Free Energy Calculation of Mechanically Unstable but Dynamically Stabilized Phases

by

Sara Kadkhodaei

B.Sc., Sharif University of Technology; Tehran, Iran, 2009

M.A., Brown University; Providence, RI, 2012

A dissertation submitted in partial fulfillment of the
requirements for the degree of Doctor of Philosophy
in The School of Engineering at Brown University

PROVIDENCE, RHODE ISLAND

May 2016

© Copyright 2016 by Sara Kadkhodaei

This dissertation by Sara Kadkhodaei is accepted in its present form
by The School of Engineering as satisfying the
dissertation requirement for the degree of Doctor of Philosophy.

Date_____ _____

A. van de Walle, Ph.D., Advisor

Recommended to the Graduate Council

Date_____ _____

A. F. Bower, Ph.D., Reader

Date_____ _____

A. Peterson, Ph.D., Reader

Approved by the Graduate Council

Date_____ _____

P. M. Weber, Dean of the Graduate School

Vitae

Sara Kadkhodaei obtained her B.Sc. in civil engineering from Sharif University of Technology, Iran, where she was ranked 2nd amongst the graduates in 2009. She was awarded, as an exceptional talent, the admission to the graduate program in structural engineering department of Sharif University of Technology. However, she decided to pursue her graduate studies in a more promising and developed environment. Therefore, she joined Brown University solids program, knowing that solids program fulfills her interests in fundamental applied science more suitably. She was awarded a one-year fellowship and was able to complete her course work in a broad range of topics, including material science and chemistry. She acquired her M.A. in chemistry in 2012 by completing necessary course work required by the department. Subsequently, she continued her study under the advice of Prof. Axel van de Walle. The outcome of her research at Brown on developing methods for free energy calculations in mechanically unstable phases is a series of conference presentations and journal papers. She received Material Research Society (MRS) graduate student award for her research during her PhD studies.

Acknowledgements

I would like to thank my advisor, Professor Axel van de Walle, for the great amount of trust, unique advice, and endless encouragement. I am indebted to Axel for many valuable opportunities he gave me during the course of this work, also for generous sharing his research experience, which provides me an important reference for my future career.

It was a privilege having such an exceptional committee of research and readers, consisting of Professor Bower and Professor Peterson. I would like to sincerely thank them all for reading and correcting the thesis, also for their constructive feedback, which added a lot to the value of the present study.

I would like to express gratitude to my lab mates, Qi-jun Hong, Joseph Yasi, Ruoshi Sun, Ljuba Miljacic, and Greg Pomrehn for all their help, many interesting discussions and their friendship.

I would like to thank my other friends, post-docs, senior researchers, and visitor scholars at Brown: Mohsen Zayernouri, Sobhan Naderi Parizi, Hamed Haftbaradaran, Akbar Bagri, Telli Davoodi, Dibakar Datta, and Ben Szajewski for their support and delightful time we spent together. I would love to express my special gratitude to my precious mother, lovely sister, and wonderful brother for their constant love, support, and friendship.

I would love to especially thank my husband, Farid Moghim, whose love, support, and encouragement made me much stronger, happier, and more faithful throughout my study at Brown.

Abstract of " Free Energy Calculation of Mechanically Unstable but Dynamically Stabilized Phases " by Sara Kadkhodaei, Ph.D., Brown University, May 2016

The phase diagram of numerous materials of technological importance features high-symmetry high-temperature phases that exhibit phonon instabilities. Leading examples include shape-memory alloys, as well as numerous refractory and structural materials. The thermodynamics of these phases have proven challenging to handle via atomistic computational thermodynamic techniques, due to the occurrence of constant anharmonicity-driven hoping between local low-symmetry distortions, while maintaing a high-symmetry time-averaged structure.

To compute the free energy in such phases, we propose to explore the system's potential energy surface by discrete sampling of local minima via a lattice gas Monte Carlo approach and by a continuous sampling via a lattice dynamics approach in the vicinity of each local minimum. Given the proximity of the local minima, it is necessary to carefully partition phase space using a Voronoi tessellation to constrain the domain of integration of the partition function, in order to avoid double-counting artifacts and enable an accurate harmonic treatment near each local minima.

We consider two different examples to illustrate our method. As a prototypical example, bcc phase of Titanium at high temperature is explored. The advantage of the introduced method over previous scheme is the capability of this method to consider alloys. Therefore as another complicated example PtTi compound system is considered.

Contents

List of Tables

List of Figures

Chapter One

Introduction

Traditionally, the fields of material science and engineering focused on precessing materials, measuring material properties and developing structure-property relations. However, designing new materials and adapting existing material to gain optimal functionality for new applications provide a promising progress in human technologies. Thanks to the rapid progress of computer power and computational methods within past decades, there is a tendency toward material design, not only based on empirical approaches, but also based on computer predictions.

Phase diagrams have been widely used as a crucial tool in material design and development which not only provide equilibrium thermodynamic data but also can be useful to assess and obtain kinetic information about the system.

1.1 Phase diagram calculation

Phase diagrams have been widely used to determine the equilibrium state of physical systems and are the traditional manifestation of the thermodynamics of a system. Understanding phase diagrams is key for development of alloys and their properties. The term "phase" is applicable to both crystalline and non-crystalline materials. In the case of crystalline materials, a phase is characterized by a specific ordering of atomic species over a given set of lattice sites, allowing for small displacement away from these ideal lattice sites. The field of alloy theory traditionally investigates the relative stability of phases in order to build the phase diagram. The relative stability of a phase is determined via the calculation of its free energy.

CALPHAD Methodology

One of the most commonly used frameworks for phase diagram calculation is computational thermodynamics based on the CALPHAD (CALculation of PHAse Diagrams) approach first introduced by L. Kaufman and H. Bernstein (1970) [34]. Within CALPHAD framework, all experimental and theoretical data available on thermodynamic properties of a system, including coexisting phases, are collected as a database. The thermodynamic properties of each phase is then described by Gibbs free energy, applying a mathematical model including adjustable parameters. These parameters are optimized using this database in a way such that the model can reproduce many experimental and first-principles data as well as theoretical models. Relative stability of phases (stability of a system in a given structure relative to other structures) is defined as the difference in molar Gibbs free energy among these phases [31, 33]. Within CALPHAD framework thermodynamic functions can be extrapolated outside the equilibrium state and provide information about thermodynamic properties outside the range of stability of a phase.

The success and popularity of the CALPHAD method is indebted to the development of multicomponent database and the capability of this method to predict the thermodynamic properties of multicomponent systems [32, 67]. The lattice stability concept (i.e. that all phases, even unstable ones, can be assigned a well-defined free energy) was essential for the development of multicomponent thermodynamic databases. Due to its hierarchal formalism, the CALPHAD model can be further extended to investigate more complicated and technologically relevant material properties as a function of temperature, pressure and composition. Although it was initially intended to account for calculation of thermodynamic properties, the CALPHAD method can be extended to model kinetic processes such as atomic diffusion and evolution of microstructure [1, 2].

First-Principle Alloy Theory

In virtue of the rapid progress of computing powers and efficiency of computational methods, now it is a possibility to explore new alloys and their properties through computer simulations without relying on experimental data. Use of first-principles calculations based on density functional theory [35] is among the most common computational methods used to build phase diagrams. Within "first-principles" phase diagram calculation, thermodynamic data are developed by single knowledge of atomic species of the system. This approach is specifically beneficial on solid-state alloys, as opposed to liquid phases, not only for computational manageability in solid phases over liquid phases, but also because of the constraints inherent to the experimental measurements of solid phases.

First-principles calculations are used to obtain quantities related to electronic structure and the total energy of a given structure. To gain thermodynamical properties of a phase, at least three different contributions to free energy have to be accounted for. The first, is the static energy or $0K$ energy; second, is due to the thermally induced lattice vibrations at finite temperatures, and third, is the thermal electronic contribution in cases where the electronic density of states (DOSs) is high at the Fermi level. In a canonical ensemble, the Helmholtz free energy as a function of temperature and volume is approximated as

$$F(V,T) = E(V) + F_{vib}(V,T) + F_{elec}(V,T) \tag{1.1}$$

where $E(V)$ is the static total energy, F_{vib} is the contribution from vibration of ions and F_{elec} is the thermal electronic contribution to the free energy.

The lattice vibration contribution, F_{vib}, is commonly handled via the standard lattice dynamics or phonon approach, using first-principles calculation within harmonic or

quasi-harmonic approximation in order to obtain full phonon spectra and density of states for a given atomic structure. These standard lattice dynamics models are applicable to mechanically stable systems where all the phonon modes have real-valued frequencies.

1.2 A Review of Current Methods

As discussed in the previous section, traditional methods for phase diagram calculation rely on the assumption that all phases, even if observed at high temperatures, are mechanically stable. This "lattice stability" assumption is the core ingredient within the traditional methods for phase diagram computation, yet it reduces the applicability of the aforementioned frameworks because the crystal structure of many high-temperature phases exhibit mechanical instabilities. For example, many transition metals [26, 55, 56, 70, 89], their alloys [12, 13, 20], accompanied by their hydrides [60, 85] and oxides [53], all reveal high-symmetry phases at elevated temperatures with mechanical instabilities. These mechanical instabilities are also common among shape memory alloys [29, 92] and refractory oxides [27, 47]. These instabilities manifest themselves via phase transitions to lower-symmetry structures at low temperature and that can be readily identified via lattice dynamics calculations based on a harmonic model centered about the high-symmetry high-temperature structure [12, 13, 20, 26, 53, 55, 56, 60, 70, 85, 89]. In some cases (such as fcc W), the mechanical instability is such that the corresponding phase simply does not exist in nature [16, 20, 52, 77]. However, in many cases, the phase is "dynamically stabilized" at high temperature, thanks to entropy contributions arising from constant hopping between local low-symmetry distortions of a high symmetry structure. The body-centered cubic phase of Titanium at low temperature is a well-known example of such

"mechanically unstable" systems [56]. The bcc structure becomes thermodynamically favorable at high enough temperatures because it constantly undergoes local distortions towards many possible similar low-symmetry structures, while maintaining time-averaged high symmetry bcc structure, which introduces large stabilizing entropic contributions to the free energy [56, 93].

The imaginary phonon frequencies obtained using harmonic phonon calculations indicate that these "mechanically unstable" phases are associated with saddle points on the potential energy hyper-surface with respect to lattice site positions, whereas mechanically stable structures are associated with minima. Therefore, standard lattice dynamic calculations, such as (quasi)-harmonic models, are inadequate for the free energy calculation of such phases, as the energy surface becomes non-convex along unstable modes and introduces nonphysical divergence in the calculation of the free energy. To calculate the free energy of such phases accurately, a practical and efficient framework has to be devised to account for anharmonic vibrational effects, which play a crucial role in stabilization of high temperature phases with low temperature mechanical instabilities.

A number of pragmatic approaches have been proposed so far [3, 23, 24, 45, 65, 66, 68, 71, 81, 94, 95], but they are not free of certain drawbacks. A brief review of these approaches is provided in the following section.

Debye model for lattice vibration

In the standard lattice dynamics model, the contribution of lattice vibrations (phonons) to the free energy under quasi-harmonic approximation is calculated according to equation (1.2):

$$F_{vib}(V,T) = k_B T \int_0^\infty \ln\left\{2\sinh\left[\frac{\hbar\omega}{2k_B T}\right]\right\} g(\omega,V)d\omega \tag{1.2}$$

where T is temperature, k_B is the Boltzmann constant, $\hbar$ is the reduced Planck's constant, ω is phonon frequency and g is the phonon density of states. In mechanically unstable phases, the above formalism can not be used to calculate vibrational contribution to free energy due to the existence of imaginary phonon frequencies. Instead, one can use the empirical Debye model to approximate the phonon density of states and obtain an estimation to the contribution of lattice vibration to the free energy (free energy of a Debye solid):

$$F_{vib}(V,T) = \frac{9}{8}k_B\Theta_D + k_BT\left\{3\ln\left[1-\exp\left(-\frac{\Theta_D}{T}\right)\right] - D\left(-\frac{\Theta_D}{T}\right)\right\} \tag{1.3}$$

where Θ_D is Debye temperature and $D\left(-\frac{\Theta_D}{T}\right)$ is the Debye function ($D(x) = \frac{3}{x^3}\int_0^x \frac{t^3}{\exp(t)-1}dt$). Mei et al. have used this model to calculate the vibrational entropy of bcc Ti [45]. This method exploits the fact that a system often remains stable with respect to macroscopic deformation even though it exhibits phonon instabilities. Since the Debye temperature can be determined from the elastic constants, this model remains directly applicable.

Ab-initio Molecular Dynamics

Ab-initio molecular dynamics (AIMD) method can be utilized to obtain free energy changes as a function of temperature using the following thermodynamic integration.

$$\frac{F(T,V)}{T} - \frac{F(T_0,V)}{T_0} = \int_{T_0}^{T} \langle U(T,V)\rangle_{NVT}\, d(1/T) \tag{1.4}$$

where the NVT-ensemble average of internal energy, U, is integrated from initial to final T. However, obtaining absolute free energy (as would be needed to predict phase transitions) remains a challenge.

AIMD calculations also suffer from the fact that they can be computationally demanding in large systems or when considering solid-solutions and compounds. This presents an obstacle especially if the time scale of the configurational changes is too long in a system.

AIMD calculations have been used in a study by Ozolins [52] to obtain the free energy and entropy difference between bcc and fcc W. Face-centered cubic W is mechanically unstable, and is only stabilized by external constraints and differs from those mechanically unstable phases that are dynamically stabilized at high enough temperatures. In their study, fixed-cell-shape AIMD is used to calculate the average stresses along the well-known Bain path, in order to be used in thermodynamic integration to obtain free energy difference [52]. The mechanical instabilities associated with the long-wavelength acoustic modes are stabilized by external constraints such as the finite size and fixed shape of the simulation cell.

Effective Hamiltonian

One can consider effective-Hamiltonians, which explicitly include the anharmonic effect within the Hamiltonian equation for lattice vibration, to calculate the free energy of entropy-driven stabilized phases [3, 71, 94, 95]. Zhong et al. and Waghmare et al. constructed a parameterized Hamiltonian with improvable approximations to energy surface in order to explain ferroelectric transitions and obtain finite temperature properties in $BaTiO_3$ and $PbTiO_3$, respectively [71, 94]. Within these studies, the energy surface is approximated by a Taylor series in terms of deviations from ideal lattice positions at least up to fourth order in order to capture the instability inherent to the ferroelectric transition. Bhattacharya et al. have used a similar approach to study mechanical instabilities associated with cubic to tetragonal deformation in TiH_2. They built an effective anharmonic strain Hamiltonian for a cubic

lattice [3].

This approach provides powerful tools to investigate phase transition phenomena but are less suited for accurate free energy calculation with one possible drawback of requiring the parametrization of the energy at $0K$, which can be a difficult task.

Self-Consistent Phonon Theory

Within self-consistent Phonon theory [7], one includes the interaction between phonons to describe phases that indicate phonon instabilities at $0K$ but become dynamically stabilized at finite temperatures. As a result, instead of a set of static phonon frequencies, a set of temperature dependent phonons are calculated. A self-consistent ab-initio lattice dynamic method was introduced by Souvatzis et al. [65], which calculates the temperature dependent phonon for bcc phase of transition metals of group IV: Ti , Zr and Hf. They used a standard supercell calculation as an initial guess for a set of self-consistent equations that takes into account the effect of temperature on the average atomic displacement from equilibrium lattice positions. Calculated phonons at finite temperature promotes the frequencies of the $0K$ unstable phonons from imaginary to real values. Knowing the self-consistent phonon spectrum, and hence the phonon density of states $g(\omega)$, the free energy can be approximated according to equation (1.2).

Self-consistent phonon theories provide computationally tractable avenues that have been successful in predicting effective phonon frequencies. However, these methods fundamentally rely on the assumption of the existence of an effective harmonic model. If this assumption is inappropriate, there is no systematic avenue to improve the accuracy of the model [23, 65, 66, 81].

1.3 The Goal of This Thesis

In this thesis, we present a statistical approach based on coarse graining of the partition function, subjected to an innovative partitioning of the phase space, which facilitates the use of the harmonic lattice vibration model for free energy calculations in mechanically unstable but dynamically stabilized phases. As shown in figure 2.1, a local exploration of multiple minima around the high symmetry structure on the potential energy surface is accomplished by partitioning the phase space into multiple corresponding regions. The partitioning scheme ensures that the harmonic approximation is not employed beyond its range of validity and eliminates unphysical divergences in the calculated harmonic free energy. We illustrate the method with the archetypical cases of bcc Ti and bcc Zr and validate the obtained free energy with National Institute of Standards and Technology (NIST) data. In the next step, we illustrate the extension of the presented method to ordered compounds and alloys considering a Titanium compound, PtTi. It is important to emphasize that the presented method is specifically beneficial when used in alloys and solid solutions where brute-force methods like AIMD are not practical.

Chapter Two

Free Energy Calculation of Mechanically Unstable but Dynamically Stabilized Phases

2.1 Phase Space Partitioning Scheme

Mechanical instabilities associated with mechanically unstable phases make it infeasible to calculate free energy of the system using the standard lattice dynamic approach. However, "dynamical stabilization" of such phases implies that the system relaxes to multiple nearby local minima. In this thesis, a general and efficient computational approach is devised in order to visit these nearby minima and to take them into account for the calculation of free energy. Consequently, the high symmetry structure is only one of the possible states (configurational states) that the system can hold, along with multiple lower symmetry configurational states that are accessible to the system due to soft nature inherent to the potential surface in harmonic mechanical unstable phases.

As schematically shown in figure 2.1, a local exploration of multiple configuration states around the high symmetry structure on the potential energy surface is accomplished by partitioning the phase space into multiple corresponding regions.

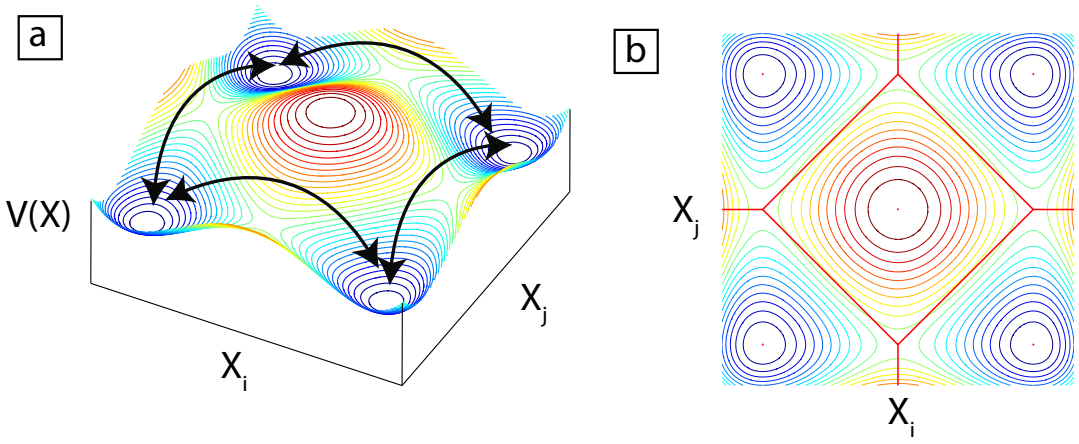

Figure 2.1: a) Schematic of potential energy including multiple local minima around the high symmetry point. b) Potential energy contour represented on the spatial phase space which is partitioned into Voronoi tesselation. Each Voronoi cell is associated with a configuration.

To account for the fact that the system hops between different local distortions of

the high symmetry lattice, we construct an *augmented lattice*, denoted by L_{aug}, that includes not only the high symmetry lattice sites, but also the sites corresponding to configurations that are local energy minima near the high symmetry structure. These additional sites can be found via the identification of unstable modes through a standard (quasi-)harmonic lattice dynamics analysis, followed by a full relaxation calculation using, as an initial configuration, high symmetry structure slightly distorted along the various unstable modes.

In the standard lattice dynamics model, wavelike solution to the classical equation of motion of atoms under a small displacement from equilibrium site is found in order to obtain phonon dispersion relations and density of states. Within harmonic model, energy of a system consisting of N atoms, which is a function of instantaneous displacement of atoms from equilibrium, can be approximated as

$$H = \sum_i \frac{\vec{\mathbf{P}}(i)}{2M_i} + \frac{1}{2}\sum_{i,j} \vec{\mathbf{u}}(i)\underline{\mathbf{\Phi}}(i,j)\vec{\mathbf{u}}(j) \tag{2.1}$$

where M_i is the mass and $\vec{\mathbf{P}}_i$ is the momentum of atom i, $\vec{\mathbf{u}}(i)$ and $\vec{\mathbf{u}}(j)$ are displacements of atoms i and j from lattice site positions. In the above approximation, the first derivative term is assumed to be zero which is only true if the system is positioned at the minimum on the energy surface. This approximation is true if the displacement of atoms from equilibrium position is small compared to interatomic distances (which is typically the case for a stable system at temperatures well below melting point).

$\underline{\mathbf{\Phi}}$ is the second derivative of energy evaluated at equilibrium position, where α and β denote Cartesian components of vectors

$$\Phi_{\alpha,\beta}(i,j) = \frac{\partial^2 E}{\partial u_\alpha(i)\partial u_\beta(j)} \tag{2.2}$$

$\underline{\mathbf{\Phi}}$ is called force constant tensor as it relates the force exerted on atom i, $\vec{\mathbf{f}}(i)$, due to displacement of atom j

$$\vec{\mathbf{f}}(i) = -\underline{\mathbf{\Phi}}(i,j)\vec{\mathbf{u}}(j) \tag{2.3}$$

In order to solve the set of equations of motion for the atoms in the system, we consider a wavelike solution of the form $\vec{\mathbf{v}}(t) = \vec{\mathbf{e}}\cos(\omega t + \phi)$ and make the change of variable $\sqrt{M_i}\vec{\mathbf{u}}(i) = \vec{\mathbf{v}}(i)$ and

$$\begin{aligned} \dot{\vec{\mathbf{P}}}(i) &= -\frac{\partial H}{\partial \vec{\mathbf{u}}(i)} = -\sum_j \underline{\mathbf{\Phi}}(i,j)\vec{\mathbf{u}}(j) \\ \sum_j \left(\frac{\underline{\mathbf{\Phi}}(i,j)}{\sqrt{M_i}\sqrt{M_j}} - \omega^2 \delta_{i,j} \right) \vec{\mathbf{e}}(j) &= 0 \end{aligned} \tag{2.4}$$

There exist a non-zero solution to equation (2.4), if the determinant of the matrix inside the parenthesis is zero. It means that the square of vibration frequencies of the system are determined by the eigenvalues of $\frac{\mathbf{\Phi}(i,j)}{\sqrt{M_i}\sqrt{M_j}}$. Associated with each eigenvalue ω_λ, there exists an eigenvector $\vec{\mathbf{e}}^\lambda$ with $3N$ components which is also called a *normal mode*.

In a mechanically stable system all the eigenvalues are positive (or the force constant matrix is positive definite), whereas in a mechanically unstable system some of the eigenvalues are negative resulting in imaginary frequencies. A negative eigenvalue indicate mechanical instability along a distortion following the corresponding eigenvector. When the unstable modes are identified through harmonic phonon analysis, one can try to find a local minimum through distortions of the system by various amplitude along the eigenvector associated with the most negative eigenvalue and relaxing the resulting structures, although it is not generally guaranteed that this approach would stabilize the unstable modes of high symmetry structure and lead to a nearby local minimum.

It is usually the case that dynamically stabilized high symmetry structures undergo

martensitic transformation at lower temperatures which manifests itself in the harmonic phonon dispersion curve as instabilities along high symmetry branches. For example, the martensitic transformation of bcc Ti and Zr to hexagonal closed packed (hcp) and ω (hexagonal) can be identified via dominant instabilities at M and along $\Gamma - R$ bcc phonon branch, respectively. One can exploit these instabilities in order to find a local minimum close to the high symmetry structure.

Once one such local minima has been identified, all other symmetrically equivalent minima can be found by applying the symmetry operations of the high-symmetry phase. If the position vector of atoms at the nearby local minimum is denoted by $\mathbf{x}_m$, and the high-symmetry position vector of atoms is denoted by $\mathbf{x}_{hs}$, the augmented lattice supercell is constructed by operating the symmetry point group of the high-symmetry structure to a lattice including both sites at $\mathbf{x}_m$ and $\mathbf{x}_{hs}$. This will result in a cell consisting of high-symmetry sites, as well as some extra sites surrounding each high-symmetry site, which form a *group* of sites.

By creating an augmented lattice, which imposes some extra lattice sites to the familiar high-symmetry lattice, phase space is partitioned into different *configurations*. A *configuration* σ, is defined as a possible assignment of atoms and vacancies to the augmented lattice sites. In order to simulate the local hopping of atoms from the high-symmetry to lower-symmetry distortions, only those configuration are considered in which there exists one atom in each *group* of sites, and all other sites in that *group* are occupied by vacancies. This results in the exclusion of states where each *group* of sites in the augmented lattice is occupied by two or more atoms (this will be explained in more details in the following sections). Figure 2.2 indicate a schematic representation of states that are excluded in our calculations.

The configurational part of free energy associated with L_{aug} is given by a $3N$-dimensional integral over the classical configurational partition function in a "coarse-

term	denotation	definition
augmented lattice	L_{aug}	Lattice consisting of high symmetry structure sites as well as extra sites associated with nearby local minima configurations
group of sites		A collection of site in the augmented lattice in which one site is occupied by an atom whereas all other sites are occupied by vacancies
configuration	σ	A possible assignment of atoms and vacancies to the augmented lattice sites
constrained vibrational free energy	F^*_σ	Free energy associated with a configuration which only includes vibrational contributions
total free energy	F_L	Free energy associated with augmented lattice including vibrational and configurational contributions
unrelaxed position	$\mathbf{x}^u_\sigma$	Atomic position vector associated with the unrelaxed position of a configuration
relaxed position	$\mathbf{x}^r_\sigma$	Atomic position vector associated with the minimum of potential energy within ζ_σ
local minimum position	$\mathbf{x}_m$	Atomic position vector associated with local minimum near the high symmetry structure
high symmetry position	$\mathbf{x}_{hs}$	Atomic position vector associated with the high symmetry structure
	ζ_σ	Portion of phase space that is defined as proximity of configuration σ
reference potential	V^{ref}	Potential energy of an artificial reference system with an isotropic positive definite Hessian
cluster	α	Symmetry-related grouping of lattice sites with different number of vertices
nearby minimum position	x_g	Atomic position vector associated with the minimum nearby the bcc structure found along bcc-to-ω transformation
short-pairs		Pair clusters which connect two sites within a group of sites
long-pairs		Pair clusters which connect two sites in neighboring groups of sites

Table 2.1: Table of terms and definitions used in the presented method.

grained" form [76]

$$F_L = -k_B T \ln \sum_{\sigma \in L_{aug}} e^{-\beta F^*_\sigma} \tag{2.5}$$

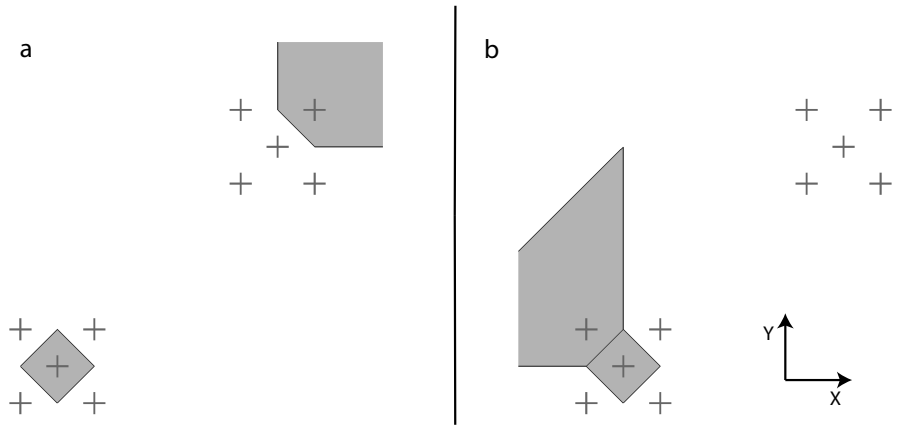

Figure 2.2: a)A 2D representation of spatial phase space, where the + signs indicate the lattice sites and the shaded areas depict the Voronoi cells associated with the sites at the center of the shaded areas. The shaded areas include all the possible coordinates for a state, so that the state is associated with a configuration in which Ti atoms occupy those sites in the center of the shaded areas. b) Representation of an example of a state that is precluded in a Monte Carlo simulations due to large imposed ECIs assigned to short-pairs.

where

$$F_\sigma^* = -k_B T \ln \int_{\mathbf{x}\in\sigma} e^{-\beta V(\mathbf{x})} d\mathbf{x} \tag{2.6}$$

where $\beta = 1/(k_B T)$, T is temperature, k_B is the Boltzmann constant, $\mathbf{x}$ is the $3N$ vector of all atomic positions, N is the number of atoms in the system and $V(\mathbf{x})$ is the potential energy of the system at a state represented by the position vector $\mathbf{x}$. The above integration can be divided into two levels. One level is the "outer" level (equation (2.5)) that sums over different configurations associated with L_{aug}, and the other is the "inner" level (equation (2.6)) which is a continuous integration of the Boltzmann distribution in the vicinity of each configuration. The inner level states are included in the set of states defined by the outer level which are characterized by *constrained vibrational free energy*, denoted by F_σ^*. The outer level states can be sampled via a cluster expansion approach [61], while a continuous sampling in the vicinity of each configuration is carried out using harmonic approximation of energy hyper-surface about each configuration (the sampling approach will be discussed in more detail in the following sections).

One has to define the proximity of each configuration for continuous sampling of the phase space. For each configuration σ, the unrelaxed atomic position of atoms is denoted by $\mathbf{x}_\sigma^u$. All the atomic position vectors closer to $\mathbf{x}_\sigma^u$ than any other configuration σ', are defined as the proximity of configuration σ and denoted by ζ_σ. This is the definition of Voronoi tessellation of the phase space [78]. The Voronoi tessellation partitioning of the phase space is preferable to the more straightforward partitioning of the phase space into hypercubes as it avoids double-counting artifacts because the regions are nonoverlapping..

For computational efficiency, we determine ζ_σ by computing the Voronoi tessellation in tridimensional space generated by the augmented lattice points (which coincides with the well-known concept of Wigner-Seitz cells [82]). We then define ζ_σ in the $3N$-dimensional phase space as the Cartesian product of the tridimensional Voronoi cell associated with each site. This construction is preferable to a Voronoi tessellation in a $3N$-dimensional space, not only for computational reasons, but also because it naturally excludes nonphysical very high energy states from the region ζ_σ, such as those where two atoms would lie in the same Wigner-Seitz cell of a given lattice site. There are some states that are excluded in our calculations as an implicit result of definition of ζ_σ. These states are much higher in energy compared with those configurations entering our calculations. If the $3N$-dimensional configurational phase space is partitioned by Voronoi tessellation, all possible configurational states are incorporated and each configurational state is associated with one specific configuration σ. Figure 2.3 illustrates partitioning of $3N$-dimensional phase space schematically. Any state in the phase space will be associated to one configuration σ. On the contrary, if the portion of phase space associated with a configuration σ is the multiplication of N 3-dimensional Voronoi cells, there exist some configurational states that are not corresponded to any of the Voronoi cells. In other words, there exist some states that do not belong to any of ζ_σ as a result of the way ζ_σ is defined. Figure 2.4 depict

a schematic state that is not counted in our calculations. As represented in figure 2.4, these states are those of very high energy and their outcome in configurational part of free energy is negligible.

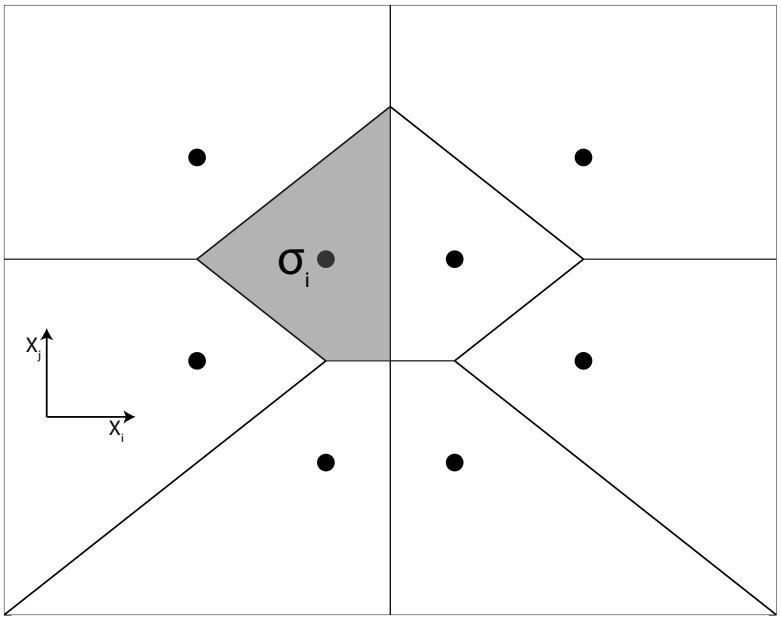

Figure 2.3: Schematic representation of partitioning of $3N$-dimensional spatial phase space into its Voronoi tessellations. The generating points (black dots) are $3N$-dimensional position vectors. The shaded area includes all the states that are associated with configuration σ_i.

2.2 Energy Surface Approximation

The partitioning scheme presented in the above section makes it possible to account for the anharmonic stabilization of the high-symmetry phase, using a harmonic approximation of the energy surface. To this end, the energy surface associated with each configuration σ is approximated as a Taylor series up to second order term. For the harmonic approximation to best represent the true potential energy, the harmonic approximation of the potential energy hyper-surface is carried out at the

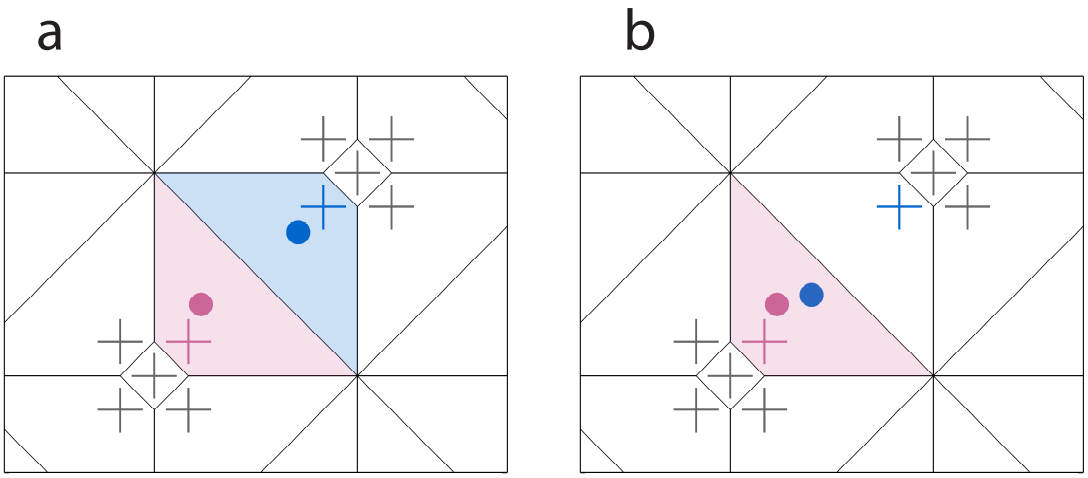

Figure 2.4: Schematic 2-dimensional representation of partitioning the spatial space into its Voronoi tessellations. The + signs indicate the lattice sites that are the generating points in the Voronoi tessellation. The circles depict the atoms. a) An example of a state which is associated with a configuration in which the atoms sit on the + signs. b) An example of a state which is associated with no configuration. The configurational state of two or more atoms lying in the shaded area simultaneously does not belong to any ζ_σ. Only those states with one atom in each Voronoi cell have a corresponding ζ_σ.

minimum of $V(\mathbf{x})$ within ζ_σ. We denote the location of this minimum by $\mathbf{x}_\sigma^r$.

To determine the minimum within ζ_σ, (which is a constrained nonlinear optimization procedure), a *steepest-descent* search is performed and an interior minimum or a boundary minimum is found. Using $\mathbf{x}_\sigma^u$ as an initial guess, a sequence of position vectors $(\mathbf{x}_\sigma^u, \mathbf{x}_1, \mathbf{x}_2, ..., \mathbf{x}_{n+1})$ is constructed by moving along the negative gradient of potential energy hyper-surface using the following equation

$$\mathbf{x}_{n+1} = \mathbf{x}_n - \gamma_n \nabla V(\mathbf{x}_n) \tag{2.7}$$

where γ_n is an arbitrary small scalar in step n. If γ_n is small enough (it satisfies Wolfe condition [84]), then $V(x_{n+1}) <= V(x_n)$ and at least one minimum is found. In the steepest-descent method, potential energy, $V(\mathbf{x}_n)$, and the gradient of potential energy, $\nabla V(\mathbf{x}_n)$, are calculated using electronic structure calculations. If the movement along the negative gradient directs the configuration outside of ζ_σ, then

the projection of the force vector, $\mathbf{f}_v(\mathbf{x}_n)$, along the boundary of ζ_σ replaces $\nabla V(\mathbf{x}_n)$ in equation (3.16).

If there exists no interior local minimum within ζ_σ, associated with a positive definite force constant matrix (defined in equation (2.2)), then the minimum must be on the boundary of ζ_σ. In this case, the force constant matrix is not necessarily positive definite, and hence there can exist some negative eigenvalues for the force constant matrix.

The first derivative of potential energy may not vanish at a boundary minimum. Whenever the gradient is nonzero, the linear term dominates for small displacements. To avoid an artificially flat energy landscape perpendicular to the gradient, we also include the quadratic contributions of the stable modes. We exclude the quadratic contributions of the unstable modes because they have little effect on the local energy landscape (their directions tend to have a large projection along the direction of the gradient). Moreover, when included, unstable quadratic terms risk introducing fictitious low-energy regions far from the boundary minimum.

In figure 2.5, an example of nonzero gradient at a boundary minimum is illustrated. The atoms that have a nonzero force magnitude are those that are located at the boundary of the corresponding Voronoi cells and the forces exerted on them are perpendicular to the Voronoi cell boundary planes. A schematic diagram manifests a typical boundary minimum configuration in figure 2.6, which demonstrates the atomic positions and forces acting on atoms corresponding to a boundary minimum.

The potential energy surface of the system is expanded up to the quadratic term around the minimum inside ζ_σ, $\mathbf{x}_\sigma^r$. The potential energy of each vibrational state, perturbed by $\Delta\mathbf{x}$ from $\mathbf{x}_\sigma^r$, is then approximated as

$$V(\mathbf{x}) = V_0 - J\Delta\mathbf{x} + \frac{1}{2}\Delta\mathbf{x}^T H \Delta\mathbf{x} \tag{2.8}$$

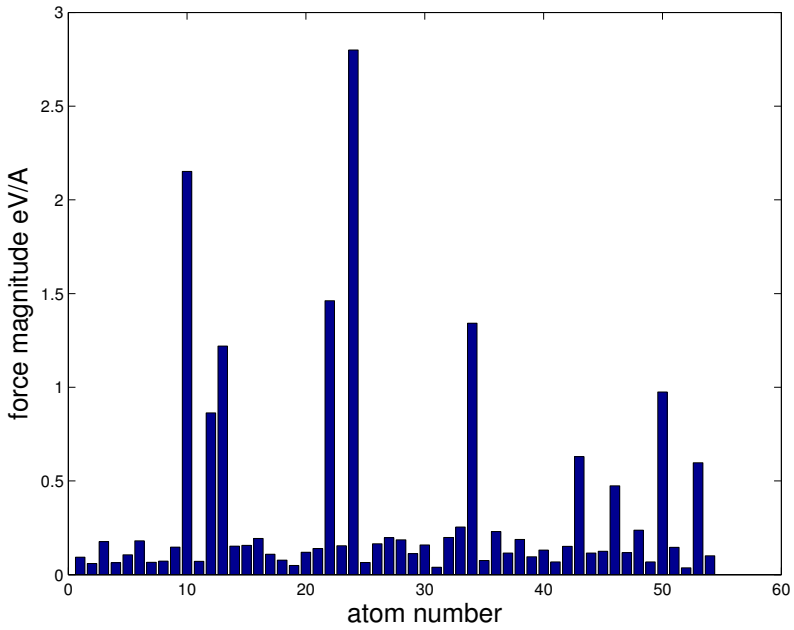

Figure 2.5: The force magnitude exerted on each atom in a configuration of 54 Ti atom supercell. Atoms with nonzero force magnitude are those that are located at the boundary of corresponding Voronoi cells at $\mathbf{x}_\sigma^r$.

where V_0 is the potential energy at $\mathbf{x}_\sigma^r$, J is the vector containing the forces in each degree of freedom (d.o.f.), H is the second derivative of potential energy with respect to displacement and $\mathbf{x}$ is the atomic position vector of a state that is displaced from $\mathbf{x}_\sigma^r$ by $\Delta\mathbf{x}$ ($\mathbf{x} = \mathbf{x}_\sigma^r + \Delta\mathbf{x}$).

$$J_i = -\frac{\partial V}{\partial x_i} \tag{2.9}$$

$$H_{ij} = \frac{\partial^2 V}{\partial x_i \partial x_j} \tag{2.10}$$

where i and j indicate the Cartesian coordinates. Both J_i and H_{ij} are calculated at $\mathbf{x}_\sigma^r$. Knowing the eigenvalues of the Hessian matrix H, the energy surface is decomposed into its principal directions (the $'$ sign indicates tensors that are transformed into principle directions)

$$H = QDQ^T \tag{2.11}$$

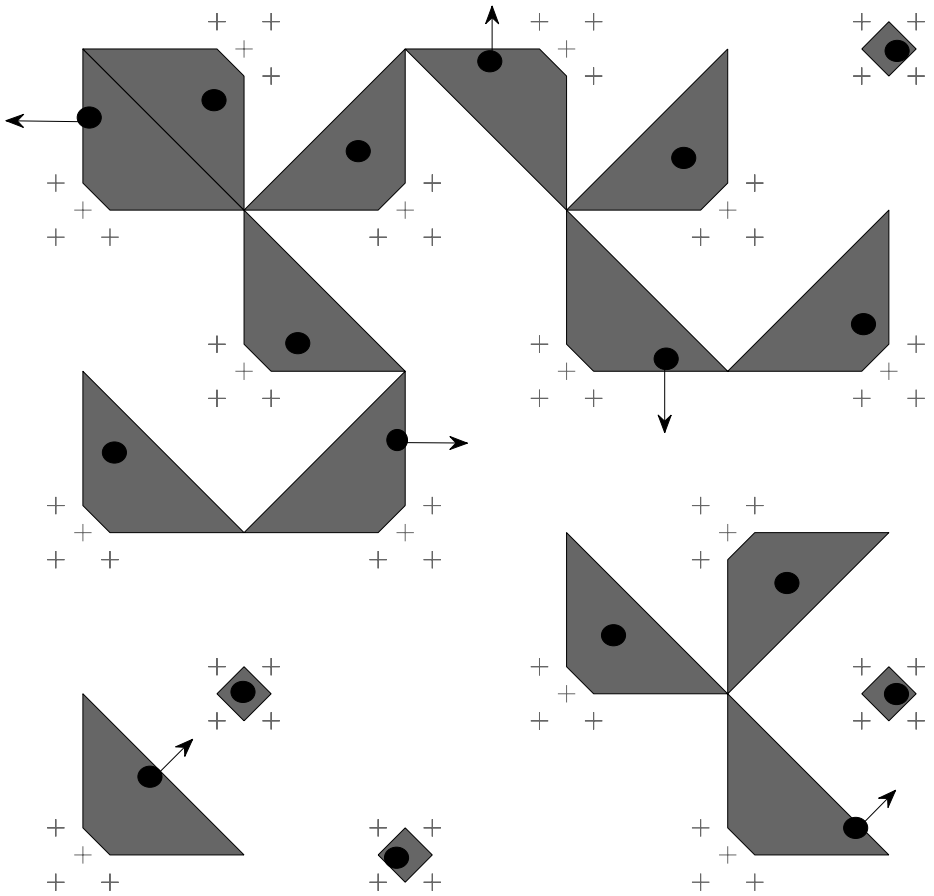

Figure 2.6: The shaded areas indicate the portion of spatial space that is sampled for a configuration σ, denoted by ζ_σ. The + signs indicate augmented lattice sites and the circles denote atoms. The minimum position is searched within ζ_σ and the forces are equilibrated unless a Voronoi cell boundary prevents the corresponding atom from moving further. In such a case, there exist a force on the atom in direction perpendicular to the Voronoi cell boundary. The arrow signs indicate the forces exerted on atoms. Those atoms with no arrows have zero first derivatives.

$$\Delta\mathbf{x}^T H \Delta\mathbf{x} = \Delta\mathbf{x}^T Q D Q^T \Delta\mathbf{x} \tag{2.12}$$

$$Q^T \Delta\mathbf{x} = \Delta\mathbf{x}' \tag{2.13}$$

$$V(\mathbf{x}) = V_0 - JQ\Delta\mathbf{x}' + \frac{1}{2}\Delta\mathbf{x}'^T D \Delta\mathbf{x}' \tag{2.14}$$

where Q is a $3N \times 3N$ matrix with its columns containing the eigenvectors of the Hessian, and D is a diagonal $3N \times 3N$ tensor containing the eigenvalues of the Hessian along each d.o.f. in eigenspace. By defining $JQ = J'$, the energy equation

is reduced to the following matrix form

$$V(\mathbf{x}) = V_0 - J'\Delta\mathbf{x}' + \frac{1}{2}\Delta\mathbf{x}'^T D\Delta\mathbf{x}' \tag{2.15}$$

where J' is a $1 \times 3N$ tensor containing the forces acting on each d.o.f in eigenspace. The scalar form of potential energy is represented accordingly

$$V(\mathbf{x}) = V_0 - \sum_{i=1}^{3N} J'_i \Delta\mathbf{x}'_i + \sum_{i=1, D_{ii}>0}^{3N} \frac{1}{2} D_{ii} \Delta(\mathbf{x}')_i^2 \tag{2.16}$$

It should be noted that the energy surface is expanded up to the first derivative along unstable modes. Therefore, if $D_{ii} < 0$, then the term $\frac{1}{2}D_{ii}\Delta\mathbf{x}_i'^2$ is not considered in the energy expression.

The rationale underlying the definition of potential energy is that if the second derivative is negative along a d.o.f., the system is not equilibrated along that d.o.f., and hence there exists a force acting along that d.o.f., and therefore, the first derivative is dominant in the expression for energy fluctuations (2.16) (except for cases where $\mathbf{x}_\sigma^r$ is located on a maximum along that d.o.f., which can be neglected because the number of such d.o.f.s does not increase when system size increases, i.e. in the thermodynamic limit $N \to \infty$).

In order to include kinetic effects, the classical partition function of a canonical ensemble for a system of N atoms associated with a configuration σ is then formulated as the following

$$Q = \frac{1}{h^{3N}} \int_{-\infty}^{\infty} \int_{\mathbf{x}\in\zeta_\sigma} e^{-\beta\frac{\mathbf{p}^2}{2m}} e^{-\beta V(\mathbf{x})} d\mathbf{x} d\mathbf{p} \tag{2.17}$$

where

$$Z_\sigma = \int_{\mathbf{x}\in\zeta_\sigma} e^{-\beta V(\mathbf{x})} d\mathbf{x} \tag{2.18}$$

is the *configuration partition function* which only includes spatial degrees of freedom. We define the partition function in equation (2.17) as the *constrained partition function*, since it only integrates over those states that are confined in ζ_σ and are associated with configuration σ. The partition function does not have the usual $N!$ term in the denominator because the system is confined inside ζ_σ and no two atoms are allowed to permute. By factoring out the kinetic part of the partition function, equation (2.17) is reduced to

$$Q = Z_\sigma \times \prod_{i=1}^{3N} \frac{1}{h}[\int_{-\infty}^{\infty} e^{-\beta \frac{p_i^2}{2m_i}} dp_i] \tag{2.19}$$

As indicated in equation (2.18), the $3N$-dimensional integral is over a complex hypervolume ζ_σ. Therefore, the analytic integration of the configurational partition function is not feasible, although the integral has known analytical solutions over certain simpler domains. Considering the mathematical complexity of the integration domain, the partition function associated with configuration σ, Z_σ, can be reformulated to the following form by the definition of function 1(A):

$$Z_\sigma = \int_{\mathbf{x}\in\zeta_\sigma} e^{-\beta V(\mathbf{x})} d\mathbf{x} = \int_{\mathbf{x}\in R} 1(\mathbf{x} \in \zeta_\sigma) e^{-\beta V(\mathbf{x})} d\mathbf{x} \tag{2.20}$$

where R is a hypercube containing ζ_σ. 1(A) is 1 if condition A is true and 0 otherwise. By multiplying and dividing (2.20) by $\int_{\mathbf{x}\in R} e^{-\beta V(\mathbf{x})} d\mathbf{x}$, which has an analytical solution, the following form is obtained

$$Z_\sigma = \frac{\int_{\mathbf{x}\in R} 1(\mathbf{x} \in \zeta_\sigma) e^{-\beta V(\mathbf{x})} d\mathbf{x}}{\int_{\mathbf{x}\in R} e^{-\beta V(\mathbf{x})} d\mathbf{x}} \times \int_{\mathbf{x}\in R} e^{-\beta V(\mathbf{x})} d\mathbf{x} \tag{2.21}$$

The first term is the ensemble average of the ratio of the number of states inside ζ_σ to the number of states inside R, and is carried out using Monte Carlo simulation,

where the Metropolis algorithm is used to draw the states. The second term is carried out analytically.

For a configuration σ, the potential energy hyper-surface is expanded harmonically about the minimum within ζ_σ. The minimum position vector, $\mathbf{x}_\sigma^r$, includes some atomic positions located at the boundary of their Voronoi cell (see figure 2.6). In such case, the ratio of the number of states inside ζ_σ to the number of states inside R, denoted by r, is very close to zero. The decay of ratio r to zero is accelerated as the dimension of the variable space for the integral in equation (2.21) increases. Therefore, even for a system of small number of atoms, the dimension of space, $3N$, is high enough to make the value of r almost zero. Free energy is a logarithmic function of this ratio, $F = f(\ln(r))$, and if the statistical error corresponding to the calculation of r is s_r, then the statistical error associated with the free energy is proportional to s_r/r. If r is close to zero, then the statistical error associated with the free energy is large and free energy does not converge to reasonable values within a practical computation effort. Moreover, divergence issues in the calculation of free energy due to existence of unstable modes present computational obstacles. Hence, the calculation of the first term in equation 2.21 is not feasible.

To circumvent these computational obstacles, the well-known adiabatic switching technique is used. The idea is to select a reference potential $V^{ref}(\mathbf{x})$ with a positive definite Hessian that is sufficiently stiff so that the integral in (2.20) yields same value whether or not it is constrained over the domain ζ_σ. For such stiff reference potential, the integration domain in equation (2.20) could be extended to infinity and the configurational partition function can be calculated analytically. Therefore, for the reference potential energy, the partition function is obtained analytically.

The reference potential is defined as a harmonic potential well, with its minimum

located at the unrelaxed configuration, $\mathbf{x}_\sigma^u$.

$$V^{ref}(\mathbf{x}) = V_0 + \frac{1}{2}(\Delta\mathbf{x}' + \mathbf{s})^T C(\Delta\mathbf{x}' + \mathbf{s}) \tag{2.22}$$

where $\mathbf{s}$ is the difference between the minimum position vector and the unrelaxed position, $\mathbf{x}_\sigma'^r - \mathbf{x}_\sigma'^u$, and C is a positive definite diagonal tensor, with its diagonal elements as the second derivatives of the reference potential energy. For simplicity, the second derivative of the reference potential is assumed to be isotropic with all its elements equal to 20 $eV/\mathring{A}^2$.

Locating the reference potential minimum at the center of Voronoi cell of each configuration is not only advantageous computationally for the calculation of equation (2.21), but also necessary for the feasibility of free energy calculation. If the reference energy is expanded about the minimum of the real energy inside ζ_σ, $\mathbf{x}_\sigma^r$, and if $\mathbf{x}_\sigma^r$ is a boundary minimum -which it usually is-, irrespective of how stiff the reference potential is, the ratio r in equation (2.21) approaches zero and makes the partition function value unphysical.

When the free energy of the reference system is calculated based on equation (2.21), the free energy difference between the real system and the reference systems is obtained by defining a thermodynamic path between two states: a state where the system is characterized by the real potential energy, and a state where the system is characterized by the reference potential energy.

The constrained vibrational free energy difference between the reference and real systems is treated as the problem of transforming the system from one thermodynamic state to another. The reference and real states are denoted by $\mathcal{A}_0$ and $\mathcal{A}_1$, respectively. At the microscopic level, these states are characterized by potential energy surfaces $V_{\mathcal{A}_0}(x_1, x_2, ..., x_{3N})$ and $V_{\mathcal{A}_1}(x_1, x_2, ..., x_{3N})$. The system is switched slowly or adiabatically from state $\mathcal{A}_0$ to state $\mathcal{A}_1$, allowing the system to fully relax

at each point along the path. The unphysical path transforming $\mathcal{A}_0$ to $\mathcal{A}_1$ is to be of no concern because free energy is a state function and is independent of the path connecting the states.

A new potential energy is defined by employing an external switching parameter, λ,

$$\hat{V}(\mathbf{x},\lambda) = \hat{V}(\mathbf{x},0) + \lambda(\hat{V}(\mathbf{x},1) - \hat{V}(\mathbf{x},0)) \tag{2.23}$$

where $\hat{V}(\mathbf{x},0) = V_{\mathcal{A}_0}(\mathbf{x})$ (reference potential energy) and $\hat{V}(\mathbf{x},1) = V_{\mathcal{A}_1}(\mathbf{x})$ (real potential energy). When $\lambda = 0$, the switching potential is equal to the reference potential, and when $\lambda = 1$, it is equal to the real system potential. The free energy difference between the two states $\mathcal{A}_0$ and $\mathcal{A}_1$ is given by integrating the derivative of free energy with respect to λ along the switching path.

$$\Delta F^* = F^*_{\mathcal{A}_1} - F^*_{\mathcal{A}_0} = \int_0^1 \frac{\partial F^*(\lambda)}{\partial \lambda} d\lambda \tag{2.24}$$

where $F^*(\lambda)$ is the constrained vibrational free energy of a configuration σ characterized by the potential $\hat{V}(\mathbf{x},\lambda)$, given by

$$F^*(\lambda) = -k_B T \ln(\int_{\mathbf{x}\in\zeta_\sigma} e^{\frac{-\hat{V}(\mathbf{x},\lambda)}{k_B T}} d\mathbf{x}) \tag{2.25}$$

The kinetic part of partition function is not included in the free energy calculation because it is the same for both states $\mathcal{A}_0$ and $\mathcal{A}_1$ and cancels out in (2.24).

$$\frac{\partial F^*(\lambda)}{\partial \lambda} = -k_B T \frac{\int_{\mathbf{x}\in\zeta_\sigma} e^{\frac{-\hat{V}(\mathbf{x},\lambda)}{k_B T}} \frac{-1}{k_B T} \frac{\partial \hat{V}(\mathbf{x},\lambda)}{\partial \lambda} d\mathbf{x}}{\int_{\mathbf{x}\in\zeta_\sigma} e^{\frac{-\hat{V}(\mathbf{x},\lambda)}{k_B T}} d\mathbf{x}} = \frac{\int_{\mathbf{x}\in\zeta_\sigma} e^{\frac{-\hat{V}(\mathbf{x},\lambda)}{k_B T}} \frac{\partial \hat{V}(\mathbf{x},\lambda)}{\partial \lambda} d\mathbf{x}}{\int_{\mathbf{x}\in\zeta_\sigma} e^{\frac{-\hat{V}(\mathbf{x},\lambda)}{k_B T}} d\mathbf{x}} = \left\langle \frac{\partial \hat{V}(\mathbf{x},\lambda)}{\partial \lambda} \right\rangle_{\lambda,\mathbf{x}\in\zeta_\sigma} \tag{2.26}$$

where $\langle ... \rangle_\lambda$ denotes an average over a canonical ensemble described by the distribution $e^{\frac{-\hat{V}(\mathbf{x},\lambda)}{k_B T}}$ with a fixed value for λ.

For the simple choice of a linear interpolation for switching potential in (2.23), equa-

tion (2.26) becomes

$$\frac{\partial F^*(\lambda)}{\partial \lambda} = \left\langle \hat{V}(\mathbf{x},1) - \hat{V}(\mathbf{x},0) \right\rangle_{\lambda,\mathbf{x}\in\zeta_\sigma} \tag{2.27}$$

Therefore, the constrained vibrational free energy difference between the real and the reference potential for a configuration σ is given by

$$F^*_{\mathcal{A}_1} - F^*_{\mathcal{A}_0} = \int_0^1 \left\langle \hat{V}(\mathbf{x},1) - \hat{V}(\mathbf{x},0) \right\rangle_{\lambda,\mathbf{x}\in\zeta_\sigma} d\lambda \tag{2.28}$$

To obtain the integral in (2.28), a set of values for λ is chosen from the interval [0 1], and at each value of λ_k, Monte Carlo calculation is carried out in order to obtain $\left\langle \hat{V}(\mathbf{x},1) - \hat{V}(\mathbf{x},0) \right\rangle_{\lambda_k,\mathbf{x}\in\zeta_\sigma}$. If λ values are close to zero, then the switching potential imitates the reference potential, and a small portion of phase space is explored because the switching potential is a stiff harmonic potential well. On the other hand, for λ values close to 1, $\hat{V}(\mathbf{x},\lambda)$ reproduces the real potential surface and therefore a larger portion of configurational phase space is sampled due to existing instabilities and soft modes. Consequently, the value of $\left\langle \hat{V}(\mathbf{x},1) - \hat{V}(\mathbf{x},0) \right\rangle_{\lambda,\mathbf{x}\in\zeta_\sigma}$ is expected to vary moderately when λ is close to 0 and more promptly for λ values close to 1. Therefore, implementing the Gaussian quadrature with a higher density of nodes close to 1 is more practical. We used 5-point Gauss-Legendre quadrature with the weights and abscissas converted to [0 1] interval for calculation of the integral in (2.28).

The constrained vibrational free energy for the reference potential energy is calculated analytically considering the definition of reference potential energy in equation (2.22). As shown in figure 2.7, for each λ value, a Monte Carlo sampling is conducted using the Metropolis algorithm to draw the states over the green energy surface (which represents $\hat{V}(\mathbf{x},\lambda)$), in oder to calculate the difference between the real potential energy surface (represented by the red curve) and the reference poten-

tial surface (represented by the blue curve). This energy difference value is indicated by the shaded area. In figure 2.8, an example of the calculation of the integral in

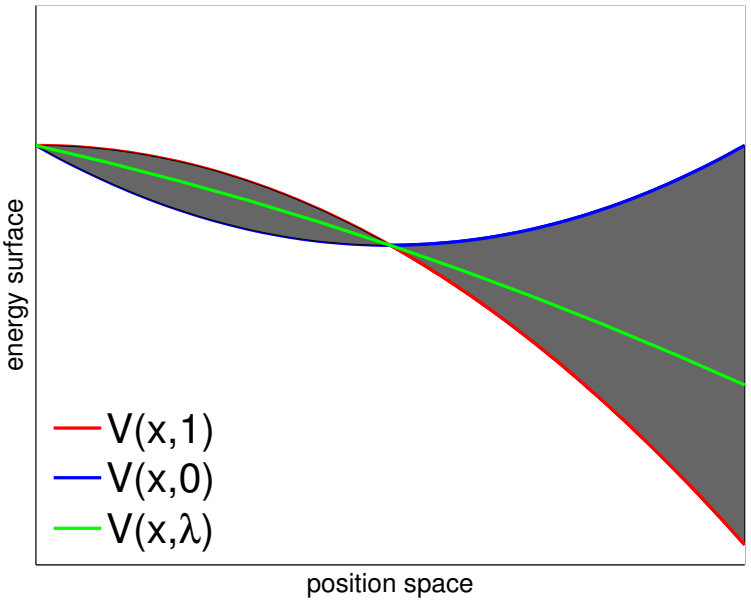

Figure 2.7: The red, green, and blue curves are schematic representations of real, switching, and reference energy surfaces, respectively. For each λ value, a Monte Carlo sampling is conducted using the switching potential to draw the states, in order to calculate the energy difference between the real and reference energy surfaces, indicated by the shaded area.

(2.28) for a supercell of Ti, including 54 atoms, is illustrated.

2.3 Cluster Expansion of Vibrational Free Energy

The procedure for calculating the vibrational free energy, for a number of different configurations σ, becomes computationally time-demanding very quickly as the number of sampled configurations increases. Since the energy surface and its derivatives are calculated using density functional theory (DFT), based on first-principles approach, it is not feasible to calculate the vibrational free energy associated with each configuration σ by direct Monte Carlo sampling of DFT energy functions. There-

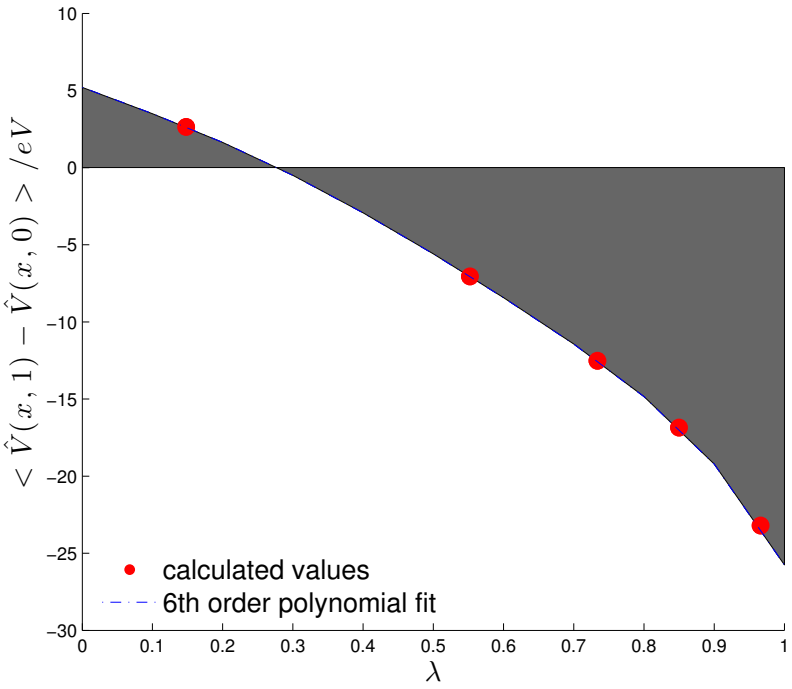

Figure 2.8: The red dots indicate the calculated energy difference values at different λ values. 5-point Gauss-Legendre quadrature is used for calculating the integral in equation (2.28), represented by the shaded area.

fore, it is preferable to obtain a compact and efficient formulation for vibrational free energy as a function of configuration and temperature.

To this end, the widely-used cluster expansion technique is used, which presents an accurate and practical way to model the configuration dependence of vibrational free energy . Within this approach, a microstate of atomic configuration is mapped into an Ising-like lattice model with each atomic species represented by a spin S_i. The constrained vibrational free energy of any configuration σ ($\sigma = \langle S_1, S_2, ..., S_{N_s} \rangle$) can be calculated using the following Ising-like Hamiltonian

$$\begin{aligned} \frac{F^*(T,\sigma)}{N_s} &= J_0(T) + \sum_i J_i(T) S_i + \sum_{i \neq j} J_{ij}(T) S_i S_j + \sum_{i \neq j \neq k} J_{ijk}(T) S_i S_j S_k + ... \\ &= \sum_\alpha m_\alpha J_\alpha(T) \left\langle \prod_i S_i \right\rangle_{\alpha'} \end{aligned} \tag{2.29}$$

In the above equation, cluster, denote by α, is symmetry-related grouping of lattice sites with different number of vertices. For example, cluster α can consist of a single site, a nearest neighbor pair, or a three-body cluster, and etc. The average $\langle \prod_i S_i \rangle$ is called the correlation function and is defined as the product of the spin variable over all sites of a cluster. The sum in the above equation is over symmetrically distinct clusters α, while the average is over clusters α' that are symmetrically equivalent to α. N_s is the number of sites in the parent lattice; m_α is the multiplicity or degeneracy factor of cluster α (the number of clusters that are equivalent by symmetry to α divided by the number of lattice sites), and $J_\alpha(T)$ is the effective cluster interaction (ECI) of cluster α at temperature T (to be determined via a fitting procedure). The effective cluster interactions encompass the energetic information of the system. The first term in the sum is a constant associated with an empty cluster, while the proceeding terms are associated with point, pair, triplet, and higher order clusters. The effective cluster interactions are temperature-dependent, unlike the well-known cluster expansion of energy with temperature-independent ECIs [76]. This temperature-dependent interaction is the result of entropic contribution included within the cluster expansion or simply the temperature dependency of free energy.

Theoretically, when including all clusters α within the sum, cluster expansion can represent any function $F^*(T, \sigma)$ of configuration σ by a relevant selection of ECIs. However, it is not practical to include all clusters. Therefore, the expansion is truncated to a finite number of terms. Different sets of α clusters can be considered to represent the cluster expansion. The advantage of cluster expansion is that (free) energy converges rapidly with respect to the number of vertices included in the cluster. Thermodynamic properties can be obtained with sufficient accuracy by using relatively compact clusters, like short range pairs and triplets.

The ECIs of a cluster expansion are usually determined by a fit to energy of a number of configurations from first-principle calculations. The set of configurations of

which energies are used to fit the cluster expansion is called the training data set, and the ECIs are the parameters that are trained. In this case, data points are the constrained vibrational free energy for a number of configurations, computed using the presented scheme.

If too few terms (clusters) are included in the expansion, it is not an accurate representation of free energy, while if too many terms are included, the problem of overfitting manifests itself. Therefore, a choice of clusters that compromises between the two competing undesirable effects has to be considered. Therefore, determination of the performance of the fit differs from the standard fitting procedure, which is assessed by a mean squared error, and a more sophisticated evaluation factor is needed (discussed in the following sections).

In our scheme, we include clusters up to the pairs between nearest neighbor *group* of sites in the cluster expansion. Therefore, the expansion includes an empty cluster, point clusters and pair clusters. This choice of clusters is adequate in capturing free energy fluctuations with respect to configuration variations and defines the configurational dependency of vibrational free energy. Two different categories of pairs can be identified in this case. One is the pair that connects two sites inside each *group* of sites (short-pairs), and the other is the pair that connects two sites in nearest neighbor *group* of sites (long-pairs). A *group* of sites is defined as a collection of sites in the augmented lattice surrounding each high-symmetry site. Not more than one atom can occupy each *group* of sites in order to replicate the hopping of atoms around the high symmetry site. Therefore, each *group* of sites can be occupied by one atomic species, and the remaining sites inside the *group* are occupied by vacancies. An example of short-pairs and long-pairs is illustrated in figure 2.9.

All of the ECIs associated with these clusters, with the exception of those associated with short-pairs, are fitted using the training data set. These short-pairs have to be treated differently in our scheme because they are undesirable pairs that have to be

precluded during Monte Carlo simulations. The reason is that we want to exclude configurations with atoms that are unphysically close to each other. We want to do so without calculating the DFT energies of unphysical configurations. Within the training data set, there exists no configuration with two or more atoms in one *group* of sites. As a result, after the fitting procedure, the ECIs associated with short-pairs are zero. However, these ECIs should be set to very large values in the Hamiltonian in equation (2.29) to present a penalty in the energy equation in order to prevent two or more atoms to occupy one *group* of sites (see figure 2.2). Moreover, these large ECIs are imposed in such a way that there is no energy cost if one atom occupies each *group* of sites.

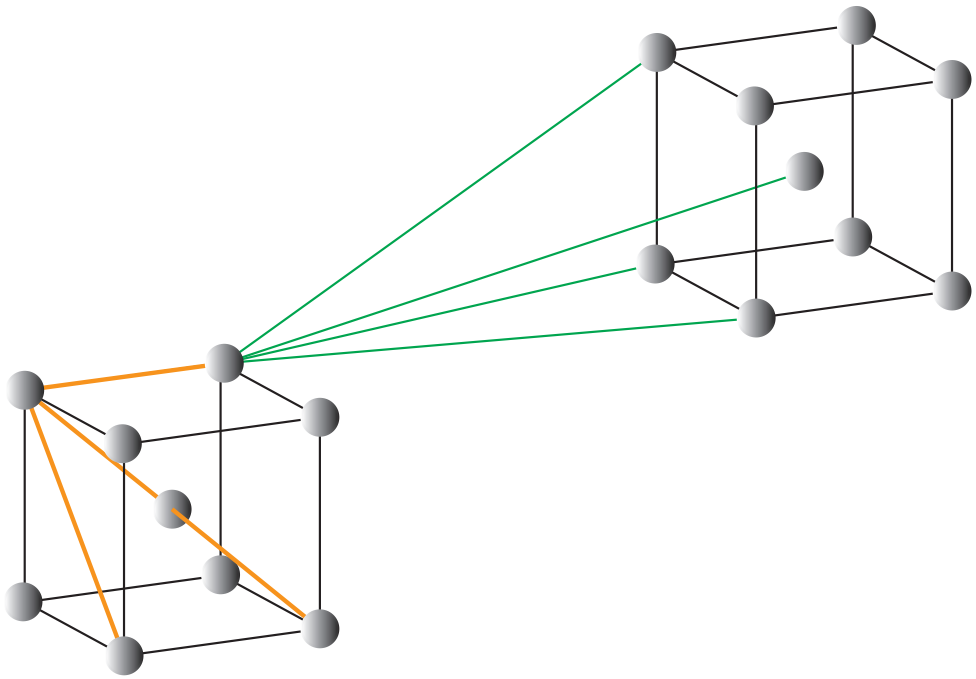

Figure 2.9: The yellow lines indicate short-pairs and the green lines represent some of the nearest neighboring long-pairs as an example. By imposing large ECIs for short-pairs, they are avoided during a Monte Carlo simulation, and hence the constraint of each *group* being occupied by one atom is satisfied.

The expansion in equation (2.29) is improved by adding more data points to the relatively small initial training data set in order to obtain converged values for ECIs. Two criteria are generally considered when adding new data points. First, if the

fit predicts a new minimum (free) energy structure, that minimum is added to the training data set. Second, including data points which span over an increasing number of dimensions in the occupation (spin) vector space is necessary.

The performance of the fit is evaluated by the cross-validation (CV) score, which is an indicator of the predictive power of cluster expansion, and defined as

$$CV = n^{-1} \sum_{i=1}^{n} \left(F_i^* - \hat{F}_{(i)}^* \right)^2 \tag{2.30}$$

where F_i^* is the calculated vibrational free energy of structure i, and $\hat{F}_{(i)}^*$ is the predicted value of vibrational free energy of structure i obtained by a least-squares fit to the remaining $(n-1)$ structures in the data set. This is the definition of leave-one-out cross-validation type score and has been used in this study employing the Alloy-Theoretic Automated Toolkit (ATAT) [72, 74, 75]. As shown in figure 2.10(a), the calculated F_i^* and the predicted $\hat{F}_{(i)}^*$ for a number of configurations are compared. The prediction error associated with each configuration i, $\left(F_i^* - \hat{F}_{(i)}^* \right)^2$, is illustrated in 2.10(b). The performance of the fit is improved by increasing the number of data points in the training data set. New data points are added to a fit until the set of ECIs provides a converged value for vibrational free energy and the performance of the fit is satisfactory.

If data points (vibrational free energies) in the training data set are associated with temperature T_1, the fit obtained for vibrational free energy is only valid at temperature T_1. In order to obtain data points at other temperatures, rather than using the relatively expensive presented scheme, constrained vibrational free energy at any other temperature T_2 is calculated knowing F^* at T_1, using the well-known thermodynamic integration reformulated as the following

$$\frac{F^*(T_2, \sigma)}{T_2} = \frac{F^*(T_1, \sigma)}{T_1} + \int_{T_1}^{T_2} \langle U_\sigma(T) \rangle \, d(1/T) \tag{2.31}$$

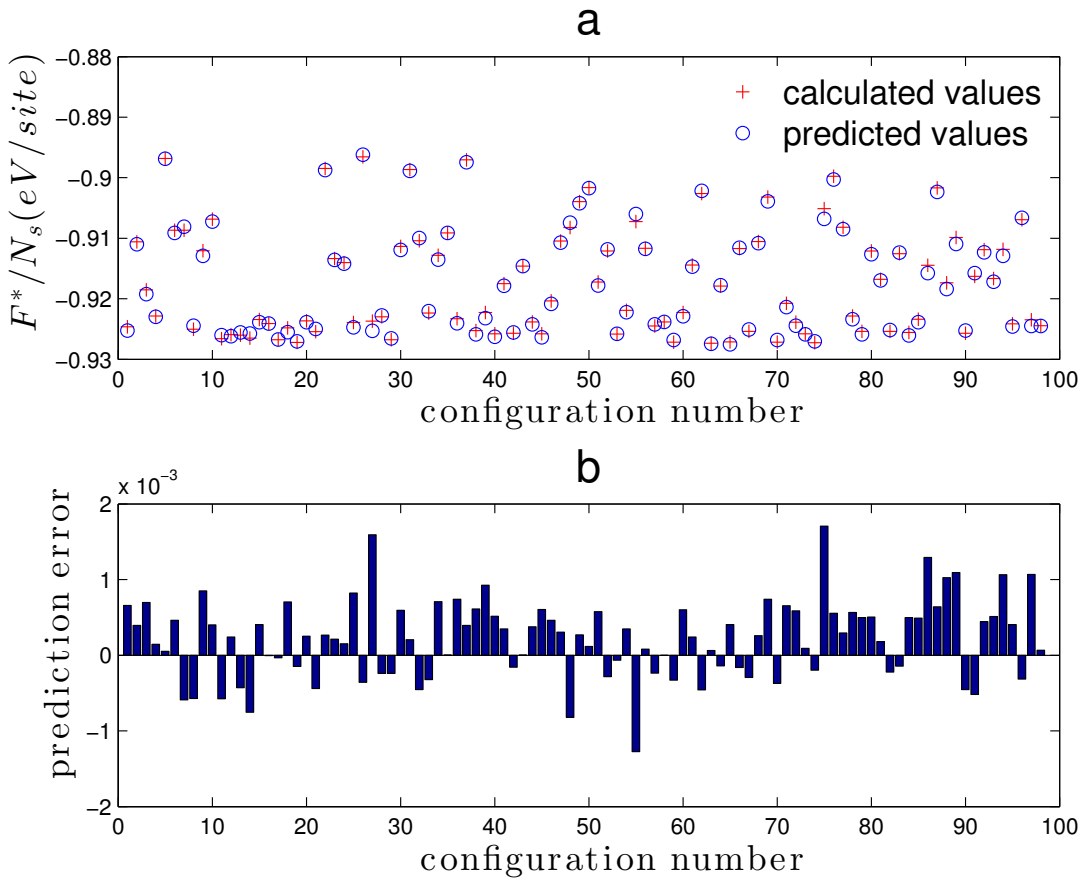

Figure 2.10: a)The red + indicates the calculated vibrational free energy for a number of different configurations using the presented method, while the blue o indicates the predicated values for vibrational free energy using cluster expansion fit. b)The predication error associated with each configuration is indicated. The CV score associated with this expansion is 0.002.

where $\langle U_\sigma(T)\rangle$ is the average internal energy of the system constrained to the Voronoi cell associated with configuration σ at temperature T.

The above equation is a reformulation of the well-known thermodynamic integration with the following derivation.

Defining the constrained vibrational free energy, $F^*_\sigma = -k_B T \ln \int_{\mathbf{x}\in\sigma} e^{-\beta V(\mathbf{x})} d\mathbf{x}$ the following derivative is calculated:

$$\begin{aligned}\left[\frac{\partial(F^*_\sigma/T)}{\partial(1/T)}\right]_{V,N} &= 1/T\left[\frac{\partial F^*_\sigma}{\partial T}\frac{\partial T}{\partial(1/T)}\right] + F^*_\sigma \\ &= -T\left[\frac{\partial F^*_\sigma}{\partial T}\right] + F^*_\sigma\end{aligned} \tag{2.32}$$

where

$$\begin{aligned}\left[\frac{\partial F_\sigma^*}{\partial T}\right] =& \frac{\partial}{\partial T}\left[-k_B T \ln \int_{\mathbf{x}\in\sigma} e^{-\beta V(\mathbf{x})} d\mathbf{x}\right] \\ =& -k_B \ln \int_{\mathbf{x}\in\sigma} e^{-\beta V(\mathbf{x})} d\mathbf{x} - k_B T\left(\frac{\int_{\mathbf{x}\in\sigma} 1/(k_B T^2) V(\mathbf{x}) e^{-\beta V(\mathbf{x})} d\mathbf{x}}{\int_{\mathbf{x}\in\sigma} e^{-\beta V(\mathbf{x})} d\mathbf{x}}\right) \\ =& -k_B \ln(Z_\sigma) - \frac{U_\sigma}{T} = -S_\sigma\end{aligned} \tag{2.33}$$

where Z_σ is the constrained partition function defined in (2.18), U_σ is the average potential energy constrained to configuration σ and S_σ is the entropy associated with configuration σ. In fact, S_σ is the vibrational entropy since it only contains the vibrational states within ζ_σ. The kinetic part of the partition function, which only depends on the momenta, is factored out according to equation (2.19), as the constraint ζ_σ has no effect on the integration boundary for the momentum variables. Therefore, equation (2.32) reduces to

$$\left[\frac{\partial(F_\sigma^*/T)}{\partial(1/T)}\right]_{V,N} = TS_\sigma + F_\sigma^* = U_\sigma \tag{2.34}$$

In figure 2.11, an example of integration in equation (2.31) is illustrated. As shown in figure 2.11(a), the average internal energy (including kinetic energy and potential energy) per atom for a prototypical example configuration including 54 Ti atoms is calculated using Monte Carlo integration. Metropolis algorithm is used to draw the states in order to sample the potential energy of the real system constrained inside ζ_σ. In figure 2.11(b), the internal energy is integrated with respect to inverse temperature according to equation (2.31) using trapezoidal rule.

Once a satisfactory fit for the vibrational free energy, $F_{\sigma,T}^*$, is obtained, the outer level sum in equation (2.5) needs to be calculated in order to obtain the total free energy associated with augmented lattice L_{aug} at temperature T. Monte Carlo simulation is carried out to calculate the ensemble average of constrained vibrational

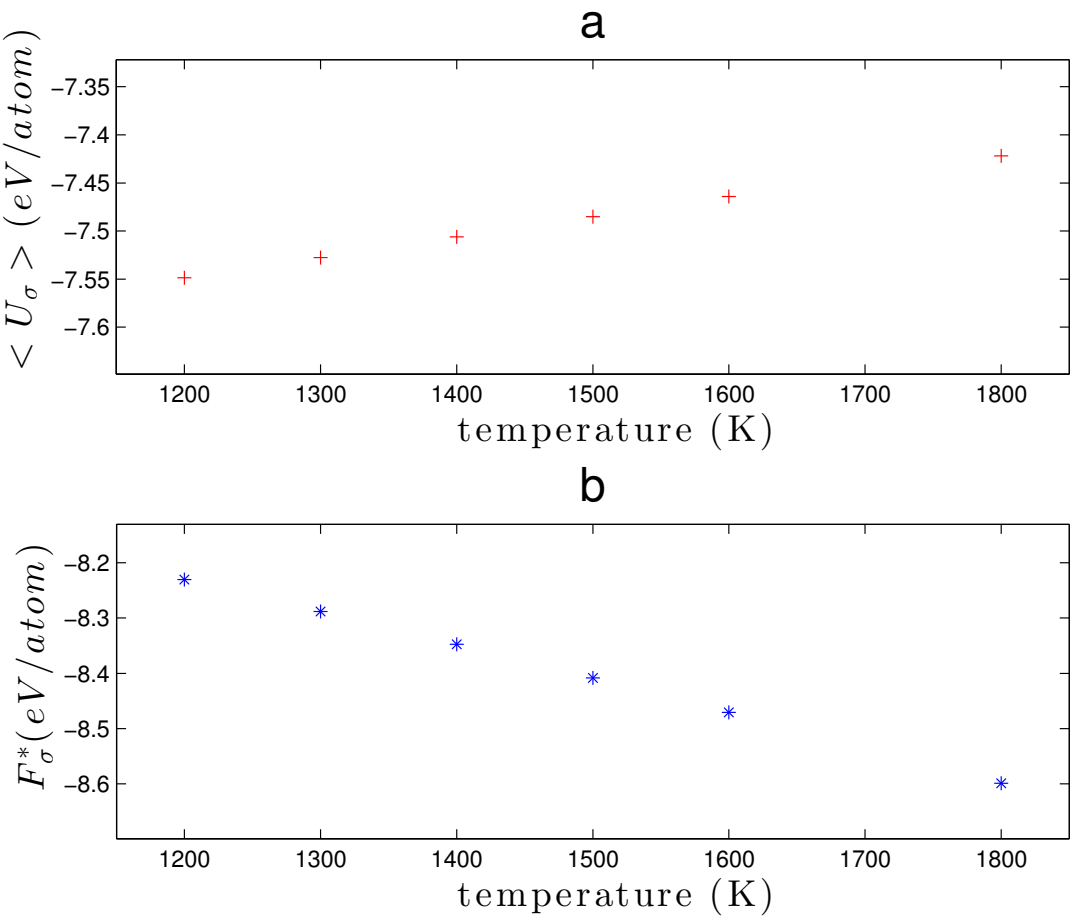

Figure 2.11: a)Average internal energy per atom for a prototypical configuration including 54 Ti atoms. b)Vibrational free energy obtained at different temperatures by integrating internal energy with respect to inverse temperature according to equation (2.31) using trapezoidal rule.

free energy, $\langle F^*_\sigma \rangle$, with equation (2.29) once the set of $\{J(T)\}$ is known, utilizing MultiComponent Easy Monte Carlo Code (memc2) [72].

2.4 Thermodynamic Integration

To calculate the Helmholtz free energy associated with lattice L at any temperature T_1, we employ thermodynamic integration in accordance with the following equation

$$\frac{F(T_1)}{T_1} - \frac{F(T_0)}{T_0} = \int_{T_0}^{T_1} \langle F^*(T) \rangle \, d(1/T) \tag{2.35}$$

where $\langle F^*(T) \rangle$ is the average vibrational free energy at temperature T and $F(T)$ is the total free energy at T. The above equation is the relation between the total free energy (including vibration and configuration contribution) associated with lattice L and the average vibrational free energy, and is a coarse-grained form of the well-known thermodynamic relation of equation (2.31) with the following derivation. Total free energy is defined in the subsequent coarse-grained equation

$$\begin{aligned} F =& - k_B T \ln \sum_{\sigma} \int_{\mathbf{x} \in \sigma} e^{-\beta V(\mathbf{x})} d\mathbf{x} \\ =& - k_B T \ln \sum_{\sigma} \exp(-\beta \left[-k_B T \ln \int_{\mathbf{x} \in \sigma} e^{-\beta V(\mathbf{x})} d\mathbf{x} \right]) \\ =& - k_B T \ln \sum_{\sigma} \exp(-\beta F_{\sigma}^*) \end{aligned} \tag{2.36}$$

Then the thermodynamic integration is derived accordingly

$$\begin{aligned} \left[\frac{\partial (F/T)}{\partial (1/T)} \right]_{V,N} =& 1/T \left[\frac{\partial F}{\partial T} \frac{\partial T}{\partial (1/T)} \right] + F \\ =& -T \left[\frac{\partial F}{\partial T} \right] + F \end{aligned} \tag{2.37}$$

where

$$\begin{aligned}\left[\frac{\partial F}{\partial T}\right] =& \frac{\partial}{\partial T}\left[-k_B T \ln \sum_{\sigma} e^{-\beta F^*_{\sigma}}\right] \\ =& -k_B \ln \sum_{\sigma} e^{-\beta F^*_{\sigma}} - k_B T \left(\frac{\sum_{\sigma} 1/(k_B T^2) F^*_{\sigma} e^{-\beta F^*_{\sigma}}}{\sum_{\sigma} e^{-\beta F^*_{\sigma}}}\right) \\ =& -k_B \ln(Z_t) - \frac{\langle F^* \rangle}{T}\end{aligned} \tag{2.38}$$

where Z_t denotes the total partition function which takes into account both vibrational and configurational states. Using the definition of free energy $F = -k_B T \ln(Z_t)$, the following relation is obtained.

$$\begin{aligned}&\left[\frac{\partial(F/T)}{\partial(1/T)}\right]_{V,N} = k_B T \ln(Z_t) + \langle F^* \rangle + F = -F + \langle F^* \rangle + F = \langle F^* \rangle \\ &\frac{F(T_1)}{T_1} - \frac{F(T_0)}{T_0} = \int_{T_0}^{T_1} \langle F^*(T) \rangle \, d(1/T)\end{aligned} \tag{2.39}$$

Canonical Monte Carlo (MC) simulation is implemented to calculate $\langle F^*(T) \rangle$ when $F^*(\sigma, T)$ is known in a compact form (see equation (2.29)). Helmholtz free energy at the initial point of integration (2.35) is chosen to be a convenient point, where F_0 can be computed analytically. To this end, the mean field approximation limit at high temperature is used as the starting point for integration in equation (2.35) [73]. The Helmholtz free energy at high temperatures can be calculated analytically.

High Temperature Limit- Mean Field Approximation

At high enough temperatures, each site on a *group* of sites is equally likely to be occupied by an atom. This is a constrained random situation, where each *group* of sites is occupied by only one atom and differs from a complete random case where all the sites can be equally likely occupied by different atomic species or vacancies. In this case, the average correlation associated with each cluster α included in the equation (2.29) can be calculated analytically.

We use the mean-field approximation (MFA) at high temperature limit to obtain average correlations associated with each cluster α

$$\bar{\Pi}_{\alpha,\mathtt{m}fa} = \left\langle \prod_i S_i \right\rangle_{\alpha'} \tag{2.40}$$

By substituting the above average correlations in (2.29), the constrained vibrational free energy at the high-temperature limit is obtained. This value, denoted by $F^*_{\mathtt{mfa}}$, is an upper limit for constrained vibrational free energy in equation (2.29), and only depends on the system properties, in this case, m_α and J_α.

To determine the total free energy at the high temperature limit, the entropy of the system has to be calculated. By considering the number of possible states for the system, w, entropy of the system is obtained accordingly.

$$S_{\mathtt{mfa}} = k_B \ln(w) \tag{2.41}$$

where $S_{\mathtt{mfa}}$ is the entropy per atom at the high temperature limit and it only includes configurational entropic effect. The total free energy per atom at MFA limit is then calculated.

$$F_{\mathtt{mfa}}(T) = F^*_{\mathtt{mfa}} - TS_{\mathtt{mfa}} \tag{2.42}$$

The above equation is used at very high temperatures, where the MFA is valid. In order to obtain high enough temperatures where the above equation is valid, we conduct a set of Monte Carlo simulations on the system and obtain the temperature where the upper limit in F^* is reached within a given accuracy. The obtained value from the above equation is used as an initial point in the integration (2.35).

In figure 2.12, the average vibrational free energy for an example system of Ti is calculated from a desired temperature, T_1, up to the high temperature limit. It is readily observed that $\langle F^*(T) \rangle$ is approaching its upper limit at high enough temper-

atures, which is defined as $F^*_{\texttt{mfa}}$. This upper limit replicates the analytically obtained value, replacing the analytical average correlation calculated in equation (2.40) back into the cluster expansion of vibrational free energy (2.29).

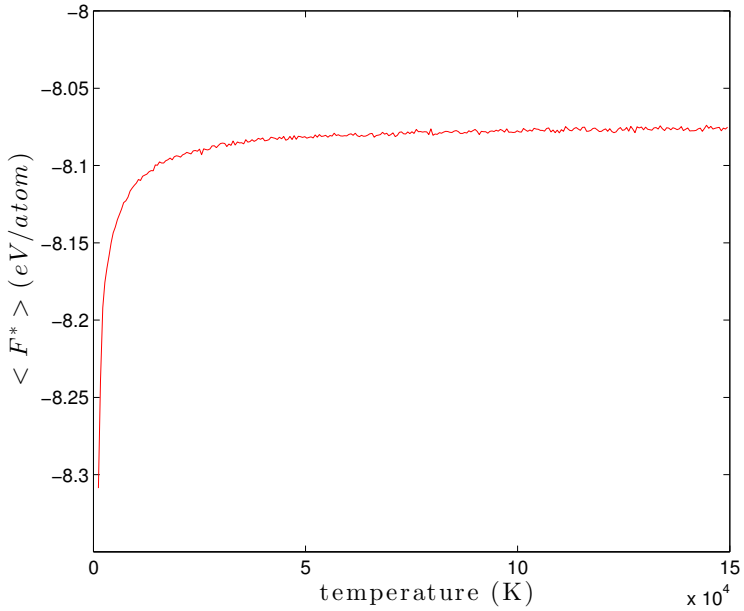

Figure 2.12: Average vibrational free energy for an example system of bcc Ti, calculated using Monte Carlo simulation from $1200K$ to $150000K$. The upper limit at high enough temperatures is the mean-field approximation limit.

Any thermodynamic process that connects the initial state to the final state can be integrated to calculate the free energy according to equation (2.35). Because the integration starts from a high temperature limit, a large portion of the integration path falls in a temperature range away from the temperature range of interest. In order to avoid calculating $\langle F^*(T)\rangle$ at temperatures far from the temperature range of interest, the ECIs are kept constant (at their value at the desired temperature, T_1) along the thermodynamic integration path, while the temperature the system experiences varies from the high temperature reference to the temperature of interest (which is why the integrand in (2.35) is $\langle F^*(T)\rangle$ rather than $\langle U^*(T)\rangle$). Only at the end of the integration path, free energy represents that of a real physical system. Therefore, two different temperatures have to be recognized here; one is the Monte

Carlo temperature which defines the path from MFA limit to desired temperature, and the other is the temperature for which the cluster expansion is fitted. For each desired temperature with a fitted cluster expansion, a Monte Carlo temperature path from high temperature to the desired temperature is conducted in order to obtain total free energy at the desired temperature.

A general and robust scheme to determine the free energy of mechanically unstable but dynamically stabilized phases is presented in chapter 2. The application of this method to transition metals of group IV, Ti and Zr, at high temperature phase of bcc and ordered compounds, PtTi, at high temperature phase of $B2$ is presented in chapters 3 and 4. The proposed method also offers a natural avenue to handle alloys since the cluster expansion method can easily allow for multiple species on each site of the augmented lattice introduced herein.

A summary of the presented scheme is shown in figure 2.13.

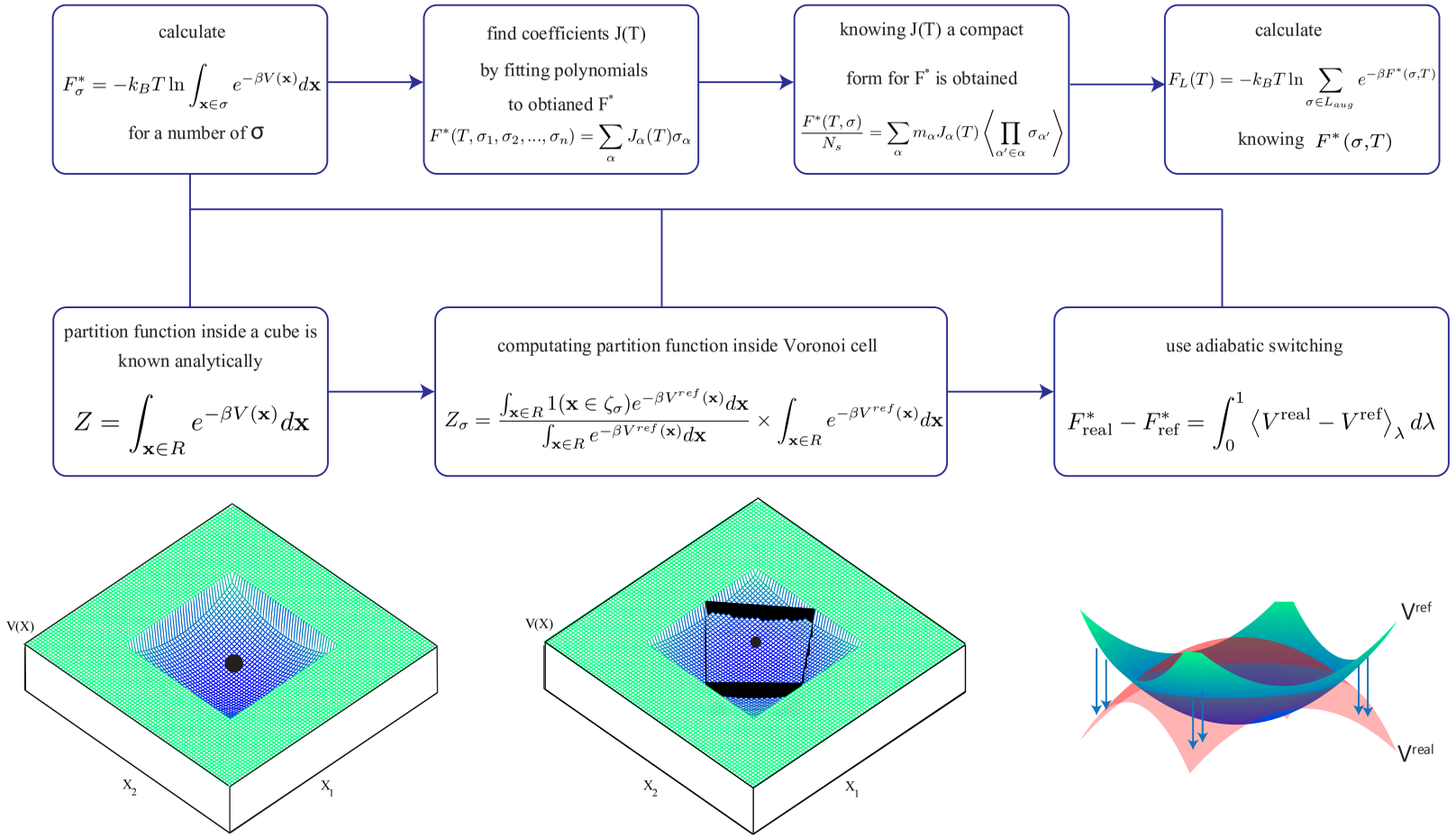

Figure 2.13: A summary of the presented scheme in chapter 2.

Chapter Three

Transition Metals

3.1 Introduction

All transition metals of group III to VI exhibit a stable body-centered cubic (bcc) phase across a temperature range and at ambient pressure. Taking melting point and temperature range of existence as a rough estimate of stability, as indicated in table 3.1 [56], stability decreases from group VI to III.

3	4	5	6
Sc $T_0 = 1337°C$ $T_m = 1539°C$	Ti 883 1660	V 1890	Cr 1857
Y 1478 1522	Zr 862 1852	Nb 2468	Mo 2617
La 865 918	Hf 1742 2227	Ta 2996	W 3410

Table 3.1: Melting temperature, T_m, and transition temperature to bcc phase, T_0, for group III to VI. Transition metals of group V and VI indicate a stable bcc phase over the whole temperature range. Taking T_m and the range of stability, $T_m - T_0$, as a crude estimate of bcc phase stability, stability increases from group III to VI. The melting temperatures and transition temperatures are obtained from ref [56].

Another reflection of gradation from weak to stable bcc phase in group III to VI transition metals is the decrease of self-diffusion in transition metals going from group III to VI. Group VI metals show a relatively slow self-diffusion while group III or IV metals are known for their fast self-diffusion [57].

In all metals of group III and IV, a martensitic transformation to hexagonal closed-packed (α) phase is observed upon lowering the temperature (and at ambient pressure). For group IV metals, a second martensitic transformation to a hexagonal (ω) phase is observed upon increasing pressure [64].

In order to better understand the stability of bcc phase of these metals, it is of important interest to know the phonon dispersion. It is expected that the phonon

dispersion curve of group IV metals (here for Ti and Zr) reflects the tendency of the system toward the martensitic transformation into α and ω phases, upon lowering temperature and increasing pressure, respectively.

As briefly described in the previous chapter, in order to obtain the phonon dispersion relation for a lattice, a set of wavelike solutions for the displacement of atoms from their ideal position (lattice site position) is considered to solve the equation of motion (see equation (2.4)). For a periodic system, the displacement of atom κ in cell n in direction i from its equilibrium lattice position, $u_{n\kappa i}$, is expressed in terms of a plane wave with respect to the unit cells coordinates in the lattice:

$$u_{n\kappa i} = \frac{1}{\sqrt{M_\kappa}} u_{\kappa i}(\vec{\mathbf{q}}) e^{i(\vec{\mathbf{q}}.\vec{\mathbf{r}}_n - \omega t)} \tag{3.1}$$

where M_κ is the mass of atom κ, $\vec{\mathbf{q}}$ is the wave vector, $\vec{\mathbf{r}}_n$ is the position of unit cell n in the lattice, ω is the frequency and t is time. $u_{\kappa i}$ is the i component of a vector called the polarization vector of the normal mode. In contrary to a normal plane wave, the above plane wave is only defined at cell positions $\vec{\mathbf{r}}_n$.

For a system consisting of N unit cells with r atoms in each, a total number of $3Nr$ equations of motion of the following form exist:

$$M_\kappa \ddot{u}_{n\kappa i} + \sum_{m\kappa' j} \Phi_{n\kappa, m\kappa'}(i,j) u_{m\kappa' j} = 0 \tag{3.2}$$

where Φ is the force constant tensor, defined in equation (2.2). By substituting the plane wave solution in equation (3.1) into the above equation of motion and reordering the summation terms, the following set of equations are obtained

$$-\omega^2 u_{\kappa i}(\vec{\mathbf{q}}) + \sum_{\kappa' j} \underbrace{\sum_m \frac{1}{\sqrt{M_\kappa M_{\kappa'}}} \Phi_{n\kappa, m\kappa'}(i,j) e^{i\vec{\mathbf{q}}.(\vec{\mathbf{r}}_m - \vec{\mathbf{r}}_n)}}_{D_{\kappa i, \kappa' j}(\vec{\mathbf{q}})} u_{\kappa' j}(\vec{\mathbf{q}}) = 0 \tag{3.3}$$

where n and m run over different cells, κ and κ' run over different atoms within a unit cell and i and j run over different components. The summation in the brace is defined as the dynamical matrix, which is independent of n or of the position of unit cell. By defining Dynamical matrix, the above set of equations reduces to a set of $3r$ coupling equation of the following form.

$$-\omega^2 u_{\kappa i}(\vec{\mathbf{q}}) + \sum_{\kappa' j} D_{\kappa i,\kappa' j}(\vec{\mathbf{q}}) u_{\kappa' j}(\vec{\mathbf{q}}) = 0 \tag{3.4}$$

The above system of equations has the following eigen-solutions.

$$Det\{D_{\kappa i,\kappa' j}(\vec{\mathbf{q}}) - \omega^2 \mathbf{I}\} = 0 \tag{3.5}$$

This equation has $3r$ different solutions for each $\mathbf{q}$. The relation between $\omega(\mathbf{q})$ and $\mathbf{q}$ is known as the dispersion relation and is usually depicted via a curve along the high symmetry branches in k-space in the first Brillouin zone.

The phonon dispersion curve for bcc Ti at $0K$, computed using *Phonopy* toolkit [69], is indicated in figure 3.1. When compared to the phonon dispersion curve of group V and VI transition metals, such as bcc Mo [18, 90], two anomalies are evident for group IV metals (as presented herein for bcc Ti and bcc Zr). The first is the existence of an extreme dip along the longitudinal branch close to $\xi = 2/3[111]$, and the second is the negative frequencies associated with the transverse branch along $\Gamma - N$ direction. These anomalies are explained in more detail in the succeeding section.

As shown in figure 3.1, there exist negative frequencies associated with mechanical instabilities for bcc Ti at $0K$. For the longitudinal phonon branch along the $[\xi\xi\xi]$ direction, there exists an extreme dip close to $\xi = 2/3$. For the transverse phonon branch along the $[0\xi\xi]$, there is a minimum located at the high symmetry point N (the Brillouin-zone boundary at $\mathbf{q} = [011]$). The atomic displacements associated with these two phonon modes have a special crystallographical meaning [22].

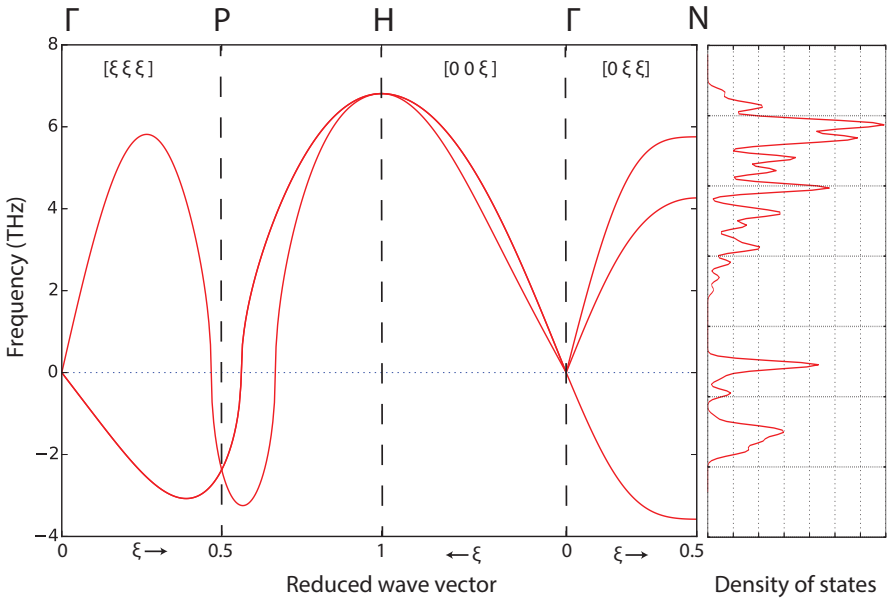

Figure 3.1: a) Phonon dispersion curve for bcc phase of Ti computed at equilibrium lattice parameter $3.2464\mathring{A}$ and temperature $0K$. The imaginary frequencies of the unstable modes are plotted as negative values. The extreme dip in the longitudinal phonon along the $[\xi\xi\xi]$ branch is located close to $\xi = 2/3[111]$ in reduced wave vector space. The atomic displacement due to this point in the dispersion curve corresponds to the martensitic transformation from bcc to ω. The other minimum along the transverse brach at point N results in an atomic displacement which is related to the martensitic transformation from bcc to hcp. b) Phonon density of states.

As shown by de Fontaine and Buck [14], the atomic displacement due to the first phonon mode is associated with the movement of neighboring (111) planes, in such a way that two of the neighboring planes move toward each other and every third plane stays at rest. When the two neighboring planes collapse, ω phase structure is obtained.

In order to obtain the atomic displacement associated with a specific phonon mode, the following equation is employed to calculate the spatial part of the atomic displacement

$$u_i(\kappa n) = \frac{1}{\sqrt{M_\kappa}} e_i(\kappa, \mathbf{q}) e^{2\pi i \mathbf{q}.\mathbf{r}(\kappa n)} \tag{3.6}$$

where $e_i(\kappa, \mathbf{q})$ is the i component of the eigenvector solution of equation (3.5) for atom κ at $\mathbf{q}$. The eigenvector associated with the negative eigenvalue (or imaginary

frequency) at $\mathbf{q} = 2/3[111]$ is $e(\mathbf{q}) = [\sqrt{3}/3, -\sqrt{3}/3, -\sqrt{3}/3]$, which results in an atomic displacement illustrated in figure 3.2.

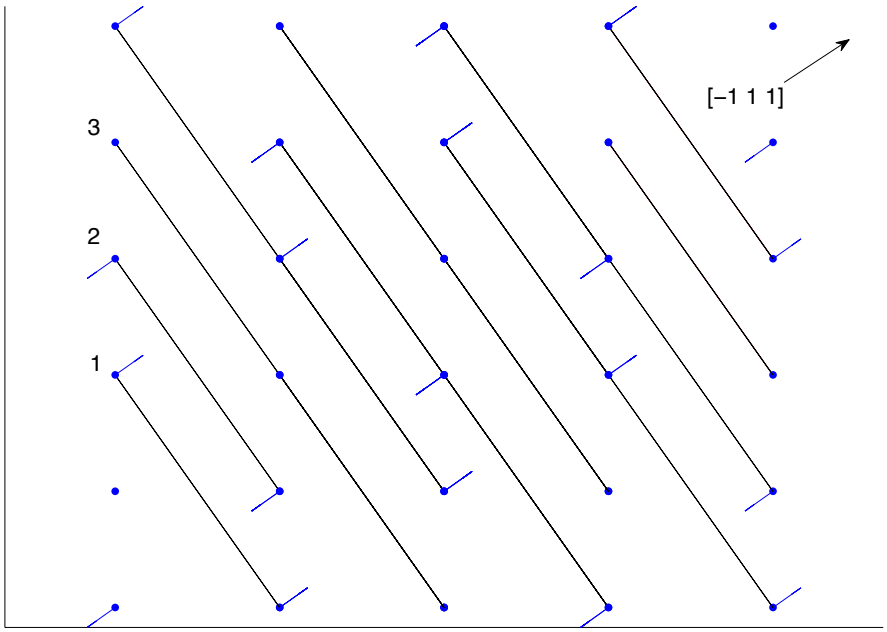

Figure 3.2: The atomic movement associated with the longitudinal phonon at $\mathbf{q} = 2/3[111]$. This atomic displacement results in movement of two neighboring (111) planes, whereas every third plane stays at rest. The normal vector to the display page is in $[1\bar{1}0]$ direction.

The second minimum in the dispersion curve in 3.1 is located at N. The atomic movement associated with this phonon mode is obtained similarly to the first phonon mode. As shown in figure 3.3, this atomic displacement results in the movement of neighboring (110) planes in opposite $[1\bar{1}0]$ directions. As shown by Burgers [8], the aforementioned movement of atoms is related to bcc-to-α martensitic transformation.

It has been shown by Petry *et al.* that $\mathbf{L}\frac{2}{3}(1,1,1)$ phonon does not change over the whole temperature range of bcc and normal pressure [56]. This suggests that the weakness of bcc phase toward ω is inherent to the bcc structure and can be explained geometrically [56]. From all the phonons along the $\mathbf{L}(1,1,1)$ branch, only the phonon at $\xi = \frac{2}{3}$ does not change the distance between nearest neighbor (NN) chain of atoms along the [111] direction. Since the distance between atoms is the shortest along the

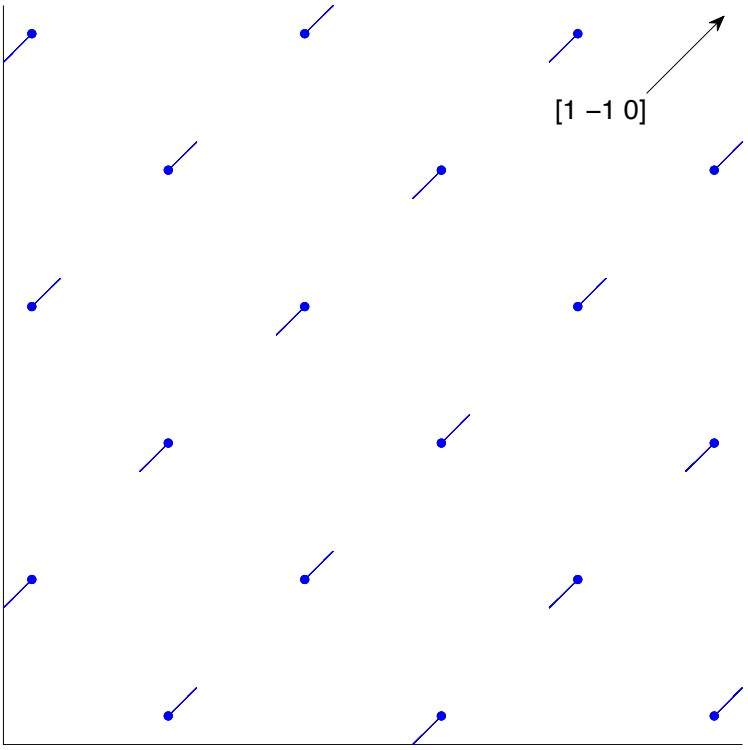

Figure 3.3: The atomic movement associated with the transverse phonon at N. The eigenvector associated with this phonon mode is $e(\mathbf{q}) = [-\sqrt{2}/2, 0, \sqrt{2}/2]$. This atomic displacement results in movement of neighboring (110) planes in opposite $[1\bar{1}0]$ directions. For a displacement magnitude of $a\sqrt{2}/12$, the hcp stacking sequence is obtained (where a is lattice constant). The normal vector to the display page is in [001] direction.

[111] direction, the restoring force along this direction is the largest. Other phonons compress the distance between NN chain of atoms, thus giving raise to the restoring forces, their frequencies (or energies) are higher, whereas the phonon that does not alter the distance between NN chain of atoms has a lower frequency.

The general weakness of $\mathbf{L}\frac{2}{3}(1,1,1)$ phonons for all bcc phases from a geometrical point of view cannot explain the fact that the dispersion curve of group V and VI transition metals is devoid of this weak phonon mode [63]. One has to pay attention to the electronic structure, as d-electron bonding is playing a role. As d orbitals get filled up moving from group IV to VI, the d bond twists its direction from concentration along [111] direction in such a way that it opposes the shear movement

among the neighboring [111] chains [25]. In group IV metals, the charge density of the d electrons is concentrated along [111] direction which amplifies the geometrical weakness of $\mathbf{L}\frac{2}{3}(1,1,1)$ phonon. However, in group VI metals, the d electron charge concentration is tangled in a way that opposes the shear movement of NN [111] chains, thus stiffening the $\mathbf{L}\frac{2}{3}(1,1,1)$ phonon [25].

Similarly, the phonon dispersion curve and density of states for bcc phase of Zr at

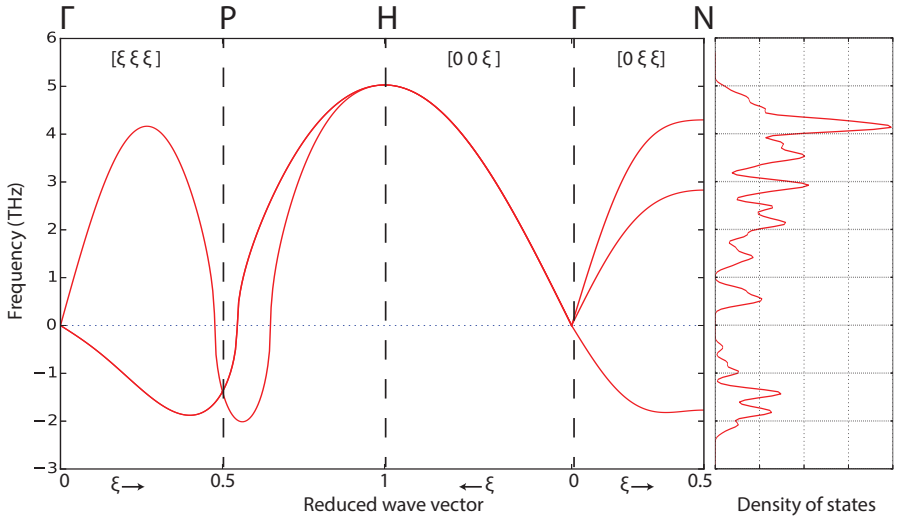

Figure 3.4: a) Phonon dispersion curve for bcc phase of Zr computed at equilibrium lattice parameter $3.574\mathring{A}$ and temperature $0K$. The imaginary frequencies of the unstable modes are plotted as negative values. The extreme dip in the longitudinal phonon along the $[\xi\xi\xi]$ branch is located close to $\xi = 2/3[111]$ in reduced wave vector space. The atomic displacement due to this point in the dispersion curve corresponds to bcc-to-ω martensitic transformation. The other minimum along the transverse brach at N results in an atomic displacement which is related to the bcc-to-hcp martensitic transformation. b) Phonon density of states.

$0K$ is illustrated in figure 3.4.

Considering the mechanical instabilities associated with the bcc phase of group IV transition metals, it is clear that large vibrational entropy causes mechanically unstable phases to become thermodynamically stable at finite temperatures. These phases become thermodynamically favorable at high enough temperatures because they constantly undergo local distortions towards many possible similar low-symmetry structures, which in turn produces large stabilizing entropic contributions to the free

energy [93].

The thermodynamic and mechanical properties of such phases are inaccessible to the standard lattice dynamic calculations, thus making their vibrational entropy undefined and imposing particular challenges for first-principles simulation. (Quasi)-harmonic approximation, used in common statistical approaches for free energy calculation at finite temperature, inhibits free energy calculation of phases with mechanical instabilities. To define the free energy of such phases accurately, a rigorous investigation of vibrational excitations is essential.

In this chapter, the free energy of bcc phase of Ti and Zr are calculated using the method presented in chapter two of the presented thesis. The results are then compared to the molecular dynamics (MD) and the National Institute of Standards and Technology (NIST) condensed phase experimental thermodynamic data [9, 11]. All computational details incorporated in these calculations are presented in the section *Computational Details* of each corresponding chapter.

3.2 Free energy calculation of bcc phase of Ti and Zr

The augmented lattice includes not only the ideal bcc sites, but also the sites corresponding to configurations that are local energy minima near the ideal bcc structure. These additional sites can be found via the identification of unstable modes through a standard lattice dynamics analysis, followed by a full relaxation calculation using, as the initial configuration, bcc structures slightly distorted along the various unstable modes. As discussed in the previous section, in the case of bcc Ti and bcc Zr, the unstable modes have been previously well-characterized [21, 56] and consist of longi-

tudinal [$\xi\xi\xi$] phonons with $\xi = 2/3$. The movement of atoms along the displacement associated with $\mathbf{T}(0, \xi, \xi)$ phonon results in no nearby local minima in case of bcc Ti and Zr. Therefore, only the displacement of atoms along $\mathbf{L}\frac{2}{3}(1, 1, 1)$ phonon is considered.

As shown in figure 3.5 the energy per atom for different displacements along $\mathbf{L}\frac{2}{3}(1, 1, 1)$ phonon is calculated using first principle electronic structure calculation. A supercell consisting of 54 Ti/Zr atoms is displaced along $\mathbf{L}\frac{2}{3}(1, 1, 1)$ phonon for a different number of d/a values, and the volume of the cell is relaxed at each displacement. a denotes the relaxed lattice constant of the supercell.

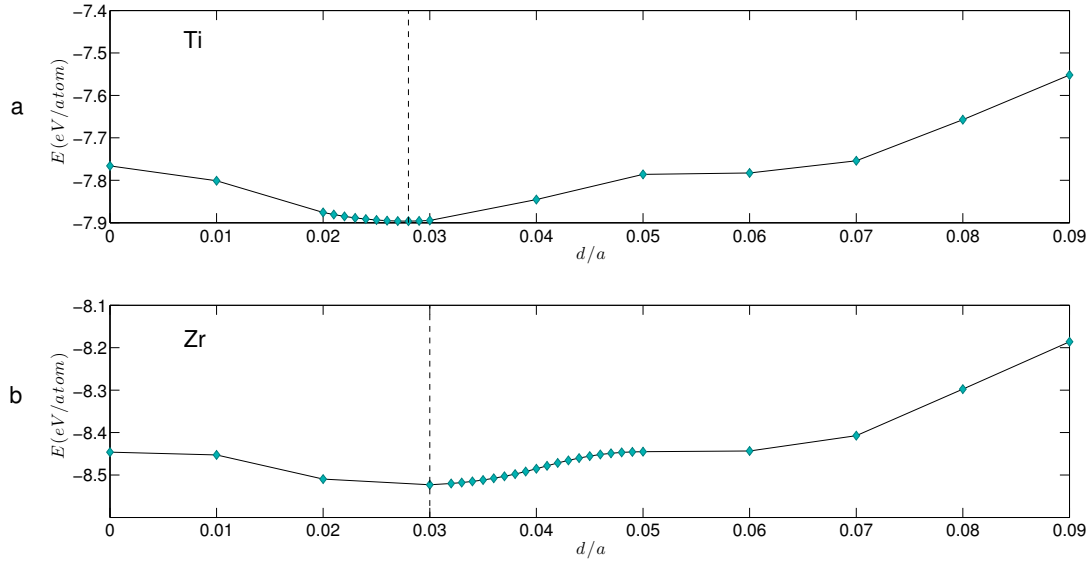

Figure 3.5: a) Energy per atom versus displacement (d) along $\mathbf{L}\frac{2}{3}(1, 1, 1)$ phonon of bcc Ti with lattice constant a. There exists a minimum located at $d/a = 0.028$. b) Energy per atom versus displacement (d) along $\mathbf{L}\frac{2}{3}(1, 1, 1)$ phonon of bcc Zr with lattice constant a. There exists a minimum located at $d/a = 0.03$.

The minimum along the energy-displacement curve could be considered as the local minimum to determine the location of the first off-bcc site. This particular position of the atoms is denoted by $\mathbf{x}_g$, where the ideal bcc position is denoted by $\mathbf{x}_{bcc}$. The augmented lattice supercell is constructed by operating the symmetry point group of bcc (O_h point group) to a lattice including both sites at $\mathbf{x}_g$ and $\mathbf{x}_{bcc}$. This will

result in a cell consisting of a bcc site, as well as eight other sites, each of which is located on a corner of a cube centering at bcc lattice point.

For the movement of atoms to represent the $\mathbf{L}\frac{2}{3}(1,1,1)$ phonon, the supercell should, at least, consist of three sets of (111) planes or a third multiple of (111) planes. This is necessary because of the periodic boundary condition. In our calculations, a $3\times3\times3$ supercell with the bcc conventional cell as the unit cell is used (each bcc unit cell consists of two Ti or Zr atoms). This results in 54 bcc sites, therefore the augmented lattice cell consists of $54\times9=324$ sites, including both the bcc and the corner sites. The augmented lattice consists of *groups* of sites surrounding each bcc site, when each Ti atom can only occupy one of the sites in each *group* of sites. This model simulates the hopping of atoms around bcc sites. By creating the augmented lattice, which imposes some extra lattice sites to the familiar bcc lattice, phase space is partitioned into different configurations. A configuration, σ, is a possible assignment of Ti/Zr atoms and vacancies (Vac) to the augmented lattice sites, in such a way that each *group* of sites is occupied by one Ti/Zr atom and eight vacancies.

The constrained vibrational free energy, F^*_σ, is calculated for a number of different configurations, using equations (2.17) to (2.28). The calculated vibrational free energy for this set of configurations is then used as a training data set, in order to obtain a relation for F^*_σ as a function of σ.

For a system consisting of N atoms, the portion of phase space associated with a configuration σ, defined as ζ_σ in chapter 2, is the multiplication of N $3d$ Voronoi cells, created using lattice sites as the generating points. Figure 3.6 illustrates the Voronoi tessellation of spatial phase space with augmented lattice sites as generating points in the periodic boundary condition. ζ_σ is the multiplication of those cells with atoms sitting on their generating lattice sites.

As discussed in the previous chapter, the vibrational free energy is calculated for a reference system with an isotropic positive definite force constant (see equation

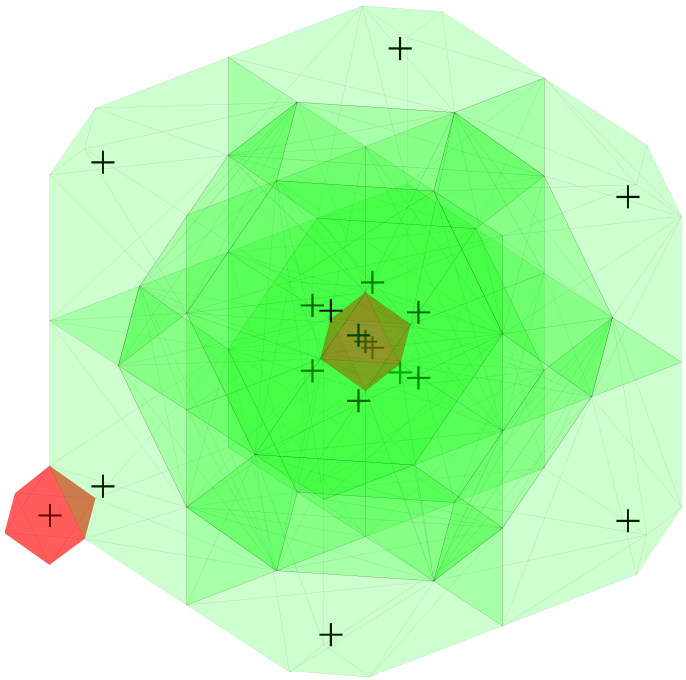

Figure 3.6: Representation of Voronoi tessellation of 3-dimensional spatial space, using augmented lattice sites as generating points, in the periodic boundary condition. The Voronoi cells along the faces of the supercell are generated considering the repetition of lattice sites periodically. The red Voronoi cells are associated with bcc lattice sites, whereas the green cells are associated with corner sites.

(2.22)). Then, the vibrational free energy of the real system is calculated by switching the reference potential to the real potential adiabatically, and by calculating the free energy difference between these two states (see equation (2.28)). Therefore, the vibrational free energy of a configuration σ consists of the following terms

$$F_{\sigma}^{*} = -k_B T \log Q + \int_0^1 < \hat{V}(\mathbf{x}, 1) - \hat{V}(\mathbf{x}, 0) >_{\lambda} d\lambda \tag{3.7}$$

where Q is the partition function defined in equation (2.19). In case of a monatomic system, the partition function is formulated as

$$Q = (\frac{2\pi m k_B T}{h^2})^{\frac{3N}{2}} \times Z_{\sigma} \tag{3.8}$$

where Z_σ is defined in equation (2.18). The configuration partition function for an isotropic reference system, with its potential defined in equation (2.22), reduces to the following form

$$Z_\sigma = \frac{\int_{\mathbf{x}\in R} 1(\mathbf{x}\in\zeta_\sigma) e^{-\beta V(\mathbf{x})} d\mathbf{x}}{\int_{\mathbf{x}\in R} e^{-\beta V(\mathbf{x})} d\mathbf{x}} \times \int_{\mathbf{x}\in R} e^{-\beta V(\mathbf{x})} d\mathbf{x} = \left(\frac{n_{VC}}{n_{MC}}\right) \times e^{-\beta V_0} \prod_{i=1}^{3N} \int_{-\infty}^{\infty} e^{-\frac{1}{2}\beta C_i x_i^2} dx_i = e^{-\beta V_0} \left(\frac{n_{VC}}{n_{MC}}\right) \times \left(\frac{2\pi k_B T}{C}\right)^{\frac{3N}{2}} \tag{3.9}$$

where n_{VC} is the number of Monte Carlo states inside ζ_σ, n_{MC} is the total number of Monte Carlo steps, and C_i is the second derivative of reference potential with respect to the i degree of freedom (which are all equivalent in an isotropic system). Consequently, the constrained vibrational free energy for a configuration σ reduces to the following form

$$F_\sigma^* = V_0 \underbrace{-k_B T \ln\left(\frac{n_{VC}}{n_{MC}}\right)}_{\text{ratio term}} \underbrace{-3Nk_B T \ln\left(\frac{2\pi k_B T}{h}\sqrt{\frac{m}{C}}\right)}_{\text{reference term}} + \underbrace{\int_0^1 < \hat{V}(\mathbf{x},1) - \hat{V}(\mathbf{x},0) >_\lambda \, d\lambda}_{\text{switching term}} \tag{3.10}$$

V_0 is the real potential energy value at the minimum within ζ_σ, as defined in equation (2.15) and (2.22).

Table 3.2 indicates different terms in equation (3.10), calculated for two different configurations. The ratio of the number of states inside ζ_σ to the total number of MC states is close to one, because of the stiffness of the reference potential. The contribution of the term $-k_B T \ln\left(\frac{n_{VC}}{n_{MC}}\right)$ is very close to zero, and as mentioned before, the domain of integration for the reference system can be extended to infinity. In order to increase the practicality of the method, it is preferable to increase the value for C as much as needed to make the contribution of $-k_B T \ln\left(\frac{n_{VC}}{n_{MC}}\right)$ negligible. This criterion is used in the presented calculations in order to adjust the value of C. As demonstrated in table 3.2,the larger ratio for Zr compared to Ti for the same value

of C is due to the larger atomic distance in bcc Zr compared to bcc Ti, and to the consequent larger volume ζ_σ assigned to each configuration in bcc Zr.

	V_0	ratio	reference	switching	total
σ_1	-422.788	0.910	-14.896	-6.767	-444.442
σ_2	-457.361	0.993	-20.198	-8.877	-486.435

Table 3.2: The calculated values for different terms in equation (3.10) for σ_1, a configuration consisting of 54 Ti atoms, and σ_2, a configuration consisting of 54 Zr atoms. The energy values are in units of eV. The reference potential for both configurations is defined as an isotropic potential well with $C = 20eV/\mathring{A}^2$.

In our calculations, 34 different clusters are included in the cluster expansion (see equation (2.29)) for both bcc Ti and bcc Zr. There is one empty cluster (which is the constant term in the polynomial series) and there are two point clusters (one is a bcc point cluster and one is a corner point cluster), along with 31 pair clusters. As shown in figure 2.9, four of these pair clusters connect the sites in each *group* of nine sites (one bcc site and eight corner sites), whereas the other 27 pairs join one site on a *group* to another site in the nearest neighbor *group* (defined as short-pairs and long-pairs, respectively). The four short-pairs include a half diagonal pair, an edge pair, a face diagonal pair and a diagonal pair of the cube formed by eight corner sites and one bcc site in the center. This choice of clusters is adequate in capturing configuration variations and is capable of defining the configurational dependence of vibrational free energy. All of the ECIs associated with these clusters are fitted using the training data set except for those ECIs associated with short-pairs. These four pairs have to be treated differently in our scheme, because they are undesirable pairs that have to be precluded during Monte Carlo simulations. To this end, some large value ECIs are imposed to these pair clusters such that no more than one Ti/Zr atom can occupy each *group* of sites. Moreover, these large ECIs impose no energy penalty if one Ti/Zr atom occupies each *group* of sites.

A set of temperature-dependent ECIs, $\{J(T)\}$, is fitted over a training data set at

different temperatures, employing the Alloy-Theoretic Automated Toolkit (ATAT) (see equation (2.29)) [72, 74, 75]. Constrained vibrational free energies for a number of different configurations, F^*_σ, calculated by the presented scheme, constitute the training data set. The training data set always includes the configuration associated with atoms sitting on x_g or the local minimum nearby the bcc structure. Other configurations are selected by random displacement of a number of atoms (for example, one or two or ten atoms) from the minimum position x_g. Different number of deviations from the minimum configuration is considered, such that a sufficient range of energy fluctuations is observed inside the training data set.

Monte Carlo simulation is carried out to calculate the ensemble average of constrained vibrational free energy, $\langle F^*_\sigma \rangle$, with equation (2.29), once the set of $\{J(T)\}$ is known, utilizing MultiComponent Easy Monte Carlo Code (memc2) [72]. Starting from a relatively small training data set, the cluster expansion is improved by adding new configurations to the data set. Figure 3.7(a) illustrates the average vibrational free energy for a number of different fits (sets of $\{J(T)\}$) at $1200K$ for Ti. Each fit has a different number of configurations within its training data set. For each fit, $\langle F^*_\sigma \rangle$ value is physical only at temperatures approaching $1200K$, since the ECIs of the fit correspond to this temperature. However, the MC temperature is allowed to vary over a temperature range, starting at $1200K$ up to the high temperature limit. As temperature increases, the average vibrational free energy for all fits converges to a limit, which is the high temperature mean field approximation (MFA) for the system. The limit obtained by Monte Carlo simulations replicates the analytical values obtained in the following section.

In fit-1, there exists a local minimum in the average vibrational free energy at temperatures close to 4000 K, while one expects the average vibrational free energy to increase monotonically with temperature for a well-converged fit. The observed local minimum implies that a relatively large number of ECIs are over-fitted over a

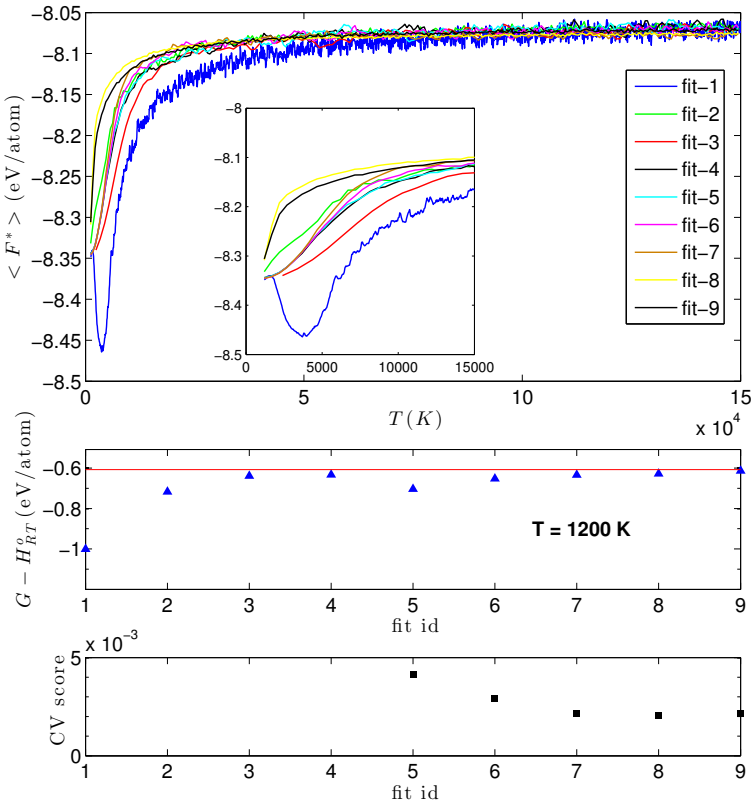

Figure 3.7: a) Average vibrational free energy vs temperature. fit-1 includes 38 data points, fit-2 to fit-5 includes 52, 53, 54 and 55 data points respectively. fit-6 to fit-9 contain 63, 73, 86 and 98 data points. b) Gibbs free energy with reference to hcp Ti at room temperature, obtained using the presented scheme for different fits, shown by diamonds, and NIST data at 1200 K shown by the horizontal line. c) The cross-validation score associated with each fit at 1200 K. The CV score for fit-1 to fit-4 is undefined because of the collinearity of correlation vectors associated with the corresponding data set.

small number of data points. Thus, the fit is improved by including in the data set the configuration corresponding to the new observed local minimum. As depicted in figure 3.7(a), fit-2 no longer predicts any local minimum. New data points are added to a fit until the set of ECIs converges and the performance of the fit is satisfactory. The performance of the fits, evaluated by the cross-validation (CV) score (see equation (2.30)), is improved by increasing the number of data points from fit-1 to fit-8. The CV score associated with each fit is shown in figure 3.7(c). The CV score for fit-2, fit-3 and fit-4 is undefined because of the collinearity of correlation vectors associated with the corresponding data set.

In figure 3.7(b), it is readily observed that the obtained free energy with our method converges to the NIST value (the red line) as the fit performance improves from fit-1 to fit-9. The detailed explanation for comparing the presented method free energy with NIST experimental data is outlined in the *validation* section of this chapter.

In order to obtain the free energy of a system for which the cluster expansion of vibrational free energy is known, the average vibrational free energy is integrated according to equation (2.35). Canonical MC simulation is carried out over a range of temperature, from high temperature or mean-field limit (the initial point in integration) down to the desired temperature (where the cluster expansion is fitted), employing MultiComponent Easy Monte Carlo Code (memc2) [72].

At high enough temperatures, each site on one *group* of sites (each *group* of one bcc site and eight corner sites) is equally likely to be occupied by a Ti/Zr atom (this is a constrained random situation, where each *group* of sites is occupied by only one Ti/Zr atom and differs from a complete random case where all the sites can be equally likely occupied by Ti/Zr or vacancies).

In the mean field approximation (MFA) limit, the average correlation associated with each of these clusters (see equation (2.29)) is calculated as the following, if an occupation value of +1 and -1 is assigned to Ti/Zr and vacancies, respectively.

$$
\begin{aligned}
&\text{empty} && = 1\\
&\text{bcc point} && = 8/9 \times -1 + 1/9 \times 1 = -7/9\\
&\text{corner point} && = 8/9 \times -1 + 1/9 \times 1 = -7/9\\
&\text{half-diag pair} && = 8/9 \times (-7/8 + 1/8) + 1/9 \times (-8/8) = 5/9\\
&\text{edge pair} && = 8/9 \times (-3/12 + 9/12) + 1/9 \times (12/12) = 5/9\\
&\text{face-diag pair} && = 8/9 \times (-3/12 + 9/12) + 1/9 \times (12/12) = 5/9\\
&\text{diag pair} && = 8/9 \times (-1/4 + 3/4) + 1/9 \times (4/4) = 5/9\\
&\text{long pairs} && = 1/81 \times 1 + 64/81 \times 1 + 2 \times 8/81 \times -1 = 49/81
\end{aligned}
$$

By substituting the above average correlations in equation (2.29), the constrained

vibrational free energy at hight temperature limit ($F^*_{\texttt{mfa}}$) is obtained. Table 3.3 demonstrates the high temperature vibrational free energy obtained for bcc Ti and bcc Zr.

To determine the total free energy at high temperature limit, the entropy of the system has to be calculated. By considering the number of possible states for the system, w, entropy of the system is obtained accordingly. For each Ti/Zr atom, the number of possible states is equal to the number of ways to select a site from a *group* of sites, which in this case equals nine. Consequently, the entropy is obtained according to the following equation.

$$s = k_B \ln(w) = k_B \ln(9) \tag{3.11}$$

where s is the entropy per atom. Free energy per atom at MFA limit is then calculated.

$$F_{\texttt{mfa}}(T) = F^*_{\texttt{mfa}} - Ts \tag{3.12}$$

The above equation is valid for $T > T_{mfa}$, where T_{mfa} is the mean field approximation temperature. T_{mfa} is obtained by conducting a set of Monte Carlo simulations on the system and obtaining the temperature where the upper limit in F^* is achieved, as shown in figure 3.7(a). The obtained values for $F^*_{\texttt{mfa}}$ and $F_{\texttt{mfa}}$ for bcc Ti and bcc Zr, for a cluster expansion fitted at $1200K$, are presented in table 3.3.

Table 3.3: The average constrained vibrational free energy and free energy value obtained at high temperature ($1.5 \times 10^5 K$) for bcc Ti and bcc Zr.

	$F^*_{\texttt{mfa}}$(eV/atom)	$F_{\texttt{mfa}}$(eV/atom)
Ti	-8.0738	-36.4751
Zr	-8.8183	-37.2196

Using $F_{\texttt{mfa}}$ as the initial point of integration in equation (2.35), the free energy of bcc Ti and bcc Zr are calculated. The values obtained for free energy of bcc Ti and

bcc Zr at different temperatures are listed in table 3.4 and 3.5, respectively.

Table 3.4: Gibbs free energy values of bcc Ti with reference to the enthalpy of hcp Ti at room temperature (RT), obtained using the presented scheme. $F(T)$ is the polynomial fit for bcc Ti free energy, valid for $1200 < T < 1800$. H^o_{RT} is the enthalpy at RT for hcp Ti.

T(K)	1200	1400	1600	1800
$G - H^o_{RT}$(eV/atom)	-0.6131	-0.7779	-0.9473	-1.1246
$F(T)$(eV/atom)$=-8.5205 \times 10^{-4}T - 7.3904$				
$H^o_{RT} = -7.8086$(eV/atom)				

Table 3.5: Gibbs free energy values of bcc Zr with reference to the enthalpy of hcp Zr at room temperature (RT), obtained using the presented scheme. $F(T)$ is the polynomial fit for bcc Zr free energy, valid for $1200 < T < 1800$. H^o_{RT} is the enthalpy at RT for hcp Zr.

T(K)	1200	1400	1600	1800
$G - H^o_{RT}$(eV/atom)	-0.6903	-0.8569	-1.0298	-1.2096
$^*F(T)$(eV/atom)$=-8.527 \times 10^{-4}T - 8.12731$				
$^{**}H^o_{RT} = -8.4689$(eV/atom)				

3.3 Validation

In order to validate the obtained free energy of bcc Ti/Zr, we compare our results with molecular dynamics and National Institute of Standards and Technology (NIST) condensed phase experimental thermodynamic data [9, 11]. In order to first perform an internal consistency check of the method, a set of NVT molecular dynamics calculations are performed using VASP [36–39]. These MD simulations are carried out in order to trace the average internal energy of bcc Ti/Zr at different temperatures, and Helmholtz free energy is obtained by integrating the following thermodynamic relation

$$\left[\frac{\partial(F/T)}{\partial(1/T)}\right]_{V,N} = U \tag{3.13}$$

where U is the average internal energy, F is Helmholtz free energy, T is temperature, V is volume and N is the number of particles. The free energy obtained at 1200 K with the presented method is used as an initial point when integrating the above relation. The free energy of bcc Ti and bcc Zr obtained using MD are compared to our result in figure 3.8(a) and 3.9(a), respectively.

The enthalpy of hexagonal closed pack (hcp) Ti/Zr at room temperature (RT) is assigned as the reference point for energy to make our results comparable to NIST data. The fitfc code [72] is used to calculate the free energy and entropy of hcp Ti/Zr at room temperature, and the enthalpy of hcp Ti/Zr is then computed using the thermodynamic relation $H = F+TS+pV$. Presented NIST values are Gibbs free energies at zero pressure with reference to hcp Ti/Zr enthalpy at room temperature. The pressure may be nonzero at the volume which Helmholtz free energy, F, is calculated.

In order to obtain Gibbs free energy from the calculated Helmholtz free energy, second order pV work term correction is employed in accordance with the following equation.

$$
\begin{aligned}
&(\frac{\partial G}{\partial p})_T = V \\
&G_{p=p_0} - G_{p=0} = \int_{p=0}^{p=p_0} V dp = \begin{cases} V_0 p_0 & \text{first order} \\ 1/2(V_{p_0} + V_0)p_0 & \text{second order} \end{cases}
\end{aligned}
\tag{3.14}
$$

where G is Gibbs free energy, p is pressure and V is volume. p_0 is the pressure at volume V_{p_0}, in which the Helmholtz free energy is obtained, and V_0 denotes volume

at zero pressure.

$$\begin{aligned} G(T, p=0) &= G(T, p=p_0) - (\frac{V_{p_0}+V_0}{2})p_0 \\ &= F(T)\mid_{p=p_0} + V_{p_0}p_0 - (\frac{V_{p_0}+V_0}{2})p_0 \\ &= F(T)\mid_{p=p_0} + (\frac{V_{p_0}-V_0}{2})p_0 \end{aligned} \tag{3.15}$$

V_0 is obtained using ab initio MD calculations, by changing the volume of the supercell until pressure converges to zero.

As shown in figure 3.8(b) and 3.9(b), the presented method predictions for free energy of bcc Ti and bcc Zr at different temperatures agree perfectly well with NIST data.

Figure 3.10 shows the obtained free energy of bcc Ti (the red curve) and the calculated free energy of hcp Ti via fitfc code (the blue curve). The transition temperature from hcp to bcc is obtained by comparing the free energies of both structures and locating the temperature where the free energies are equal. Likewise, the free energy of bcc Zr (the red curve) and the calculated free energy of hcp Zr via fitfc code (the blue curve) are demonstrated in figure 3.11, and the transition temperature of hcp to bcc Zr is obtained by locating the temperature where both free energies are equal. As shown in table 3.6, the calculated transition temperature of 1220 K for α-to-β Ti compares well with the experimental values of ref [56] and ref [9] and computational values of ref [45] and ref [24]. Similarly, the transition temperature of α to β for Zr is computed to be $1172K$, and agrees well with the experimental values of ref [9, 21, 89], as shown in table 4.1. The computational values of ref [58] and ref [83], computed using empirical potential MD and tight-binding, are less in agreement with the experimental values.

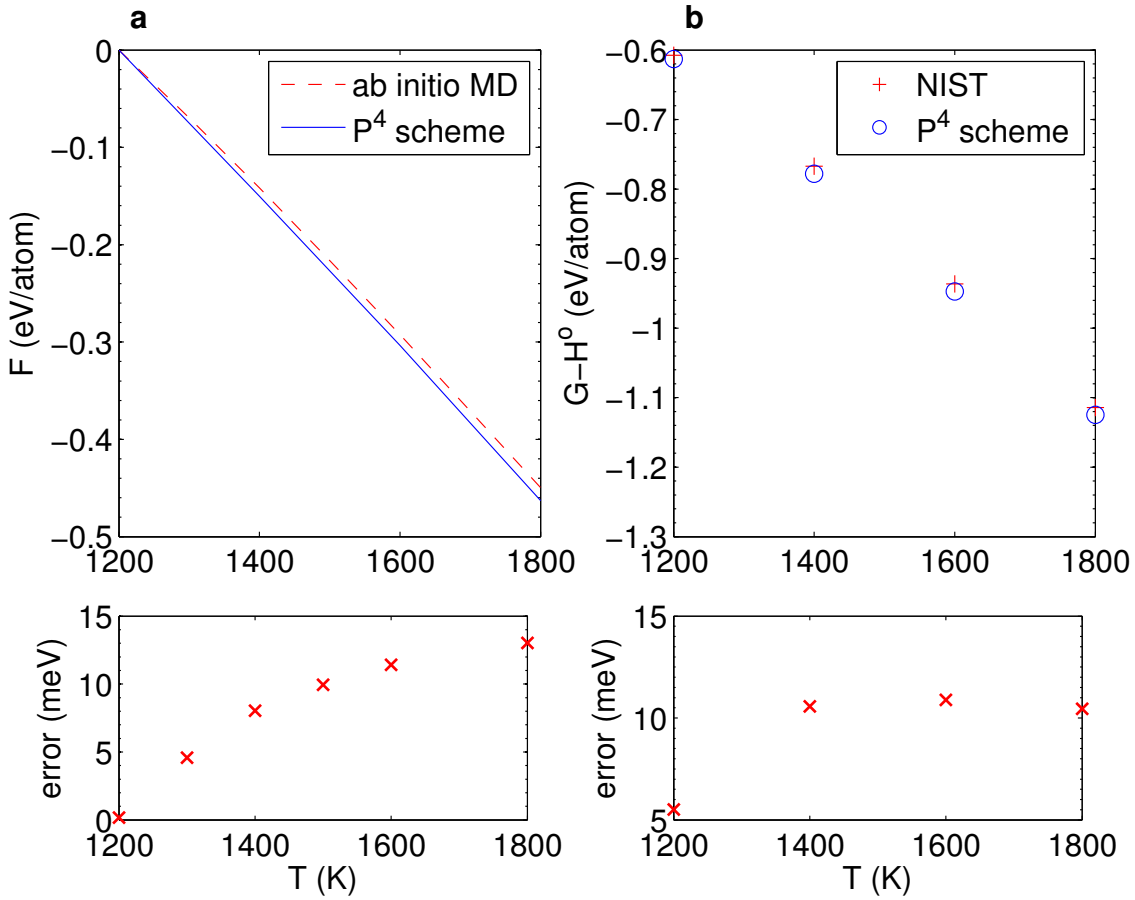

Figure 3.8: a) Helmholtz free energy of bcc Ti b) Gibbs free energy of bcc Ti with reference to hcp Ti enthalpy at room temperature. The error of calculated G with respect to NIST is 5 meV and 10 meV for 1200 K and 1400 – 1800 K, respectively.

3.4 Computational Details

1) All electronic structure calculations are performed using the Vienna Ab initio Simulation Package (VASP) [36–39], implementing the projector augmented wave (PAW) method [40]. For both Ti and Zr, the PBE functional [54] is used, with a plane wave kinetic energy cutoff of $222.3eV$ and $229.8eV$, respectively. A $(4 \times 4 \times 4)$ Monkhorst-Pack mesh [48] is used for creating k-space grid. Volume relaxation for each supercell is performed in two steps (relaxing the initial structure and re-relaxing) using the Methfessel-Paxton method [46] with $ISMEAR = 1$ and $SIGMA = 0.15$.

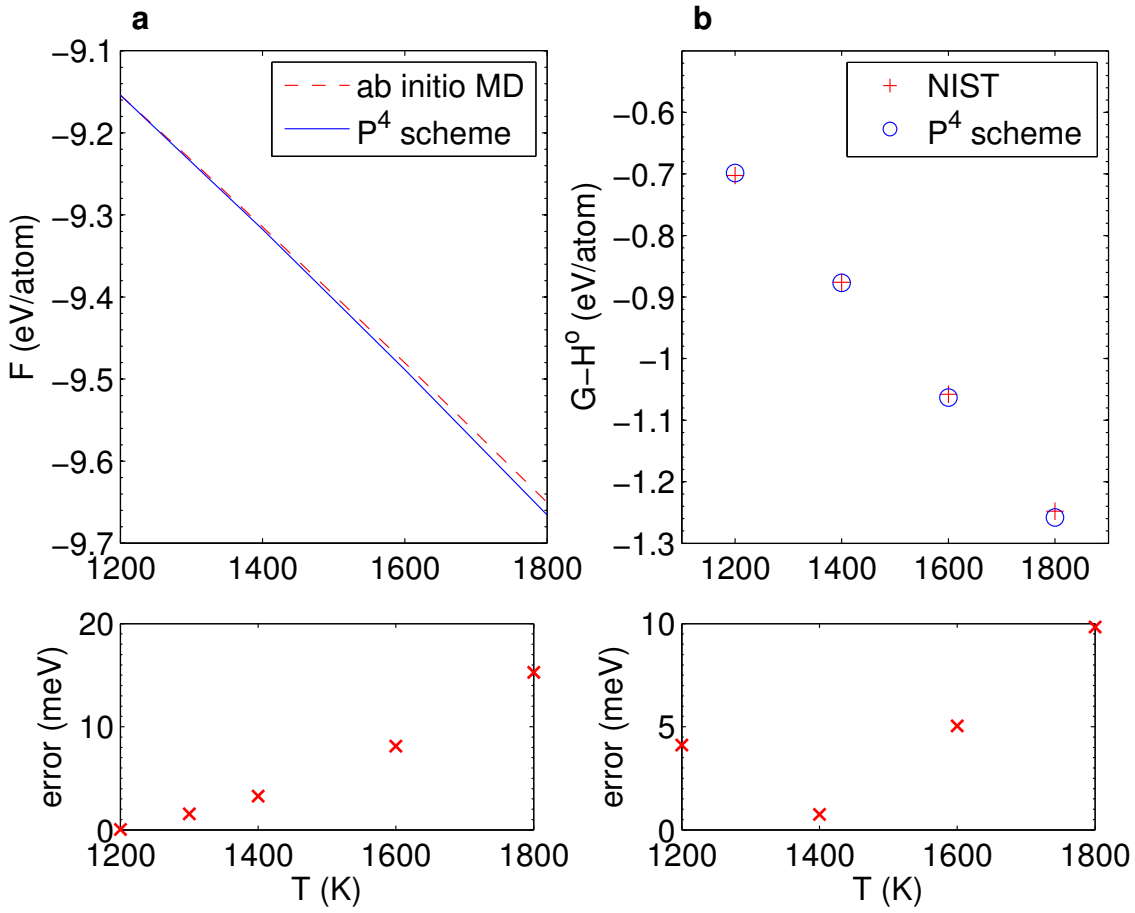

Figure 3.9: a) Helmholtz free energy of bcc Zr b) Gibbs free energy of bcc Zr with reference to hcp Zr enthalpy at room temperature. The error of calculated G with respect to NIST is less than 5 meV and 10 meV for $1200 - 1600$ K and 1800 K, respectively.

To obtain the energy (i.e. the energy of the relaxed volume structure), the tetrahedron method [6] with Blöchl corrections is used. All of the energies, forces and second derivatives of energy (force constant matrix), used in calculations of free energies, are obtained using PAW-PBE with Fermi smearing ($ISMEAR = -1$) with $SIGMA = 1200k_B = 0.1034eV$.

2) In order to obtain the location of the minimum inside ζ_σ for each configuration, $\mathbf{x}_\sigma^u$ is used as an initial guess, and a sequence of position vectors $(\mathbf{x}_\sigma^u, \mathbf{x}_1, \mathbf{x}_2, ..., \mathbf{x}_{n+1})$ is constructed by moving along the negative of the gradient of potential energy hyper-

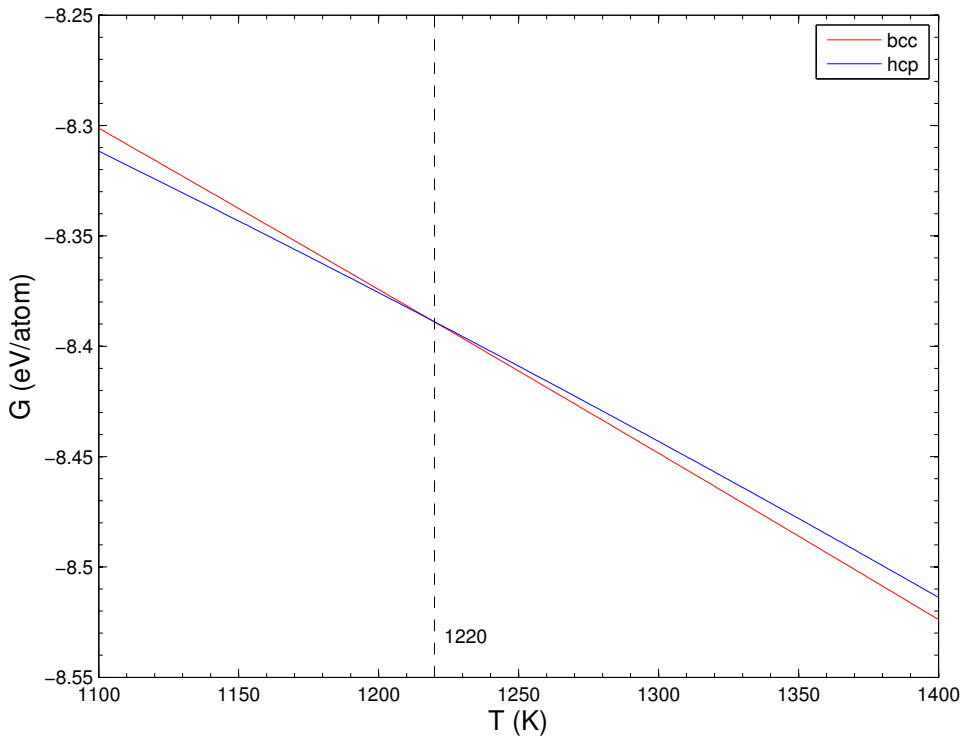

Figure 3.10: The red curve and the blue curve are the second order polynomial fitted to free energy values of bcc and hcp Ti, respectively. The dashed line corresponds to the intersection of free energy curves at $1220K$.

Table 3.6: Transition temperature from hcp(α) to bcc (β) phase for Ti.

this work	ref [56]	ref [9]	ref [45]	ref [24]
$1220K$	$1156.15K$	$1198.26K$	$1114K$	$1250K$

surface using the following equation

$$\mathbf{x}_{n+1} = \mathbf{x}_n - \gamma_n \nabla V(\mathbf{x}_n) \tag{3.16}$$

where γ is an arbitrary small scalar. If γ_n is small enough (it satisfies Wolfe condition [84]), then $V(x_{n+1}) <= V(x_n)$ and at least one minimum is found.

In the steepest-descent method, potential energy, $V(\mathbf{x}_n)$, and the gradient of potential energy, $\nabla V(\mathbf{x}_n)$, are calculated using VASP. For each step, a value of 0.02 $\mathring{A}^2/eV$ is used for γ. If the movement along the negative gradient directs the configuration

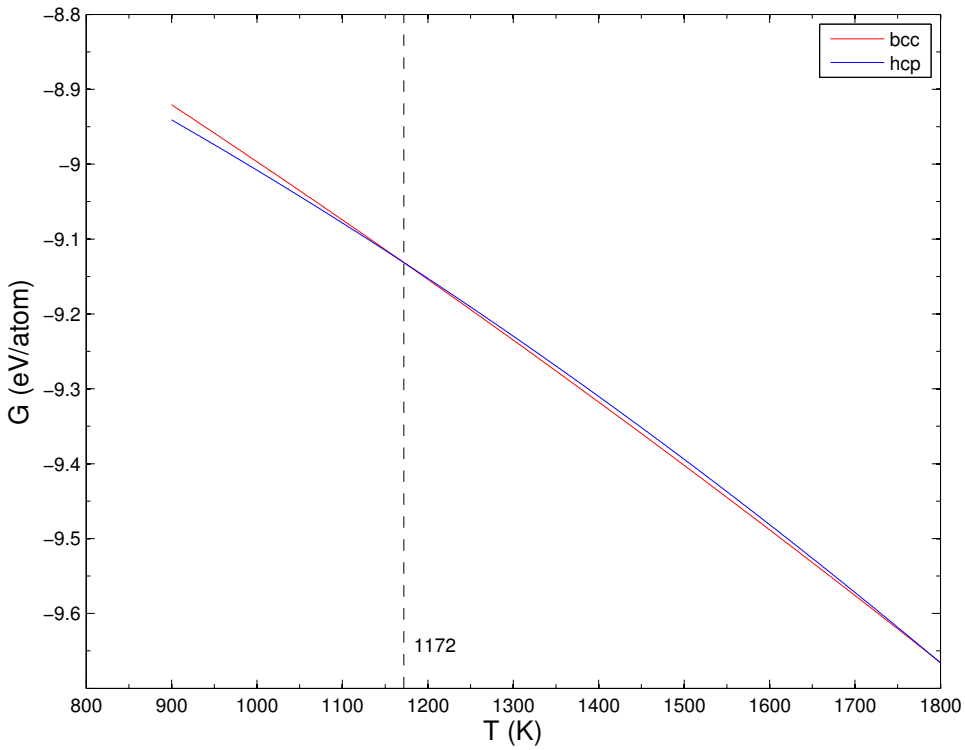

Figure 3.11: The red curve and the blue curve are the second order polynomial fitted to free energy values of bcc and hcp Zr, respectively. The dashed line corresponds to the intersection of free energy curves at $1172K$.

Table 3.7: Transition temperature from hcp(α) to bcc (β) phase for Zr.

this work	ref [21]	ref [89]	ref [9]	ref [58]	ref [83]
$1172K$	$1138.15K$	$1136K$	$1134.1146K$	$1349K$	$1912K$

outside ζ_σ, then the projection of the force vector, $\mathbf{f}_v(\mathbf{x}_n)$, along the boundary of ζ_σ replaces $\nabla V(\mathbf{x}_n)$ in equation (3.16).

3) The training data set for the cluster expansion consists of a number of constrained vibrational free energies, $F^*(\sigma, T)$, calculated by the presented scheme. Constrained vibrational free energy of σ_g is always included within the data set along with the constrained vibrational free energies of some configurations with a definite number of Ti/Zr atoms displaced randomly from $\mathbf{x}_g$. The data set also includes F^*_σ of all symmetrically distinct combinations of 1 and 2 atoms displaced from $\mathbf{x}_g$.

4) Free energies of hcp Ti and hcp Zr are calculated using standard quasi-harmonic approximation, utilizing the fitfc code [72, 75]. For calculating force constant, the fitfc code includes up to the third nearest neighbor forces in a 90 atom supercell with 0.1 Ådisplacements.

Quasi-harmonic calculations, implemented in the fitfc code in order to include thermal expansion in the free energy calculations, are used for a set of different c/a-ratios for hcp Ti/Zr. Hence, free energy, instead of energy, is minimized with respect to c/a-ratio at different temperatures (in this case, the c/a-ratio is considered as a degree of freedom and is allowed to relax during optimization).

5) In ab-initio molecular dynamics calculations, the thermostat is conducted under the Nosé-Hoover chain formalism [28, 44, 49, 50] and ensemble averages are captured every 20 steps ($60fs$) in a MD trajectory of several thousands of steps.

Chapter Four

Alloys: Shape Memory Alloys

4.1 Introduction

Shape-memory alloys (SMAs) are a class of alloys that remember their original shape after being deformed, hence they can return to their pre-deformed shape when heated above a certain temperature. The underlying mechanism of the so-called "shape-memory" effect behavior is the phase transformation between a high-temperature parent phase called austenite and a low-temperature produced phase called martensite. This martensitic transformation is a diffusionless structure phase transformation, involving the collective shift of atoms at the same time to form a new structure. Therefore, no local composition change is included, while a change in the shape of unit cell along with atomic scale displacement of atoms in the lattice is observed.

Aside from shape-memory effect, some shape-memory alloys exhibit another anomalous mechanical property called "pseudo-elasticity". Pseudo-elasticity is the reversible response of a crystal to applied stress, caused by a phase transformation between the austenitic and martensitic phases of the crystal. A pseudo-elastic material returns to its original shape after removal of even large deformations, as it creates a stress-induced phase which becomes unstable after removal of stress. The phase transformation in pseudo-elasticity is induced by mechanical stress, whereas the phase transformation in shape-memory effect is a response to temperature.

Not all alloys that have several structural phases at a specific composition range display a shape-memory effect. The reason is that in order to reveal shape-memory effect, the crystal requires to undergo a full reversible phase transformation between austenite and martensite phases. This type of transformation excludes all phase transformations caused by local migration and diffusion of atoms inside a crystal.

Shape memory alloys, used in industrial applications, are categorized into two main groups: copper-based and nickel-titanium-based alloys. Although, other alloys such as Fe-Pt, Fe-Pd and Au-Cu also exhibit shape memory effect (SME), their cost

and other disadvantageous properties, like high transformation temperature, prevent them to be used in industrial applications. Although copper-based alloys are less expensive, nickel-titanium-based alloys are preferable due to their perfect corrosion resistance and biocompatibility [42].

The specific property of this group of alloys has attracted the attention of different fields, and SMAs have found their way into a wide range of applications. They are not only useful as structural elements, due to their mechanical toughness, but they also have the capability to fulfill the functions of sensors and actuators. SMAs are widely used in different domains, such as biomedical industry, aerospace and the nuclear industry [51].

The martensitic transformation, austenite→martensite, takes place when the free energy of martensite becomes less than the free energy of austenite, below the critical temperature, T_0, where the free energy of two phases are equal. However, the transformation does not start exactly at T_0, but the appearance of the first martensite platelet begins at M_s^0 (martensite start) during cooling, and austenite disappears completely at M_f^0 (martensite finish) as the transformation evolves upon further cooling. The reverse transformation, martensite→austenite, occurs when the SMA is heated from martensite phase, and the disappearance of the first martensite platelet begins at A_s^0 (austenite start), followed by the complete disappearance of martensite at A_f^0 (austenite finish). Figure 4.1 illustrates a schematic representation of austenite fraction as a function of temperature, obtained from reference [42]. The equilibrium temperature, T_0, is in the neighborhood of $(M_s^0 + A_f^0)/2$.

SME reveals itself when an SMA is deformed while in the martensite phase ($T < M_f^0$) and then unloaded while still at the martensitic phase. If the material is subsequently heated above A_f^0, parent austenite phase is obtained, and the inelastic strain is recovered. One has to distinguish between elastic strain, which is recovered after unloading, and inelastic strain, (induced by de-twinning and favored orienting

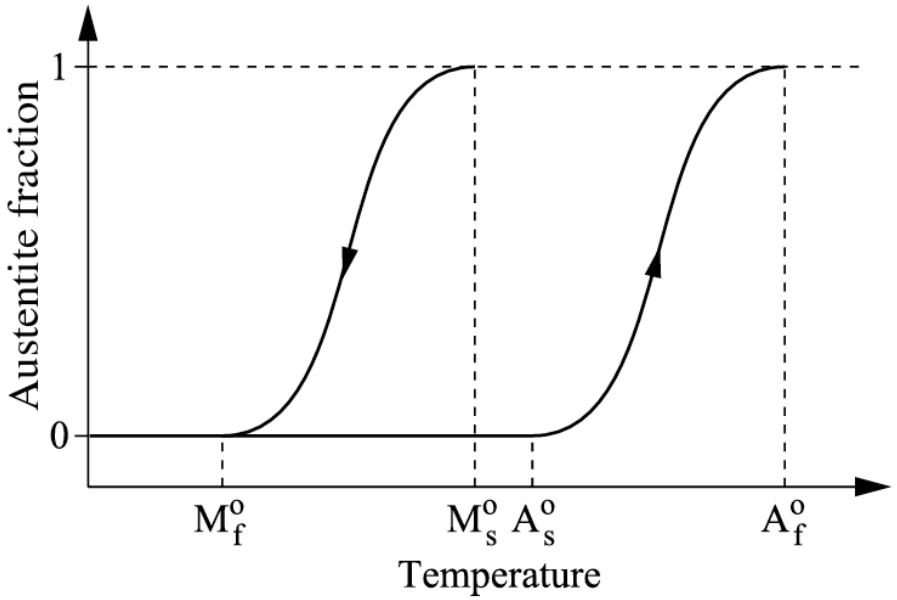

Figure 4.1: Volume fraction of austenite as a function of temperature. Characterization of the four phase transformation temperatures in the stress free state. Reproduced from reference [42]

of multiple martensitic variants), which is only recovered by transforming back to parent austenite phase upon heating. The subsequent cooling of austenite phase results in multiple martensitic variants. The great mobility of the boundaries between multiple variants of martensite and twinning interfaces has the key role in shape memory effect, where the mobility of these interfaces is obtained at stress levels far lower than the plastic yield limit of the martensite.

In pseudo-elasticity, the martensitic transformation is induced by stress while the material is in the austenite phase, at temperatures above A_f^0. In this case, the detwinned martensite phase is produced directly from austenite upon applying stress. Figure 4.2 demonstrates a schematic representation of stress-strain-temperature ternary diagram for SMAs, indicating SME and pseudo-elasticity, obtained from reference [42].

Almost all practical shape memory alloys, like NiTi and Cu-based alloys, have a transformation temperature lying in the range of $-100°C$ to $100°C$ [62]. A wide range of applications of SMAs at high temperatures, like combustion engines, gas

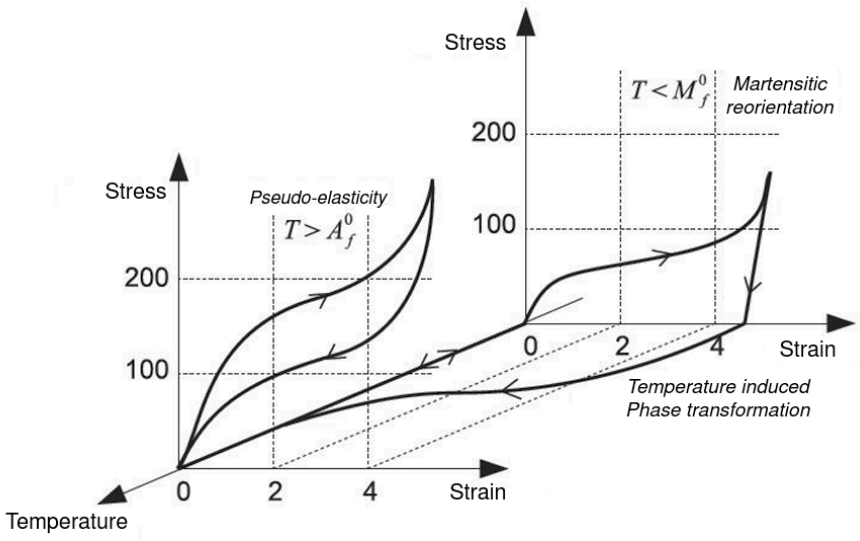

Figure 4.2: Shape-memory effect and pseudo-elasticity in an SMA. Reproduced from reference [42]

turbines, rocket engines, nuclear reactor environments, and control of high temperature chemical reactions can be envisioned. However, a limited number of alloys have the potential to be used as high-temperature shape memory alloys, such as NiAl [17], AuTi, PdTi, PtTi [5, 15], and RuX (X=Ta, Nb) [19]. Among these compounds, the transformation temperature of PdTi and AuTi is in the range of $400°C$ to $600°C$, depending on stoichiometry [15], while PtTi has a second order martensitic transformation at higher temperature (around $1000°C$ [15]).

It has been shown in the previous studies [4, 87] that ordered PtTi exhibits shape-memory effect and pseudo-elasticity above $1273K$, thus making it a promising potential candidate as the basis for a high-temperature SMA. Acceptable shape recovery is observed both in martensitic phase below M_s (pseudo-elasticity), caused by reversible twin interface movement in the martensite, and upon heating to parent phase (SME) [4, 87].

It has been reported that PtTi undergoes a martensitic transformation at about $1300K$ from a high-temperature austenite phase with a cubic $B2$ structure (CsCl structure with space group $Pm3\bar{m}$) to a low-temperature martensite phase with

orthorhombic $B19$ (space group $Pmma$) structure [4, 15]. This $B2 \rightarrow B19$ transformation also occurs in PdTi and AuTi. For NiTi, the austenite phase appears as a cubic $B2$ structure on average, although x-ray diffraction studies predict an austenite phase that cannot be described by $B2$ symmetry [79, 91]. At lower temperatures, NiTi transforms to a monoclinic $B19'$ structure (space group $P2_1/m$, reported experimentally [41]). The $B19$ structure in PdTi and PtTi has a very close structure to hcp, such that it can be regarded as chemically ordered hcp. Such analogy shed light on the mechanism for martensitic transformation ($B2 \rightarrow B19$), which ca be viewed as analogous transformation of $bcc \rightarrow hcp$ [30]. Figure 4.3 illustrates the unit cell for $B2$ and $B19$ structures.

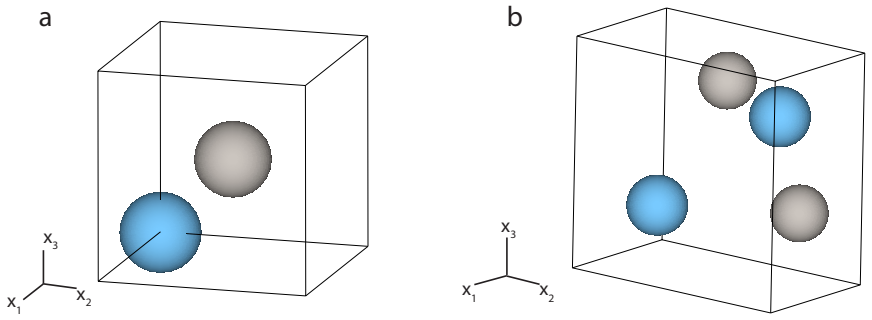

Figure 4.3: a)Primitive unit cell of $B2$ PtTi. b)Primitive unit cell of $B19$ PtTi. Grey (smaller) and blue(larger) spheres indicate Ti and Pt atoms.

A number of studies have been conducted so far, in order to investigate the $B2 \rightarrow B19$ martensitic transformation in PtTi [15], and to elaborate the phase diagram of Pt-Ti system around equiatomic composition via a detailed exploration of its microstructure [4, 5, 59]. The electronic structure and energetics of PtTi at different phases ($B2$,$B19$,$B19'$) have also been investigated [30, 80, 88]. However, to our best knowledge, there has been no elaborate investigation of the thermodynamic properties of the austenite phase of PtTi, except for the Calphad model introduced based on the available experimental data on transformation temperatures for phase dia-

gram calculations [43].

Some SMAs, including PtTi and PdTi, exhibit soft modes or instabilities in the phonon dispersion of austenite. The soft-mode theory of structural transitions [10], which associates instabilities or near-instabilities in certain diatomic crystals to ferroelectric phase transitions, has been used in recent studies to investigate mechanisms underlying the martensitic transformation in PtTi and PdTi [30]. Therefore, it is essential to investigate the phonon dispersion curve of austenite phase.

Figure 4.4, indicates the phonon dispersion curve of $B2$ structure of PtTi, calculated utilizing fitfc module in the Alloy-Theoretic Automated toolkit (ATAT) [72]. There are large regions of reciprocal space where one, two or even three modes are unstable. The major instabilities occur for the acoustic mode at M and along $\Gamma - R$ branch.

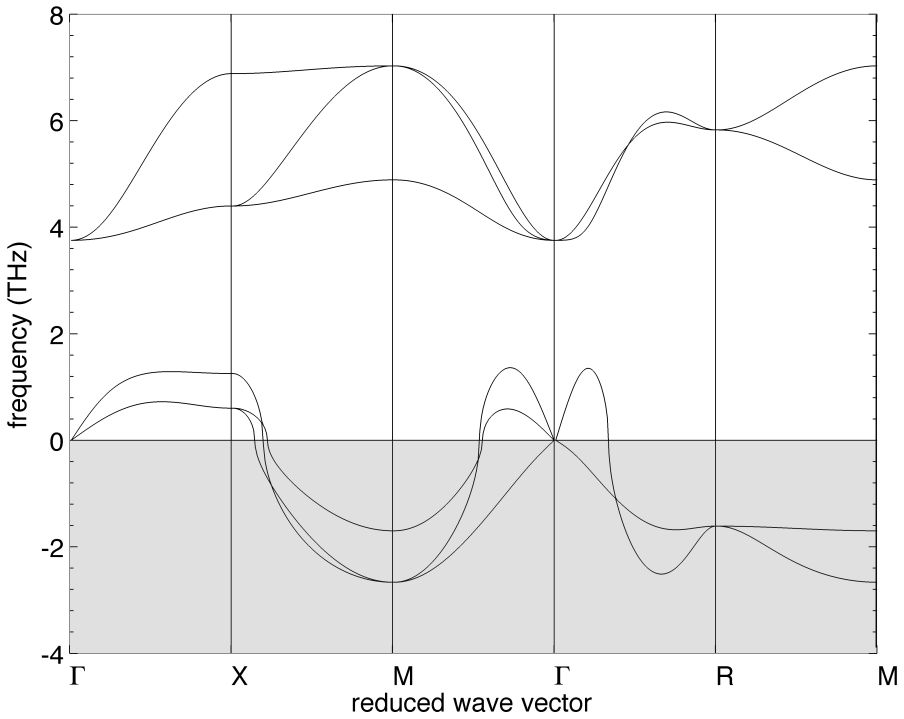

Figure 4.4: Phonon dispersion curve of $B2$ PtTi calculated at equilibrium lattice parameter $3.172\mathring{A}$ and $0K$. The imaginary frequencies of the unstable modes are plotted as negative values.

4.2 Free energy calculation of B2 phase of PtTi

Despite mechanical instabilities inherent to the $B2$ phase of PtTi, it is dynamically stabilized by anharmonic effects and can be characterized by large fluctuating local distortions. The unstable phonons at M and along $\Gamma - R$ could be considered as equivalents to those of unstable bcc phases, such as bcc Ti and bcc Zr, which corresponds to the martensitic transformation from bcc to hcp and ω phases, respectively. This similarity illuminates the underlying microscopic mechanism for $B2 \rightarrow B19$ martensitic transformation. The atomic displacement associated with the unstable phonons at M and along $\Gamma - R$ are obtained similar to those for bcc Ti and bcc Zr (see equation (3.6)). The M unstable mode results in shuffling of $(110)_{B2}$ planes along $[1\bar{1}0]$ direction, similar to the mechanism for $bcc \rightarrow hcp$ transformation (for a detailed description see reference [30]). This analogy motivates us to look into the mechanism corresponding to the phonon mode located at $\Gamma - R$ branch close to $\xi = 2/3$. This phonon mode transforms $B2$ structure to $C32$ (analogous ordered phase of ω). This transformation is resulted by the movement of the (111) planes in such a way that two neighboring planes get close to each other while every third plane stays at rest. By distorting $B2$ structure along this path, relaxing the volume of each distorted structure, and calculating the energy of each distorted structure a local minimum is found adjacent to $B2$ structure. As depicted in figure 4.5, the minimum structure lies about $15meV$ lower than the ideal $B2$ structure ($d = 0$).
The augmented lattice is constructed by combining $B2$ lattice points with the lattice sites located at the nearby local minimum. Implementing the symmetry point group of high-symmetry structure (in this case, O_h^1 for $B2$) results in an augmented lattice with eight corner lattice sites surrounding each $B2$ site. This augmented lattice is very similar to that obtained for bcc Ti and bcc Zr. For a schematic representation, see figure 2.9.

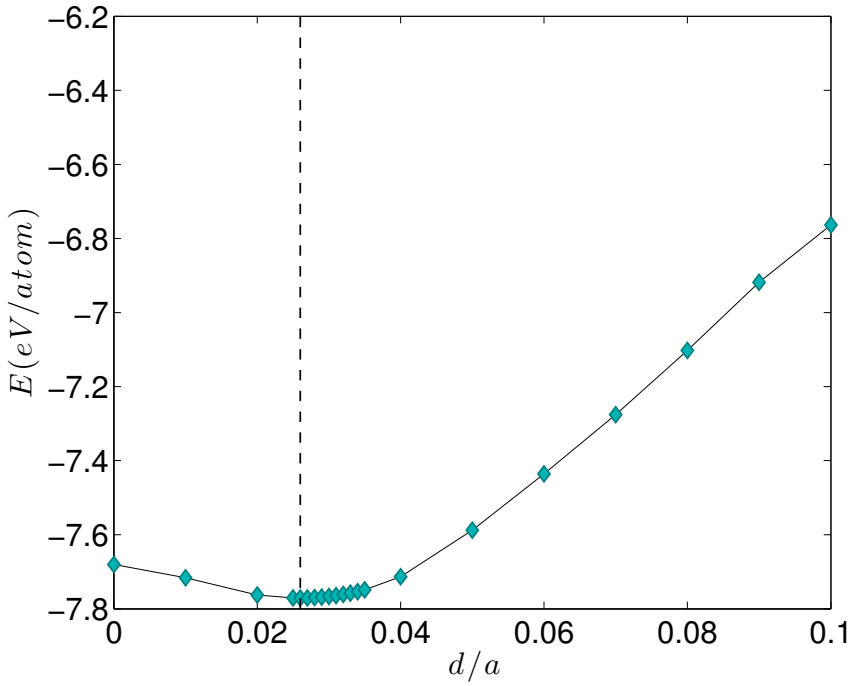

Figure 4.5: Energy per atom versus displacement (d) along $\mathbf{L}\frac{2}{3}(1,1,1)$ phonon of $B2$ PtTi with lattice constant a. There exists a minimum located at $d/a = 0.026$.

Only the unstable $\mathbf{L}\frac{2}{3}(1,1,1)$ phonon mode results in a adjacent local minimum which is a small deviation from $B2$ structure. This nearby local minimum becomes useful in the augmented lattice construction. Distorting the $B2$ structure along other unstable phonon modes, such as the phonon mode at M, does not result in an adjacent local minimum, in spite of the fact that the M unstable mode is associated with the martensitic transformation $B2 \rightarrow B19$. Figure 4.6 illustrates the energy change for the distortion of $B2$ structure along M phonon mode (shuffling of $(110)_{B2}$ planes along $[1\bar{1}0]$ direction), which clearly results in no nearby local minimum. In order to retain the symmetry of the high-symmetry structure ($B2$), the cell shape is not allowed to change for each distortion. The only degree of freedom equilibrated is the volume of the cell. If one relaxes the cell shape, which alters the symmetry of the structure, a minimum along this path is found (see figure 4.7). However, this minimum is not suitable for constructing the augmented lattice, because those struc-

tures that are being combined to build the augmented lattice must have unit cells with the same symmetry. The unit cell of the local minimum structure found along $\mathbf{L}\frac{2}{3}(1,1,1)$ phonon distortion contains the symmetry of $B2$ structure.

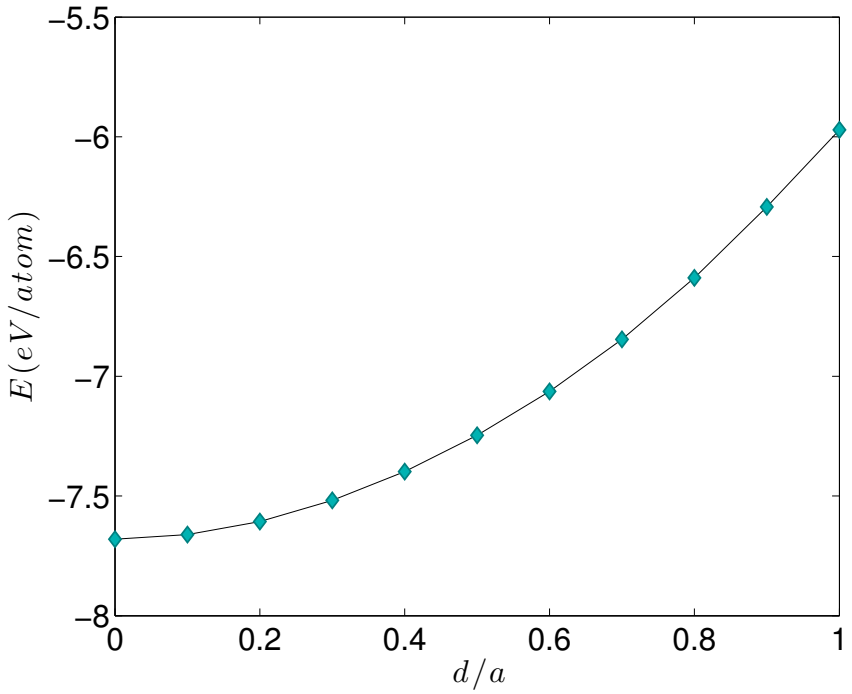

Figure 4.6: Energy per atom for distortion (d) along M phonon of $B2$ PtTi with lattice constant a. a is the equilibrated lattice constant for each distortion. d is the distortion amplitude along the M phonon eigenvector. There exists no local minimum along this path.

When the augmented lattice is constructed, the constrained vibrational free energy, F^*_σ, is calculated for a number of different configurations, using equations (2.17) to (2.28). There is a minor modification in calculation of the partition function for a diatomic system (compared to monatomic systems of bcc Ti and bcc Zr discussed in chapter 3) and equation (2.17) is modified accordingly.

$$Q = \frac{1}{h^{3N}} \int_{-\infty}^{\infty} e^{-\beta \frac{\mathbf{p}^2}{2m_i}} d\mathbf{p} \int_{\mathbf{x}\in\zeta_\sigma} e^{-\beta V(\mathbf{x})} d\mathbf{x} \tag{4.1}$$

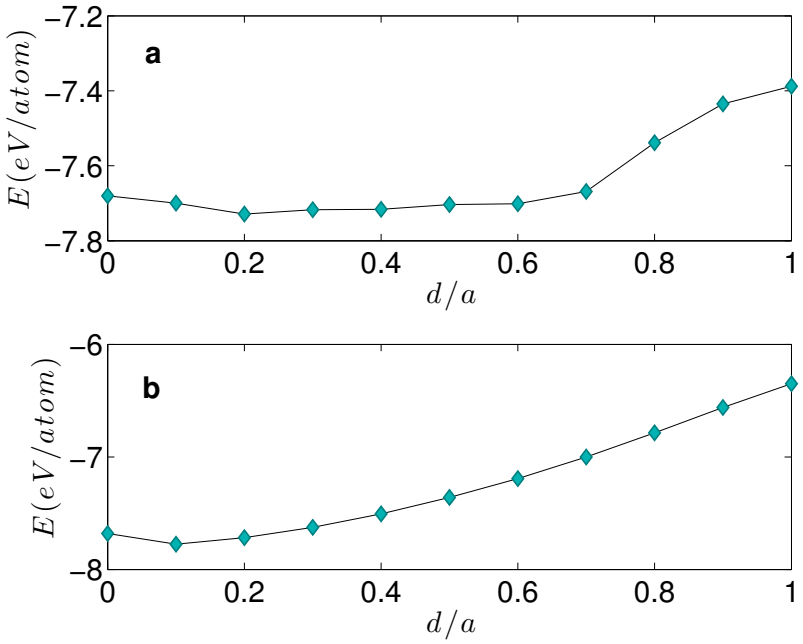

Figure 4.7: a)Potential energy per atom for distortion (d) along M phonon of $B2$ PtTi with lattice constant a. For each distortion, unit cell volume and shape is allowed to equilibrate, as well as position of atoms. d is the distortion amplitude along the M phonon eigenvector. b) Potential energy per atom for distortion (d) along M phonon of $B2$ PtTi with lattice constant a. For each distortion unit cell volume and shape is allowed to equilibrate but the atomic coordinates are fixed.

In the above equation m_i is the mass of atom i (i=Pt or Ti). For the ordered $B2$ structure with $50at.\%$ Pt, equation (4.1) is simplified as the following.

$$Q = (\frac{2\pi\sqrt{m_{Ti}m_{Pt}}k_BT}{h^2})^{\frac{3N}{2}} \times Z_\sigma \tag{4.2}$$

Subsequently, the constrained vibrational free energy for a configuration is calculated according to equation (3.10) with the above modification.

The calculated vibrational free energies for a set of configurations are used as a data set, in order to obtain a relation for F^*_σ as a function of σ. Figure 4.8 illustrates the calculated constrained vibrational free energies for a number of different configurations at $1400K$. The fit to this data set is only valid for free energy calculation at $1400K$. The performance of the fit is assessed by cross-validation score, defined in

equation (2.30), and is shown in figure 4.8. The constrained vibrational free energy

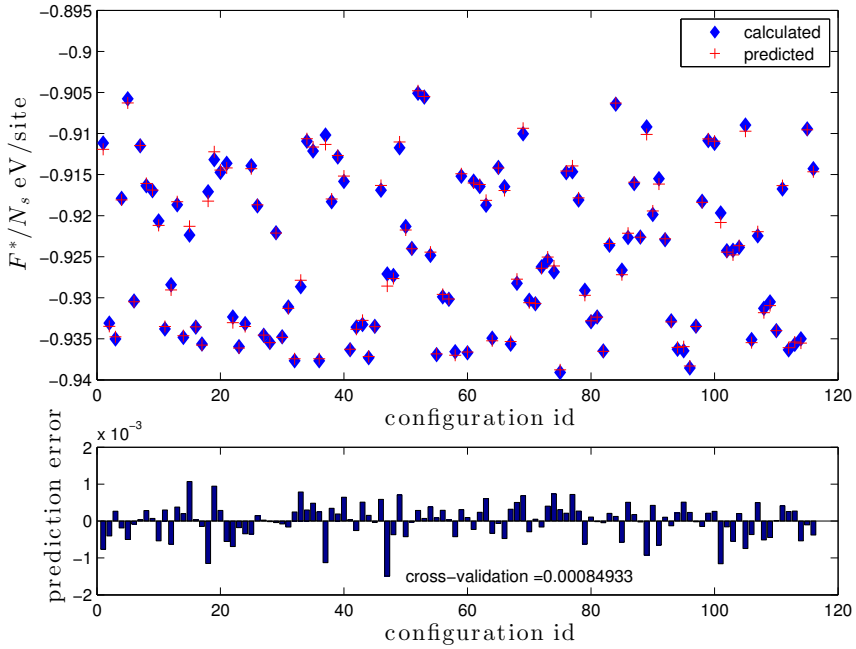

Figure 4.8: The calculated constrained vibrational free energies at $1400K$, depicted as blue diamonds, and the constrained vibrational free energies predicted by the fit, illustrated as red crosses. The prediction error corresponding to each configuration is indicated as a bar graph. The CV score for the fit is 0.00085

for each configuration is calculated for other temperatures according to equation (2.31), where F^*_σ at $1400K$ is used as the initial point in the integration. Figure 4.9 shows the calculated F^*_σ at $1400K$, $1600K$, $1800K$, and $2000K$, sorted for the purpose of better representation. In equation (2.31), the average internal energy for each configuration, $\langle U_\sigma \rangle$, is calculated by conducting a Monte Carlo simulation confined in ζ_σ.

The clusters considered in the cluster expansion (see equation (2.29)) are empty and point clusters, along with all pairs up to the longest pair between nearest neighboring *groups* of sites. In $B2$ PtTi, there exists two different types of *group*. One is the *group* of sites that can be occupied by a Ti atom and eight vacancies, and second is the *group* of sites that can be occupied by a Pt atom and eight vacancies. These *groups* of sites are considered in an ordered way, so that *group* one (Ti *group*) is

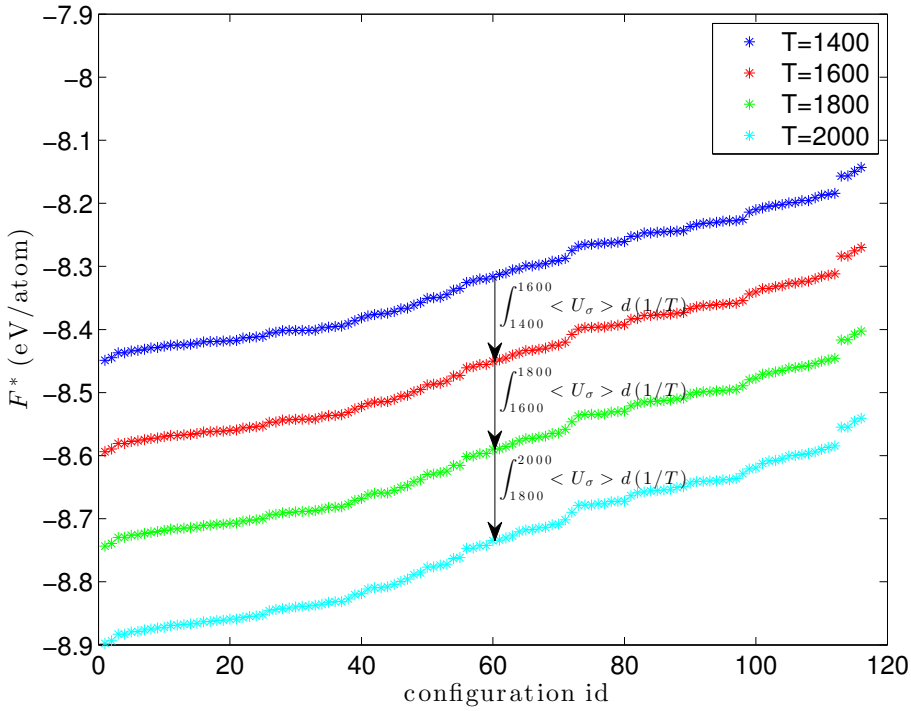

Figure 4.9: The calculated constrained vibrational free energies at $1400K$, $1600K$, $1800K$, and $2000K$ for a number of different configurations. The free energies are sorted for the purpose of better representation. A Monte Carlo simulation is carried out in order to calculate the average internal energy associated with each configuration,U_σ, at different temperatures.

surrounded only by *group* two (*group* Pt). Since there exists two distinct atomic type, the Ti-Ti, Pt-Pt and Pt-Ti pairs are distinguishable. Therefore, the number of short-pairs is twice the number of short-pairs in the case of bcc Ti and bcc Zr, and the number of long-pairs increases, so that Vac-Ti, Vac-Pt and Pt-Ti pairs are recognized. A temperature-dependent ECI ($J(T)$ in equation (2.29)) is obtained for each of these clusters through a fitting procedure, where T is the temperature for which F^* values are calculated.

The canonical ensemble average constrained vibrational free energy $\langle F^* \rangle$ is obtained by conducting a Monte Carlo simulation over a temperature range, starting from the temperature of interest T, (which coincides with the temperature for which the cluster expansion is valid), to the high temperature limit. The Monte Carlo simulations are carried out utilizing MultiComponent Easy Monte Carlo Code (memc2) [72],

and using the cluster expansion fitted for T in equation (2.29). Figure 4.10 indicates the average constrained vibrational free energy $\langle F^* \rangle$ for four different fits associated with $1400K$, $1600K$, $1800K$ and $2000K$. The average free energy is calculated from the high temperature limit (in this case $1.5 \times 10^5 K$) to the temperature of interest, T (T =$1400K$, $1600K$, $1800K$ and $2000K$). Each fit approaches a limit at high enough temperatures, which replicates the mean-field approximation limit calculated in the following (see table 4.1). Subsequently, the total free energy of $B2$ PtTi at temperature T is calculated according to equation (2.35), where $F(T_0)$ is the high temperature limit (MFA) free energy.

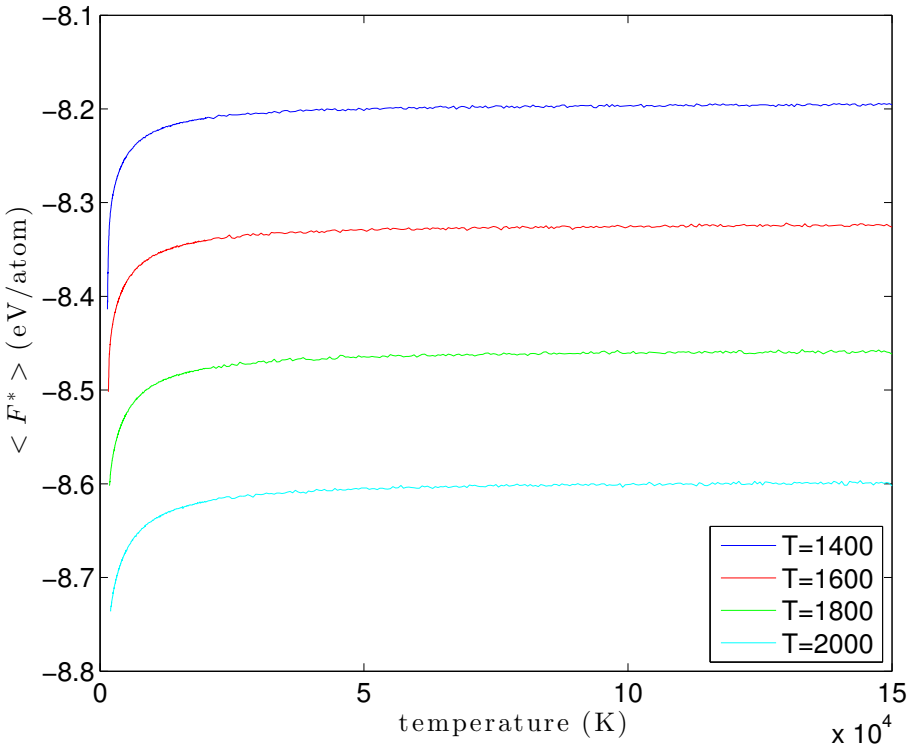

Figure 4.10: Average vibrational free energy vs. temperature. The temperature is varied from high temperature limit ($1.5 \times 10^5 K$) down to the temperature of interest for each fit (T = 1400, 1600, 1800 and $2000K$). All the fits approach a limit at high temperature limit which replicates the analytic MFA limit.

At high enough temperatures, each site on *group* one is equally likely to be occupied by a Ti atom (this is a constrained random situation, where each *group* of sites is occupied by only one Ti atom and differs from a complete random case where all the

sites can be equally likely occupied by Ti or vacancies). Likewise, each site on *group* two is equally probable to be held by a Pt atom. Therefore, the average correlation of each site in equation (2.29) can be calculated analytically. Considering that each fit is identified by its set of $J(T)$, the high temperature limit for vibrational free energy ($F^*_{\texttt{mfa}}$) is obtained by substituting the average correlations in equation (2.29). The average correlation associated with each cluster is calculated as the following, if an occupation value of +1 and -1 is assigned to Ti/Pt and vacancies, respectively.

empty	$= 1$
center point	$= 8/9 \times -1 + 1/9 \times 1 = -7/9$
corner point	$= 8/9 \times -1 + 1/9 \times 1 = -7/9$
half-diag pair	$= 8/9 \times (-7/8 + 1/8) + 1/9 \times (-8/8) = 5/9$
edge pair	$= 8/9 \times (-3/12 + 9/12) + 1/9 \times (12/12) = 5/9$
face-diag pair	$= 8/9 \times (-3/12 + 9/12) + 1/9 \times (12/12) = 5/9$
diag pair	$= 8/9 \times (-1/4 + 3/4) + 1/9 \times (4/4) = 5/9$
long pairs	$= 1/81 \times 1 + 64/81 \times 1 + 2 \times 8/81 \times -1 = 49/81$

Table 4.1 demonstrates the high temperature vibrational free energy obtained for the fits of $1400K$, $1600K$, $1800K$, $2000K$.

To determine the total free energy at high temperature limit ($F_{\texttt{mfa}}$), the entropy of the system has to be calculated. Analytical value for entropy per atom is obtained considering that for each Ti or Pt atom the number of possible states equals the number of ways of picking a site from a *group* of sites (which in this case equals nine). Consequently, the entropy is obtained as the following.

$$s = k_B \ln(w) = k_B \ln(9) \tag{4.3}$$

where w is the number of possible states per atom, and s is the entropy per atom. In figure 4.11, the configurational entropy per atom, obtained from Monte Carlo

simulation, for the $1400K$ fit is illustrated. This entropy value only incorporates the configurational contribution to the total entropy but not the vibrational contribution. At and above temperatures close to 10^4K, s approaches an upper limit (depicted as a horizontal line) which is the maximum possible configurational entropy for the system. This value reproduces the analytical entropy value calculated in equation (4.3).

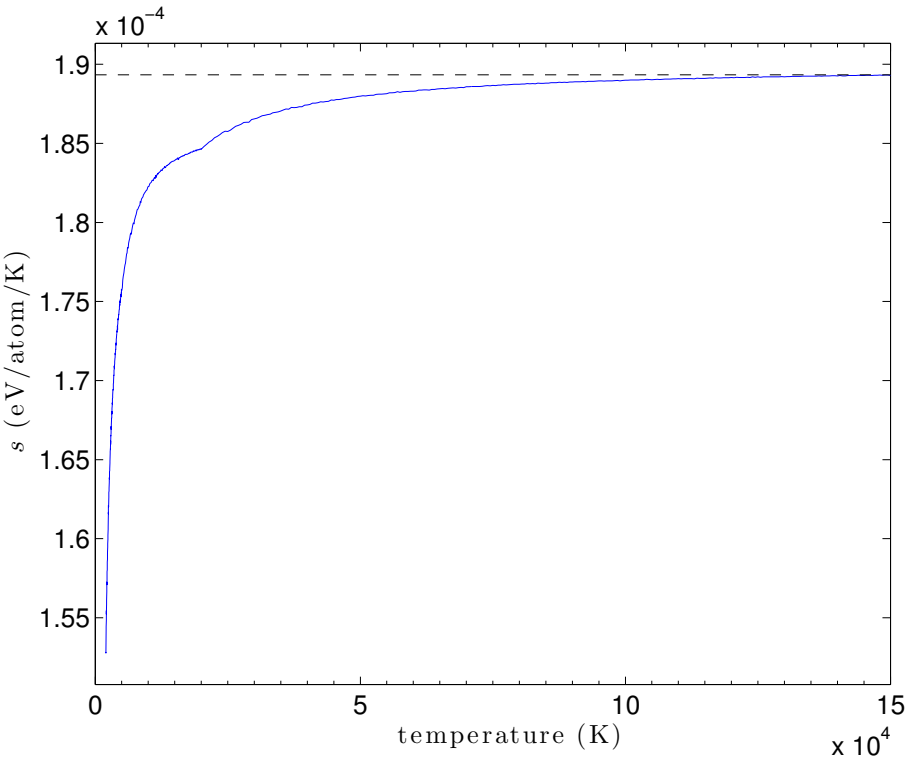

Figure 4.11: Configurational entropy per atom vs. temperature. The temperature is varied from high temperature limit (1.5×10^5K) down to the temperature of interest during a Monte Carlo simulation for the fit at $T = 1400K$. The entropy approaches a limit at high temperature which is the highest possible entropy for the system. Entropy values are only physical at temperatures close to $1400K$.

Free energy per atom at MFA limit is calculated accordingly.

$$F_{\texttt{mfa}}(T) = F^*_{\texttt{mfa}} - Ts \tag{4.4}$$

The above equation is valid for $T > T_{mfa}$, where T_{mfa} is the mean field approximation temperature. T_{mfa} is obtained by conducting a set of Monte Carlo simulations on the system and obtaining the temperature where the upper limit in $\langle F^* \rangle$ is achieved. This upper limit is readily observed in figure 4.10. The obtained values for $F^*_{\texttt{mfa}}$ and $F_{\texttt{mfa}}$ for $B2$ PtTi at different temperatures are presented in table 4.1. The

Table 4.1: The MFA vibrational free energy and free energy value obtained at high temperature ($1.5 \times 10^5 K$) for $B2$ PtTi.

	fit $1400K$	fit $1600K$	fit $1800K$	fit $2000K$
$F^*_{\texttt{mfa}}$(eV/atom)	-8.1937	-8.3221	-8.4566	-8.5963
$F_{\texttt{mfa}}$(eV/atom)	-36.5950	-36.7234	-36.8577	-36.9972

free energy of $B2$ PtTi is calculated using $F_{\texttt{mfa}}$ as the initial point of integration in equation (2.35). A Monte Carlo simulation is employed where $\langle F^* \rangle$ is integrated from high temperature to the desired temperature. The values obtained for free energy of $B2$ PtTi at different temperatures are listed in table 4.2.

Table 4.2: Helmholtz free energy per unit cell for $B2$ PtTi with reference to the enthalpy of $B19$ PtTi at room temperature (RT), obtained using the presented scheme. $F(T)$ is the polynomial fit for $B2$ PtTi Helmholtz free energy, valid for $1100 < T < 2000$. H^o_{RT} is the enthalpy at RT for $B19$ PtTi.

T(K)	1400	1600	1800	2000
$F - H^o_{RT}$(eV/unit cell)	-1.6530	-1.9877	-2.3473	-2.7263
$F(T)$(eV/atom)$=-8.9521 \times 10^{-4}T - 7.3166$				
$H^o_{RT} = -7.7475$(eV/atom)				

The free energy of $B19$ PtTi, which is the low-temperature or martensite phase, is calculated employing a quasi-harmonic model. In previous studies, it has been shown that $B19$ phase undergoes a low-temperature phase transition to monoclinic $B19'$ (space group $P2_1/m$) [30]. Table 4.3 presents the Γ-point frequencies for $B19$, and only one of the calculated frequencies is imaginary (negative). This unstable mode results in the transformation of $B19$ structure to the lower-symmetry $B19'$ structure.

Although $B19'$ has a slightly lower energy than $B19$ phase, their free energies are almost equal. Therefore, we utilize fitfc module [72] in order to calculate the free energy of $B19$ PtTi at various temperatures by freezing the variables along the unstable mode. This freezing of atoms along unstable mode has negligible effect on the free energy calculation as the number of degrees of freedom grows with increasing the number of atoms (i.e. in the thermodynamic limit).

Table 4.3: Phonon frequencies at Γ for PtTi in $B19$ and $B19'$ structures. Frequencies are obtained from finite differences using VASP. The unstable mode (negative value) in $B19$ couples to the transition in $B19$-$B19'$.

structure	ω (cm^-1)
$B19$	284.1683 284.1683 282.8470 281.8175 281.8175 281.3109 276.4939 272.4972 272.4972 256.6138 256.2377 256.2377 248.3562 244.4553 240.7660 237.3197 229.4473 228.6367 225.3638 225.3125 225.3125 220.6226 219.6862 219.6862 201.3378 196.1216 191.5672 188.3114 188.3114 188.1899 188.1899 186.0535 186.0535 184.2255 179.3557 178.0522 175.9655 174.7340 170.1414 169.5944 163.1166 161.0187 157.5915 152.8057 152.8057 141.2524 141.2524 133.7139 133.7139 127.9863 127.9863 124.3892 118.4036 117.3942 117.1932 117.1932 116.8039 116.6895 116.6895 114.2432 111.0382 111.0382 110.2357 110.2357 109.3285 104.9225 103.2592 103.2592 103.1545 101.0305 101.0127 98.3956 94.3803 90.9917 85.2426 85.2426 82.6649 82.4256 81.6842 81.6842 79.5672 79.5672 78.9368 76.3410 76.3410 74.9369 73.3214 73.3214 68.6460 68.6460 65.6940 59.1559 0.8790 1.1798 1.1888 -45.3776
$B19'$	297.7656 292.1504 292.1504 291.0685 290.6287 288.8445 284.0523 284.0523 280.8143 280.8143 260.5290 260.5290 256.2603 249.9313 244.4756 241.3421 240.5750 236.8354 236.8354 235.1548 232.6105 225.7057 225.7057 220.1973 206.5143 202.5741 196.8180 196.8180 196.1368 192.5224 192.3161 192.1718 192.1718 190.2076 188.6105 188.6105 184.2212 180.8545 172.0954 170.7199 166.1222 160.8190 157.4205 157.4205 155.6270 152.9274 152.9274 152.6173 152.6173 147.0288 147.0288 146.0600 140.2204 136.4321 136.4321 126.5744 124.5255 124.5255 123.0729 122.1501 122.1501 122.1052 120.5299 116.3710 113.1446 112.9191 112.9191 109.5232 108.3682 108.3682 105.1456 101.9432 98.1093 97.5087 92.8675 89.2528 89.2528 89.0858 88.8919 88.8919 83.7231 82.9975 82.9975 78.6936 76.8703 76.4372 76.4372 75.3399 75.3399 67.7035 67.7035 64.6010 41.4412 0.8404 0.9513 1.3725

One can infer that $B19$ structure is dynamically stabilized as is $B2$ structure at higher temperatures. However, since the mechanical instability for $B19$ is just along

one mode, standard quasi-harmonic model is used to calculate its free energy. Atomic motion is frozen along the unstable mode, where the contribution of a single mode to the free energy is negligible in the thermodynamic limit ($N \to \infty$). The Helmholtz free energy of $B19$ PtTi at different temperatures is presented in table 4.4.

Table 4.4: Helmholtz free energy per unit cell of PtTi in $B19$ and $B19'$ structures. Free energies are calculated using quasi-harmonic model utilizing fitfc.

	T(K)						
structure	0	100	200	300	400	500	600
$B19$	-15.5951	-15.6056	-15.6493	-15.7171	-15.8020	-15.9000	-16.0087
$B19'$	-15.5994	-15.6091	-15.6506	-15.7161	-15.7986	-15.8941	-16.0003
	T(K)						
structure	700	800	900	1000	1100	1200	1300
$B19$	-16.1264	-16.2520	-16.3844	-16.5230	-16.6672	-16.8166	-16.9707
$B19'$	-16.1154	-16.2384	-16.3681	-16.5040	-16.6455	-16.7921	-16.9434
	T(K)						
structure	1400	1500	1600	1700	1800	1900	2000
$B19$	-17.1293	-17.2921	-17.4587	-17.6291	-17.8029	-17.9801	-18.1604
$B19'$	-17.0991	-17.2589	-17.4226	-17.5899	-17.7606	-17.9347	-18.1119

Figure 4.12 shows the calculated free energies of $B2$ (the red curve) and $B19$ (the blue curve) PtTi, respectively. The transition temperature from $B19$ to $B2$ is obtained by comparing the free energies of both structures and locating the temperature where the free energies are equal.

4.3 Validation

A large number of previous studies on PtTi have been devoted to investigate additional details about martensitic transformation and martensite and austenite microstructures, specifically mechanical properties associated with shape memory effect, while fewer number of studies explore thermodynamic properties. To our best knowledge, thermodynamical data available on PtTi are experimental phase trans-

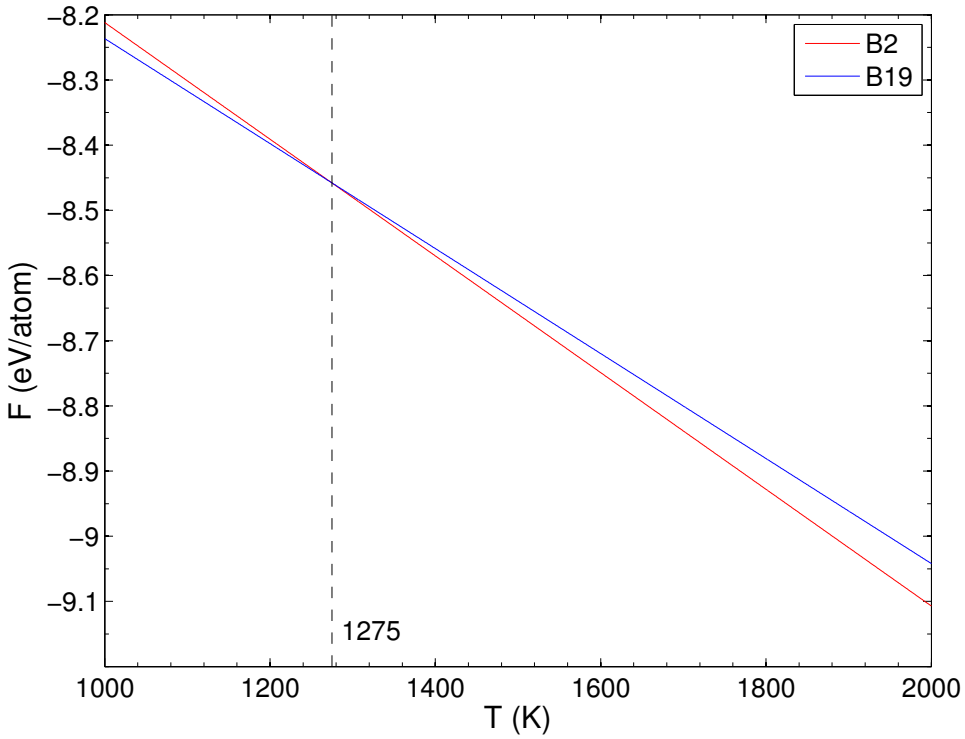

Figure 4.12: The red curve and the blue curve are the first order polynomial fitted to free energy values of $B2$ and $B19$ PtTi, respectively. The dashed line corresponds to the intersection of free energy curves at $1275K$.

formation temperatures, which are utilized to determine the phase diagram of Pt-Ti system around 50 at.% Pt.

Donkersloot and Vucht initially reported to observe shape memory effect at high temperatures in PtTi, thus introduced it as a potential candidate for high temperature shape memory alloy. They reported the characteristic martensitic-transformation temperatures, M_s, M_f, A_s and A_f to be $1070°C$, $1020°C$, $1040°C$ and $1085°C$, respectively [15]. Here, the M_s is higher than A_s which is not possible for a two-phase martensitic transformation cycle. Later, Biggs et al. reported A_s and M_s to be $1040°C$ and $1020°C$, with M_s being about $40°C$ lower than previously accepted [4]. Another study by Yamabe-Mitarai et al. measured M_s, M_f, A_s and A_f as $1262K$, $1236K$, $1273K$ and $1330K$ [86].

Table 4.5 compares the transformation temperature calculated in this thesis to the

Table 4.5: Martensitic transformation characteristic temperatures for PtTi.

	(K)				
	M_s	M_f	A_s	A_f	$T_0 = (M_s + A_f)/2$
ref [15]	1343.15	1293.15	1313.15	1358.15	1350
ref [4]	1293.15	-	1313.15	-	1303.2
ref [86]	1262	1236	1273	1330	1296
this work	-	-	-	-	1275

available experimental values. The remarkable agreement of this work with experimental martensitic transformation temperatures confirms the validity of the scheme introduced in this thesis. To our best knowledge, it is the first time to present thermodynamic functions for $B2$ PtTi via computational methods, where standard harmonic models are inadequate for thermodynamic calculations. We are not aware of any experimental study that reveals thermodynamic functions of $B2$ PtTi system.

4.4 Computational Details

1) All electronic structure calculations are performed using VASP, implementing projector augmented wave (PAW) method. For both $B2$ and $B19$ PtTi, the PBE functional is used, with a plane wave kinetic energy cutoff of $230.3eV$. A $(4 \times 4 \times 4)$ Monkhorst-Pack mesh is used for creating the k-space grid. Volume relaxation for each supercell is performed in two steps (relaxing the initial structure and re-relaxing) using Methfessel-Paxton method with $ISMEAR = 1$ and $SIGMA = 0.2$. To obtain the energy (i.e. the energy of the relaxed volume structure), tetrahedron method with Blöchl corrections is used. All the energies, forces and second derivatives of energy (force constant matrix) used in calculations of free energies are obtained using

PAW-PBE. In order to obtain electronic contribution to free energy, Fermi smearing ($ISMEAR = -1$) is used with $SIGMA$ value set to the corresponding temperature, $SIGMA = k_B \times T$.

2) In the *steepest-descent* search in equation (3.16), γ_n is set to $0.02\mathring{A}^2/eV$. The second derivative of the reference potential is set to $20eV/\mathring{A}/\mathring{A}$ along all degree of freedoms.

3) The training data set for the cluster expansion consists of 116 constrained vibrational free energies, $F^*(\sigma, T)$, calculated by the presented scheme. Constrained vibrational free energy of σ_g is always included within the data set along with the constrained vibrational free energies of some configurations with a definite number of Pt and Ti atoms randomly displaced from $\mathbf{x}_g$.

4) Free energy of $B19$ and $B19'$ PtTi are calculated using standard quasi-harmonic approximation, utilizing fitfc code. For force constant matrix calculation, the fitfc code includes up to third nearest neighbor forces in a 128 atom supercell with 0.1 Ådisplacements.

Chapter Five

Conclusion

In this thesis, we present a new method in order to calculate the free energy of phases which reveal low-temperature mechanical instabilities but are dynamically stabilized at high enough temperatures. Numerous materials of technological importance feature high-symmetry high-temperature phases that exhibit phonon instabilities. Anharmonic vibrational contributions to the free energy play a crucial role in stabilization of such phases, yet the standard lattice dynamics approaches are deficient to account for these effects. Mechanical instabilities hinder defining the partition function in its usual form, i.e. integration of the Boltzmann distribution over the potential energy surface in the proximity of the high-symmetry structure. The energy surface becomes non-convex along unstable modes and introduces non-physical divergence in the calculation of the partition function.

The high-symmetry structure becomes thermodynamically favorable at high enough temperatures because it constantly undergoes local distortions towards many possible similar low-symmetry structures, while maintaining time-averaged high-symmetry structure, which introduces large stabilizing entropic contributions to the free energy.

We develop the method based on partitioning the phase space into multiple regions in order to accomplish a local exploration of multiple minima around the high-symmetry structure on the potential energy surface. The partitioning scheme facilitates the use of harmonic approximation to handle anharmonic lattice dynamics. Therefore, this method exploits the computational practicality of harmonic lattice dynamics while fully accounting for anharmonic effects.

The developed method is utilized in three different examples: the high-temperature bcc phase of group-IV transition metals, Ti and Zr, and the high-temperature $B2$ phase of PtTi, a shape memory alloy. The reasonable agreement between the free energy obtained for the prototypal example of bcc group-IV metals and the existing experimental and computational values confirms the validity of our method. More-

over, we calculate the martensitic transformation temperature in PtTi to be in good consistency with available experimental data. This can be considered as the first computational thermodynamic study on austenite PtTi, other than the traditional extrapolations methods.

The proposed method also offers a natural avenue to handle alloys since the cluster expansion method can easily allow for multiple species on each site of the augmented lattice introduced herein. Proposing an automated method in order to construct the augmented lattice would promote the broader use of the proposed general scheme. An augmented lattice could be constructed by imposing extra sites around the high-symmetry site, preferably along high-symmetry directions, in order to contain fluctuations to low-symmetry distortions of the high-symmetry structure. The scheme ensures to capture the local minima via an accurate exploration of the energy surface for the minimum associated with each configuration. This approach is specifically useful in more complicated system, where several candidate instabilities are possible. The most excessive computer cost in the proposed method arises from first-principles force constant calculations. In order to circumvent this computational obstacle, it is of important interest to utilize available approximations for force constant computations [76], and it is our future focus on this matter.

Bibliography

[1] J. Agren. Numerical treatment of diffusional reactions in multicomponent alloys. *Journal of Physics and Chemistry of Solids*, 43(4):385 – 391, 1982.

[2] J.O. Andersson and J. Agren. Models for numerical treatment of multicomponent diffusion in simple phases. *Journal of Applied Physics*, 72(4):1350–1355, 1992.

[3] J. Bhattacharya and A. van der Ven. Mechanical instabilities and structural phase transitions: The cubic to tetragonal transformation. *Acta Materialia*, 56:4226–4232, 2008.

[4] T. Biggs, M. B. Cortie, M. J. Witcomb, and L. A. Cornish. Martensitic transformations, microstructure, and mechanical workability of TiPt. *Metallurgical and Materials Transactions A*, 32(8):1881–1886, 2001.

[5] T Biggs, M.J Witcomb, and L.A Cornish. Martensite-type transformations in platinum alloys. *Materials Science and Engineering: A*, 273275:204 – 207, 1999.

[6] P.E. Blochl, O. Jepsen, and O.K. Andersen. Improved tetrahedron method for brillouin-zone integrations. *Phys. Rev. B*, 49:16223, 1994.

[7] P. Bresch. Anharmonicity. In *Phonons: Theory and Experiments I*, volume 34 of *Springer Series in Solid-State Sciences*, pages 152–200. Springer Berlin Heidelberg, 1982.

[8] W.G. Burgers. On the process of transition of the cubic-body-centered modification into the hexagonal-close-packed modification of zirconium. *Physica*, 1(712):561 – 586, 1934.

[9] Jr. Chase, M.W. Nist-janaf themochemical tables, fourth edition. *J. Phys. Chem. Ref. Data, Monograph 9*, 19988.

[10] W. Cochran. Crystal stability and the theory of ferroelectricity. *Phys. Rev. Lett.*, 3:412–414, Nov 1959.

[11] J.D. Cox, D.D. Wagman, and V.A. Medvedev. Codata key values for thermodynamics. *Hemisphere Publishing Corp.*, New York, 1984.

[12] P. J. Craievich, J. M. Sanchez, R. E. Watson, and M. Weinert. Structural instabilities of excited phases. *Phys. Rev. B*, 55:787–797, 1997.

[13] P. J. Craievich, M. Weinert, J. M. Sanchez, and R. E. Watson. Local stability of nonequilibrium phases. *Phys. Rev. Lett.*, 72:3076–3079, 1994.

[14] D. de Fontaine and O. Buck. A monte-carlo simulation of the omega phase transformation. *Philosophical Magazine*, 27(4):967 – 983, 1973.

[15] H.C. Donkersloot and J.H.N. Van Vucht. Martensitic transformations in gold-titanium, palladium-titanium and platinum-titanium alloys near the equiatomic composition. *Journal of the Less Common Metals*, 20(2):83 – 91, 1970.

[16] K. Einarsdotter, B. Sadigh, G. Grimvall, and V. Ozolins. Phonon instabilities in fcc and bcc Tungsten. *Phys. Rev. Lett*, 79:2073–2076, 1997.

[17] K. Enami and S. Nenno. Memory effect in Ni-36.8 At. Pct Al martensite. *Metallurgical Transactions*, 2(5):1487–1490, 1971.

[18] Daniel L. Farber, Michael Krisch, Daniele Antonangeli, Alexandre Beraud, James Badro, Florent Occelli, and Daniel Orlikowski. Lattice dynamics of molybdenum at high pressure. *Phys. Rev. Lett.*, 96:115502, Mar 2006.

[19] R.W. Fonda, H.N. Jones, and R.A. Vandermeer. The shape memory effect in equiatomic TaRu and NbRu alloys. *Scripta Materialia*, 39(8):1031–1037, 1998.

[20] G. Grimvall, B. Magyari-Kope, V. Ozoliņš, and K. A. Persson. Lattice instabilities in metallic elements. *Rev. Mod. Phys.*, 84:945, 2012.

[21] A. Heiming, W. Petry, J. Trampenau, M. Alba, C. Herzig, H. R. Schober, and G. Vogl. Phonon dispersion of the bcc phase of group-IV metals. II. bcc zirconium, a model case of dynamical precursors of martensitic transitions. *Phys. Rev. B*, 43:10948–10962, May 1991.

[22] A. Heiming, W. Petry, J. Trampenau, M. Alba, C. Herzig, and G. Vogl. Phonons and martensitic phase transitions in pure bcc Ti and bcc Zr. *Phys. Rev. B*, 40:11425–11428, Dec 1989.

[23] O. Hellman, I. A. Abrikosov, and S. I. Simak. Lattice dynamics of anharmonic solids from first principles. *Phys. Rev. B*, 84:180301, 2011.

[24] R. G. Hennig, T. J. Lenosky, D. R. Trinkle, S. P. Rudin, and J. W. Wilkins. Classical potential describes martensitic phase transformations between the α, β, and ω titanium phases. *Phys. Rev. B*, 78:054121, 2008.

[25] K.-M. Ho, C. L. Fu, and B. N. Harmon. Vibrational frequencies via total-energy calculations. applications to transition metals. *Phys. Rev. B*, 29:1575–1587, Feb 1984.

[26] K.-M. Ho, C.-L. Fu, and B.N. Harmon. Microscopic analysis of interatomic forces in transition metals with lattice distortions. *Phys. Rev. B.*, 28:6687–6694, 1983.

[27] Q. Hong, S. V. Ushakov, A. Navrotsky, and A. van de Walle. Combined computational and experimental investigation of the refractory properties of La2Zr2O7. *Acta Materialia*, 84:275 – 282, 2015.

[28] W. G. Hoover. Canonical dynamics: Equilibrium phase-space distributions. *Phys. Rev. A*, 31:1695, 1985.

[29] X. Huang, G. J. Ackland, and K. M. Rabe. Crystal structures and shape-memory behaviour of NiTi. *Nat Mater*, 2:307–311, 2003.

[30] X. Huang, K. M. Rabe, and G. J. Ackland. First-principles study of the structural energetics of PdTi and PtTi. *Phys. Rev. B*, 67:024101, Jan 2003.

[31] L. Kaufman. The lattice stability of metals I. Titanium and Zirconium. *Acta Metallurgica*, 7(8):575 – 587, 1959.

[32] L. Kaufman. Computational thermodynamics and materials design. *Calphad*, 25(2):141 – 161, 2001.

[33] L. Kaufman. Hume-rothery and calphad thermodynamics. In *CALPHAD and Alloy Thermodynamics as held at the 2002 TMS Annual Meeting*, pages 3–19, 2002.

[34] L. Kaufman and H. Bernstein. *Computer Calculation of Phase Diagram*. Academic Press Inc., New York, USA, 1970.

[35] W. Kohn and L. J. Sham. Self-consistent equations including exchange and correlation effects. *Phys. Rev.*, 140:A1133–A1138, Nov 1965.

[36] G. Kresse and J. Furthmller. Efficiency of ab-initio total energy calculations for metals and semiconductors using a plane-wave basis set. *Comput. Mat. Sci.*, pages 6–15, 1996.

[37] G. Kresse and J. Furthmller. Efficient iterative schemes for ab initio total-energy calculations using a plane-wave basis set. *Phys. Rev. B*, 54:11169, 1996.

[38] G. Kresse and J. Hafner. Ab initio molecular dynamics for liquid metals. *Phys. Rev. B*, 47:558, 1993.

[39] G. Kresse and J. Hafner. Ab initio molecular-dynamics simulation of the liquid-metal-amorphous-semiconductor transition in germanium. *Phys. Rev. B*, 49:14251, 1994.

[40] G. Kresse and D Joubert. From ultrasoft pseudopotentials to the projector augmented-wave method. *Phys. Rev. B*, 59:1758–1775, 1999.

[41] Y Kudoh, M Tokonami, S Miyazaki, and K Otsuka. Crystal structure of the martensite in Ti-49.2 at.%Ni alloy analyzed by the single crystal x-ray diffraction method. *Acta Metallurgica*, 33(11):2049 – 2056, 1985.

[42] C. Lexcellent. *Shape-memory Alloys Handbook*. John Wiley & Sons, Inc., 2013.

[43] M. Li, W. Han, and C. Li. Thermodynamic assessment of the PtTi system. *Journal of Alloys and Compounds*, 461(12):189 – 194, 2008.

[44] G. J. Martyna, M. L. Klein, , and M. Tuckerman. Nose-hoover chains: The canonical ensemble via continuous dynamics. *J. Chem. Phys.*, 97:2635, 1992.

[45] Z. Mei, S. Shang, Y. Wang, and Z. Liu. Density-functional study of the thermodynamic properties and the pressur-temperature phase diagram of Ti. *Phys. Rev. B*, 80:104116, 2009.

[46] M. Methfessel and A.T. Paxton. High-precision sampling for brillouin-zone integration in metals. *Phys. Rev. B*, 40:3616, 1989.

[47] A. P. Mirgorodsky, M. B. Smirnov, and P. E. Quintard. Lattice-dynamical study of the cubic-tetragonal-monoclinic transformations of zirconia. *Phys. Rev. B*, 55:19–22, 1997.

[48] Hendrik J. Monkhorst and James D. Pack. Special points for brillouin-zone integrations. *Phys. Rev. B.*, 13:5188–5192, 1976.

[49] S. Nose. A molecular-dynamics method for simulations in the canonical ensemble. *Mol. Phys.*, 52:255–268, 1984.

[50] S. Nose. A unified formulation of the constant temperature molecular dynamics methods. *J. Chem. Phys.*, 81:511, 1984.

[51] K. Otsuka and X. Ren. Recent developments in the research of shape memory alloys. *Intermetallics*, 7(5):511 – 528, 1999.

[52] V. Ozolins. First-principles calculations of free energies of unstable phases: The case of fcc W. *Phys. Rev. Lett*, 102:065702, 2009.

[53] K. Parlinski, Z-.Q. Li, and Y. Kawazoe. First-principles determination of the soft mode in cubic ZrO2. *Phys. Rev. Lett.*, 78:4063, 1997.

[54] J. P. Perdew, K. Burke, and M. Ernzerhof. Generalized gradient approximation made simple. *Phys. Rev. Lett.*, 77:3865–3868, 1996.

[55] K. Persson, M. Ekman, and V. Ozolins. Phonon instabilities in bcc Sc, Ti, La, and Hf. *Phys. Rev. B*, 61:11221–11224, 2000.

[56] W. Petry, A. Heiming, J. Trampenau, M. Alba, C. Herzig, H.R. Schober, and G. Vogl. Phonon dispersion of the bcc phase of group-IV metals. I. bcc titanium. *Phys. Rev. B*, 43:10934–10947, 1991.

[57] W. Petry, A. Heiming, J. Trampenau, and G. Vogl. On the diffusion mechanism in the bcc phase of the group 4 metals. *Defect and Diffusion Forum*, 66-69:157 – 174, 1991.

[58] U Pinsook. Molecular dynamics study of vibrational entropy in bcc and hcp zirconium. *Phys. Rev. B*, 66:024109, Jul 2002.

[59] G.-M. Rotaru, W. Tirry, P. Sittner, J. Van Humbeeck, and D. Schryvers. Microstructural study of equiatomic PtTi martensite and the discovery of a new long-period structure. *Acta Materialia*, 55(13):4447 – 4454, 2007.

[60] R.Quijano, R. de Coss, and D. J. Singh. Electronic structure and energetics of the tetragonal distortion for TiH_2, ZrH_2, and HfH_2:a first-principles study. *Phys. Rev. B*, 80:184103, 2009.

[61] J.M. Sanchez, F. Ducastelle, and D. Gratias. Generalized cluster description of multicomponent systems. *Physica*, 128:334–350, 1984.

[62] L.M. Schetky. In J. H. Westbrook and R. L. Fleischer, editors, *Intermetallic Compounds. Principles and Practice*, volume 2, pages 529–58. John Wiley & Sons, 1995.

[63] W. M. Shaw and L. D. Muhlestein. Investigation of the phonon dispersion relations of chromium by inelastic neutron scattering. *Phys. Rev. B*, 4:969–973, Aug 1971.

[64] S.K. Sikka, Y.K. Vohra, and R. Chidambaram. Omega phase in materials. *Progress in Materials Science*, 27(3):245 – 310, 1982.

[65] P. Souvatzis, O. Eriksson, M. I. Katsnelson, and S. P. Rudin. Entropy driven stabilization of energetically unstable crystal structure explained from first principles theory. *Phys. Rev. Lett*, 100:095901, 2008.

[66] P. Souvatzis, O. Eriksson, M.I. Katsnelson, and S.P. Rudin. The self-consistent ab initio lattice dynamical method. *Computational Materials Science*, 44:888–894, 2009.

[67] P.J. Spencer. A brief history of CALPHAD. *Calphad*, 32(1):1 – 8, 2008.

[68] J. C. Thomas and A. van der Ven. Elastic properties and stress-temperature phase diagrams of high-temperature phases with low-temperature lattice instabilities. *Phys. Rev. B*, 90:224105, 2014.

[69] A Togo and I Tanaka. First principles phonon calculations in materials science. *Scr. Mater.*, 108:1–5, Nov 2015.

[70] J. Trampenau, W. Petry, and C. Herzig. Temperature dependence of the lattice dynamics of chromium. *Phys. Rev. B*, 47:3132–3137, 1993.

[71] U.V.Waghmare and K .M .Rabe. ab initio statistical mechanics of the ferroelectric phase transition in PbTiO_3. *Phys. Rev. B*, 55:6161, 1997.

[72] A. van de Walle. Multicomponent multisublattice alloys, nonconfigurational entropy and other additions to the alloy theoretic automated toolkit. *Calphad*, 33:266–278, 2009.

[73] A. van de Walle and M. Asta. Self-driven lattice-model monte carlo simulations of alloy thermodynamic properties and phase diagrams. *Modelling Simul. Mater. Sci. Eng.*, 2002.

[74] A. van de Walle, M. Asta, and G. Ceder. The alloy theoretic automated toolkit: a user guide. *Calphad*, 26:539–553, 2002.

[75] A. van de Walle and G. Ceder. Automating first-principles phase diagram calculations. *J. Phase Equilib*, 23:348–359, 2002.

[76] A. van de Walle and G. Ceder. The effect of lattice vibrations on substitutional alloy thermodynamics. *Rev. Mod. Phys.*, 74:11–45, 2002.

[77] A. van de Walle, Q. Hong, S. Kadkhodaei, and R. Sun. The free energy of mechanically unstable phases. *Nature Communications*, 6:7559, 2015.

[78] G. Voronoi. Nouvelles applications des paramtres continus la thorie des formes quadratiques deuxime memoire: Recherches sur les parallllodres primitifs. *Journal fr die Reine und Angewandte Mathematik*, 134:198–287, 1908.

[79] F. E. Wang, W. J. Buehler, and S. J. Pickart. Crystal structure and a unique "martensitic" transition of TiNi. *Journal of Applied Physics*, 36(10), 1965.

[80] X. Wang. Twinned structure for shape memory: First-principles calculations. *Phys. Rev. B*, 78:092103, Sep 2008.

[81] N. R. Werthamer. Self-consistent phonon formulation of anharmonic lattice dynamics. *Phys. Rev. B*, 1:572, 1970.

[82] E. Wigner and F. Seitz. On the constitution of metallic sodium. *Phys. Rev.*, 43:804, 1933.

[83] F. Willaime and C. Massobrio. Temperature-induced hcp-bcc phase transformation in zirconium: A lattice and molecular-dynamics study based on an N -body potential. *Phys. Rev. Lett.*, 63:2244–2247, Nov 1989.

[84] P. Wolfe. Convergence conditions for ascent methods. *SIAM Review*, 11:226–235, 1969.

[85] Q. Xu and A. van der Ven. First-principles investigation of metal-hydride phase stability: The Ti-H system. *Phys. Rev. B*, 76:064207, 2007.

[86] Y. Yamabe-Mitarai, T. Hara, S. Miura, and H. Hosoda. Mechanical properties of Ti-50(Pt,Ir) high-temperature shape memory alloys. *MATERIALS TRANSACTIONS*, 47(3):650–657, 2006.

[87] Y. Yamabe-Mitarai, T. Hara, S. Miura, and H. Hosoda. Shape memory effect and pseudoelasticity of TiPt. *Intermetallics*, 18(12):2275 – 2280, 2010.

[88] Y. Y. Ye, C. T. Chan, and K. M. Ho. Structural and electronic properties of the martensitic alloys TiNi, TiPd, and TiPt. *Phys. Rev. B*, 56:3678–3689, Aug 1997.

[89] Y.-Y. Ye, Y. Chen, K.-M. Ho, B. N. Harmon, and P. A. Lindgard. Phonon-phonon coupling and the stability of the high-temperature bcc phase of Zr. *Phys. Rev. Lett.*, 58:1769–1772, 1987.

[90] J. Zarestky, C. Stassis, B. N. Harmon, K. M. Ho, and C. L. Fu. Temperature dependence of the vibrational modes of molybdenum. *Phys. Rev. B*, 28:697–701, Jul 1983.

[91] N. A. Zarkevich and D. D. Johnson. Stable atomic structure of NiTi austenite. *Phys. Rev. B*, 90:060102, Aug 2014.

[92] A. T. Zayak, P. Entel, J. Enkovaara, A. Ayuela, and R. M. Nieminen. First-principles investigation of phonon softenings and lattice instabilities in the shape-memory system Ni_2MnGa. *Phys. Rev. B*, 68:132402, 2003.

[93] C. Zener. *Influence of Entropy on Phase Stabilization.* Phase Stability in Metals and Alloys (McGraw-Hill, New York), 1967.

[94] W. Zhong, David Vanderbilt, and K. M. Rabe. First-principles theory of ferroelectric phase transitions for perovskites: The case of BaTiO_3. *Phys. Rev. B*, 52:6301–6312, 1995.

[95] W. Zhong, David Vanderbilt, and K.M. Rabe. Phase transitions in BaTiO_3 from first principles. *Phys. Rev. Lett*, 73:1861–1864, 1994.